

**THEORY AND SIMULATION OF RARE EVENTS  
IN STOCHASTIC SYSTEMS**

by

**Bin W. Zhang**

MS, University of Science and Technology of China, 2001

Submitted to the Graduate Faculty of  
the Department of Physics & Astronomy in partial fulfillment  
of the requirements for the degree of

**Doctor of Philosophy**

University of Pittsburgh

2008

UNIVERSITY OF PITTSBURGH  
DEPARTMENT OF PHYSICS & ASTRONOMY

This dissertation was presented

by

Bin W. Zhang

It was defended on

August 7th 2009

and approved by

David Jasnow, Department of Physics & Astronomy

Daniel M Zuckerman, Department of Computational Biology

Daniel Boyanovsky, Department of Physics & Astronomy

Robert Coalson, Department of Physics & Astronomy, Department of Chemistry

Anthony H. Duncan, Department of Physics & Astronomy

Walter I. Goldburg, Department of Physics & Astronomy

Dissertation Advisors: David Jasnow, Department of Physics & Astronomy,

Daniel M Zuckerman, Department of Computational Biology

# THEORY AND SIMULATION OF RARE EVENTS IN STOCHASTIC SYSTEMS

Bin W. Zhang, PhD

University of Pittsburgh, 2008

Activated processes driven by rare fluctuations are discussed in this thesis. Understanding the dynamics of these activated processes is important for understanding chemical and biological reactions, drug design and many other important applications. First, theoretical tools including the Langevin equation, the Fokker-Planck equation and the path integral technique are reviewed. Based on these theories, simulation methods have been developed to sample the activated processes by a number of investigators. Several of the most important path sampling and path generating approaches are introduced. A combination of analytic and numerical techniques are applied to study the distribution of the durations of transition events over a barrier in a one-dimensional system undergoing over-damped Langevin dynamics. Then we employ the “weighted ensemble” path sampling method to generate an unbiased ensemble of paths for a conformational transition in a 210-dimensional model of the protein calmodulin, and also find the reaction rate. The results show that the weighted ensemble approach is a remarkably straightforward and successful method. At last, systems with multiple channels are studied by the weighted ensemble approach and the more common transition path sampling approach. The weighted ensemble method is distinguished by its ability to perform complete path sampling for systems with multiple channels at reasonable cost.

## TABLE OF CONTENTS

<b>I.</b>	<b>INTRODUCTION</b>	1
	A. Rare events	1
	B. Examples	1
	1. Brownian particle in double well potential	1
	2. Calmodulin	3
	C. Basic physical ideas	6
	D. Outline of thesis	8
<b>II.</b>	<b>THEORY OF BROWNIAN MOTION</b>	9
	A. Introduction	9
	1. Historical background of Brownian motion	9
	2. Application of Brownian motion	12
	B. Langevin equation	13
	1. Diffusion coefficient	13
	2. Over-Damped Langevin equation	15
	C. Fokker-Planck equation	16
	1. Derivation of Fokker-Planck equation	16
	2. Discussion of Fokker-Planck equation	20
	D. Path integral representation	25
	1. A simple illustration	25
	2. Path integral formulation for free Brownian motion	26
	3. Path integral formulation for Brownian motion in an absorbing medium	29
	4. Path integral formulation of Brownian motion in a field of force	30

5. Optimal path . . . . .	31
6. The quadratic approximation . . . . .	32
E. Examples . . . . .	36
1. Reaction rate . . . . .	36
2. Splitting probability . . . . .	39
<b>III. SIMULATION METHODS . . . . .</b>	<b>42</b>
A. Importance of simulation . . . . .	42
B. Brute force simulation . . . . .	43
C. Path sampling approaches . . . . .	44
1. Transition path sampling . . . . .	45
2. Weighted ensemble method . . . . .	49
3. Dynamic importance sampling . . . . .	54
4. Langevin dynamics in path space . . . . .	59
5. Transition interface sampling . . . . .	60
6. Others . . . . .	63
D. Path finding techniques . . . . .	63
1. Targeted molecular dynamics . . . . .	63
2. Steered molecular dynamics simulation . . . . .	66
<b>IV. DURATION OF TRANSITION-EVENTS . . . . .</b>	<b>68</b>
A. Introduction . . . . .	68
B. Simulation . . . . .	71
C. Transition-Events . . . . .	74
1. Distribution of transition-event duration . . . . .	74
2. Examples: free diffusion and linear potential . . . . .	75
3. Approximate solution for inverted parabolic potential . . . . .	78
4. Moments of the distribution of transition-event durations . . . . .	80
5. Short time behavior . . . . .	88
6. Long time behavior for double-well potential . . . . .	94
7. Implications for long-time behavior in complex systems . . . . .	98
D. Concluding discussion . . . . .	99

<b>V.</b>	<b>WE SIMULATION FOR CAM</b>	101
	A. Introduction	101
	B. Methods	103
	1. Path sampling using the weighted ensemble (WE) approach.	103
	2. Bistable Gō model of united-residue calmodulin (N-terminal domain).	105
	3. Error analysis by block averaging.	107
	C. Results	108
	1. Distribution of event durations	108
	2. The transition rate	110
	3. Structural cross-sections of the path ensemble	110
	4. Efficiency	110
	5. Use of a two-dimensional progress coordinate	112
	D. Discussion: Applying WE to More Complex Systems	113
	E. Conclusions	114
<b>VI.</b>	<b>TEST SYSTEMS WITH MULTIPLE CHANNELS</b>	116
	A. Introduction	116
	B. Comparison of two path sampling methods	117
	1. Potentials	117
	2. Simulation results	118
	C. Alanine dipeptide	121
	1. Alanine dipeptide	121
	2. Simulation results and discussion	122
	D. Conclusions	128
<b>VII.</b>	<b>CONCLUSION AND OUTLOOK</b>	129
	A. What has been accomplished	129
	B. What will be accomplished	130
	1. Distribution of the durations of transition-events	130
	2. Weighted ensemble approach	130
	<b>BIBLIOGRAPHY</b>	132

## LIST OF TABLES

1	The extreme points of the model potentials . . . . .	118
2	The distributions of four types of transition paths between states $C_{7eq}$ and $C_{7ax}$ of alanine dipeptide . . . . .	126

## LIST OF FIGURES

1	A Brownian particle moving in a double well potential . . . . .	2
2	A Brownian particle moving in a two-dimensional toy potential . . . . .	3
3	Calmodulin . . . . .	4
4	A sample trajectory from the simulation of the N-terminal domain of calmodulin	5
5	Basic physical ideas . . . . .	7
6	A schematic illustration of Brownian motion . . . . .	9
7	A simple illustration for the basic idea of path integral . . . . .	25
8	A path goes through the sequence of coordinates $(x_0, x_1, x_2 \dots x_N, x)$ at corresponding times $(t_0, t_1, t_2 \dots t_N, t)$ within ranges $(0, dx_1, dx_2 \dots dx_N, 0)$ . . . . .	27
9	An over-damped Brownian particle escapes from a potential well . . . . .	36
10	Shooting algorithm to generate new path . . . . .	47
11	Probability distribution and histogram of simulations for a regular brute-force simulation . . . . .	49
12	Schematic probability and histogram of simulations for a weighted ensemble simulation . . . . .	50
13	Schematic illustration of the Weighted Ensemble (WE) method . . . . .	52
14	The waiting time of the rare events satisfies the exponential distribution . . . . .	53
15	Generate new path with a bias force in dynamic importance sampling method	56
16	Schematic diagram of sampling for $p(x_0)$ with given $x_0$ in transition interface sampling . . . . .	61
17	Schematic representation of two-dimensional targeted molecular dynamics . . . . .	64
18	Schematic diagram of steered molecular dynamics simulation . . . . .	66

19	Trajectory for a Brownian particle moving in a double well potential . . . . .	68
20	The definition of the transition-event duration, $t_b$ . . . . .	69
21	Scaled event duration distribution for free diffusion and the linear potential . . . . .	77
22	Inverted parabolic potential with different boundary conditions . . . . .	78
23	The event-duration distribution $\rho_b$ for inverted parabolic potentials with different barrier heights . . . . .	80
24	Reconstruction of $\rho_b$ for double-well potentials based on moments and a Gram-Schmidt procedure . . . . .	87
25	Calculating the path integral with absorbing walls at $x = 0$ and $x = L$ . . . . .	89
26	Short time behavior of $\rho_b$ for double-well potentials . . . . .	92
27	A high-barrier double-well potential $U^*$ and its Schrödinger analogue $V_s$ . . . . .	95
28	Comparison of two numerical approaches for computing the long time behavior of the event-duration distribution . . . . .	97
29	Long time behavior of $\rho_b$ for double-well potentials and the inverted parabola . . . . .	98
30	The N-terminal domain of calmodulin undergoes a large-scale structural change when it binds calcium . . . . .	102
31	The time evolution of the probability distribution in the WE simulation of calmodulin . . . . .	104
32	The potential of bonded interaction in the double-native Gō potential . . . . .	106
33	The non-native, single-native and double-native potentials in the double-native Gō potential . . . . .	107
34	The distribution of transition-event durations $\rho_b(t)$ from WE and brute-force simulations for calmodulin . . . . .	109
35	Structural distributions describing the heterogeneity of the path ensemble connecting the Apo and Holo states of calmodulin, based on both WE and brute-force simulations . . . . .	111
36	Contours of toy potentials with barrier-separated channels of paths . . . . .	117
37	Cross sections at $x = 0$ of the model potentials . . . . .	118
38	The transition path sampling (TPS) method switches between two types of paths . . . . .	119

39	The weighted ensemble method switches between two types of paths . . . . .	120
40	Distribution of transition-event durations for the model potentials . . . . .	120
41	Alanine dipeptide molecule . . . . .	122
42	Four energy minima of alanine dipeptide . . . . .	123
43	One path of alanine dipeptide is plotted in the regular dihedral plane and an enlarged dihedral plane . . . . .	124
44	Four types of transition paths between states $C_{7eq}$ and $C_{7ax}$ of alanine dipeptide	125
45	Two channels of transition-events between states $C_{7eq}$ and lower right $C_{7ax}$ of alanine dipeptide . . . . .	126

## I. INTRODUCTION

### A. RARE EVENTS

Driven by a rare fluctuation, a system can climb over an energy barrier, and finish the transition from one state to the other. It is an activated process. It is also called a “rare event” because it involves a waiting time before these events happen. Lots of important dynamical phenomena are activated processes. Examples include chemical reactions, protein conformational changes and nucleation, etc [1]. Understanding the dynamics of these activated processes is important for chemical and biological reaction control, drug design and many other important applications. [1]. The theory of rare events has been studied for a long time by physicists and chemists [2]. Besides theoretical formulation, computer sampling becomes also important for this topic because of the difficulty of obtaining analytical solutions and the increase of computational power.

### B. EXAMPLES

We will use two examples to explain the concept of rare events more explicitly.

#### 1. Brownian particle in double well potential

The first example is a Brownian particle moving in a double well potential, an important model that will be used many times in this thesis.

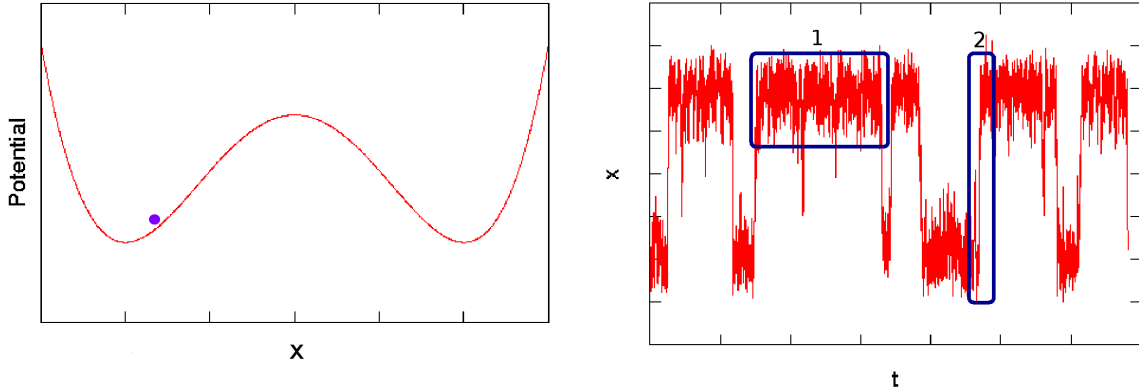


Figure 1: The left panel shows a Brownian particle moving in a double well potential. The right panel shows its trajectory and the time is in units of computational steps. In the right panel, the first rectangle indicates the waiting period before the rare event and the second rectangle indicates one transition-event.

The right picture in Fig. 1 shows the trajectory  $x(t)$  of this Brownian particle<sup>1</sup>. One can find two stable states and several transition-events from its trajectory. One transition-event is indicated by the second rectangle. All these transitions are the rare events which we are interested in. Because these transitions are driven by thermal fluctuations, some degree of variability among events must be expected. Therefore, the study will maintain a statistical viewpoint and the transition-events will be treated as an ensemble. The first rectangle shows one waiting period before the rare events; and an appropriate average tells how frequently these rare events will happen. Its evaluation is a very important topic [2]. The timescale of waiting is much longer than the timescale of rare events, which is obvious in Fig. 1. When

<sup>1</sup> The trajectory was obtained by the simulation based on the over-damped Langevin equation

$$\frac{dx}{dt} = \frac{F}{\gamma} + R(t), \quad (\text{I.1})$$

where  $\gamma$  is the friction constant,  $F$  is the physical force and  $R$  is the Gaussian white noise with zero mean and correlation

$$\langle R(t)R(t') \rangle = \left( \frac{2k_B T}{\gamma} \right) \delta(t - t') = 2D\delta(t - t'). \quad (\text{I.2})$$

The Langevin equation will be discussed later in Sec.(II.B). Eq.(I.2) shows that the fluctuations will increase as the temperature  $T$  increases. So in higher temperature the Brownian particle will become more active and the transition-events will happen more frequently.

the energy barrier is high ( $\gtrsim 10k_B T$ ), the timescale of waiting time will be beyond the ability of our computational power. So how to avoid waiting time and focus computer time on rare events is an appreciated challenge in computer simulation.

In higher dimensional space, sometimes transition paths go through different channels. One example in two-dimensional space is shown in Fig. 2. Finding multiple channels of paths will be discussed later in this thesis.

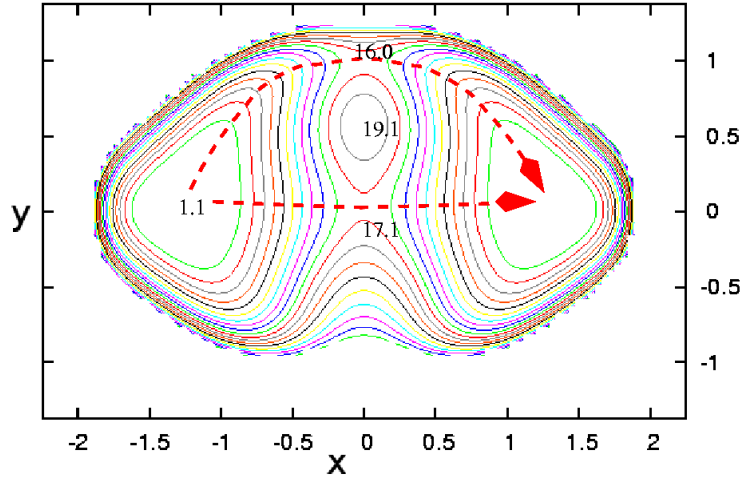


Figure 2: A Brownian particle moving in a two-dimensional toy potential. The red arrows show the multiple channels of paths connecting two stable states. The potential energy is in unit  $k_B T$ .

## 2. Calmodulin

The second example is the conformational change of a protein called calmodulin. Proteins are polymers of amino acids, they are most of the dry mass of a cell, and they also execute nearly all cell functions. For example, in a cell enzymes provide the intricate molecular surfaces, which promotes its chemical reactions. [3]. A protein's physical interaction with other molecules decides its biological properties. Every protein can stick or bind to other molecules [3]. When there is an interaction, the conformation of the protein will generally change. It has long been appreciated that conformational changes in proteins are critical

to biological function. Examples including allosteric proteins like hemoglobin, enzymes like adenylate kinase, signaling proteins like calmodulin, and motor proteins like myosin are only the most famous textbook cases [4].

Calcium (as  $\text{Ca}^{2+}$ ) plays an important role for numerous functions of eukaryotes. The extracellular concentration of  $\text{Ca}^{2+}$  ( $\sim 10^{-3}\text{mol/L}$ ) is about 10,000 times higher than intracellular one ( $\sim 10^{-7}\text{mol/L}$ ) because a cell continually pumps the calcium ion out of the cytosol (the internal fluid of the cell). The big difference of concentration makes the cell ready to import the calcium ion, which acts as a messenger, through its calcium channels [3, 5].

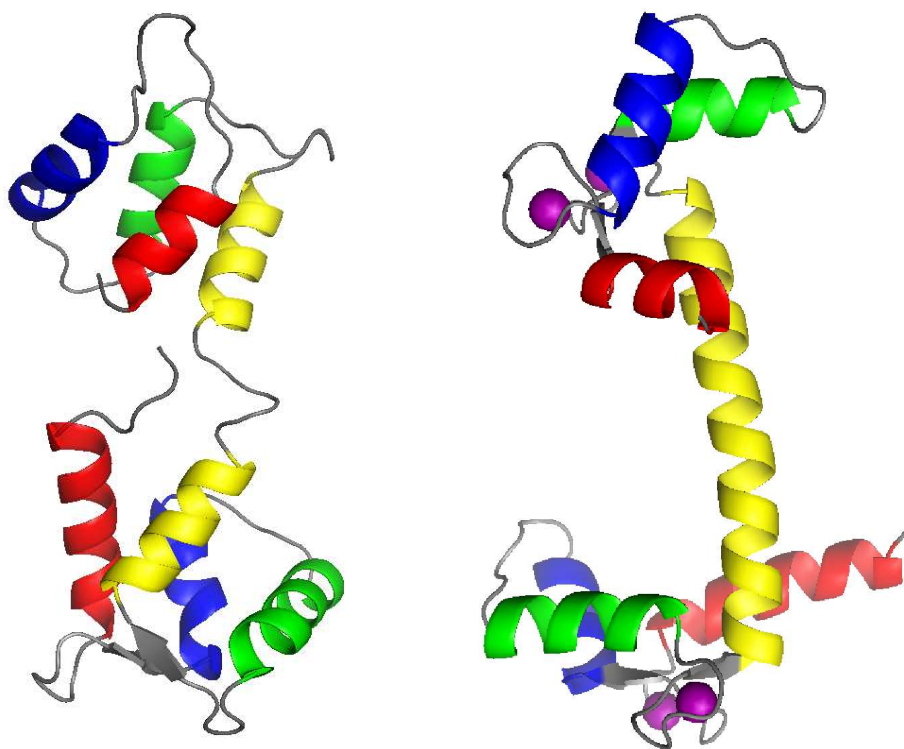


Figure 3: Calmodulin (CaM). The left is the Apo structure (1CFD), which is calcium-free. The right is the Holo structure (1CLL), which is calcium-bound. The purple spheres are bound calcium ions. CaM will undergo a large-scale structure change when it binds calcium

To detect the change of concentration of calcium ions, a cell must have a calcium sensor. Calmodulin is a protein that can bind calcium ions, which, as noted, are found in the cytosol

of all eukaryotic cells [3]. There are four binding sites in Calmodulin, each one can sense an intracellular change of concentration of  $\text{Ca}^{2+}$  as low as  $1\mu\text{M}$  [6]. The binding of  $\text{Ca}^{2+}$  causes a significant conformational change of Calmodulin, as shown in Fig. 3.

In Fig. 4, a sample trajectory from the simulation of the N-terminal domain of calmodulin is shown. The vertical axis is the distance-RMSD <sup>2</sup> (DRMSD), which quantifies molecular structural difference from one conformation to another. We will explain DRMSD later in Chapter V. In Fig. 4, the stable state with small DRMSD is the structures close to the Holo structure, and the other one with large DRMSD is close to the Apo structure. By comparing Fig. 4 and the right picture in Fig. 1, although the conformational change of CaM is a problem with hundreds or thousands of degrees of freedom, it exhibits familiar properties of rare events in one-dimensional space.

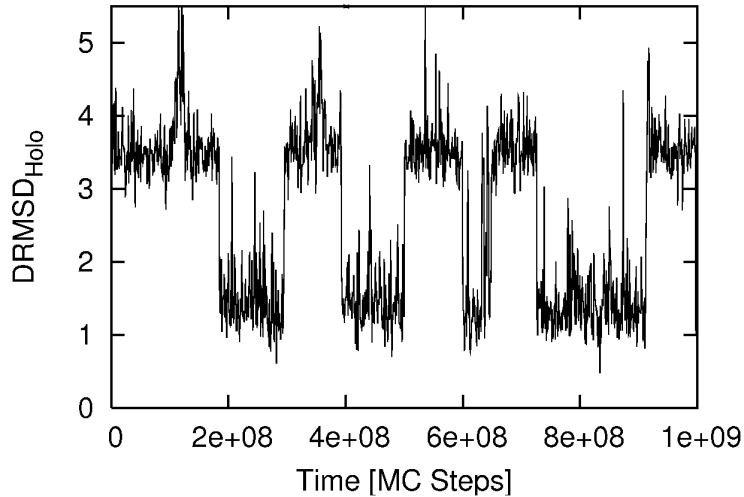


Figure 4: A sample trajectory from the simulation of the N-terminal domain of calmodulin by using a simple potential model. The trajectory exhibits several transition-events and two stable states.

---

<sup>2</sup>RMSD: root mean square deviation, the measure of the average distance between the structures of superimposed proteins.

### C. BASIC PHYSICAL IDEAS

For a single Brownian particle, its trajectory  $x(t)$  is the basic physical object of interest. Dividing the total force acting on the Brownian particle into the systematic part (or friction) and the fluctuation (or noise), the Langevin equation provides the equation of motion for the Brownian particle [7–11]. The Langevin equation is one basic tool to study the rare events in stochastic process. One can follow Langevin dynamics to run “brute-force” simulations easily. But brute-force simulation cannot avoid the long waiting times before the rare events happen, so usually it is not the best choice. We did brute-force simulation for several low barrier cases, i.e., a low-dimensional toy model, small molecules and simplified models of proteins at high temperature.

For stochastic processes, the information on one single random case is not enough; an ensemble average is the final goal. The Fokker-Planck equation describes the average behavior of a statistical ensemble of Brownian particles, and is another basic equation for stochastic process [7–11]. The Fokker-Planck equation gives the time evolution of probability density function  $P(x, t)$ , where  $P(x, t)dx$  is the probability that one finds the Brownian particle between  $x$  and  $x + dx$  at time  $t$ . The Fokker-Planck equation is a mathematically equivalent formulation to the Langevin equation under certain conditions. One can run multiple brute-force simulations, as a statistical ensemble, to get the approximate solution of  $P(x, t)$ . The “weighted ensemble” approach, an advanced sampling method, is based on this. The weighted ensemble approach is much more efficient than the brute force simulation, especially for high barrier problems. We will discuss this method carefully in this thesis later and apply it to a low-dimensional toy model, small molecules and simplified models of proteins.

As we just mentioned, if one can sample the possible trajectories of Brownian particles enough times, one finds  $P(x, t)$  eventually. This job is formally accomplished by a path integral technique. Calculating the weights of all possible trajectories of Brownian particles, path integral techniques can give the “propagator” which is equivalent to Green’s function solution of the associated Fokker-Planck equation [12, 13]. Path integral methods provide another useful tool and a different perspective for the study of Brownian motion. A trajectory in a path integral is analogous to a configuration in equilibrium statistical mechanics, and the

path integral is the analog of the partition function. Several advanced simulation approaches for studying rare events take root in the idea of path integral methods, i.e., “transition path sampling”, “dynamic importance sampling” and Langevin dynamics in path space. These methods all sample the paths of rare events by evaluating their relative weights and concentrate the computer time on the rare events. Although these methods study nonequilibrium systems, they treat the transition paths as an equilibrium ensemble and borrow sampling ideas from previous experience in the study of equilibrium system. Transition path sampling, maybe the most popular path sampling method, will be used for low-dimensional toy model and small molecules below.

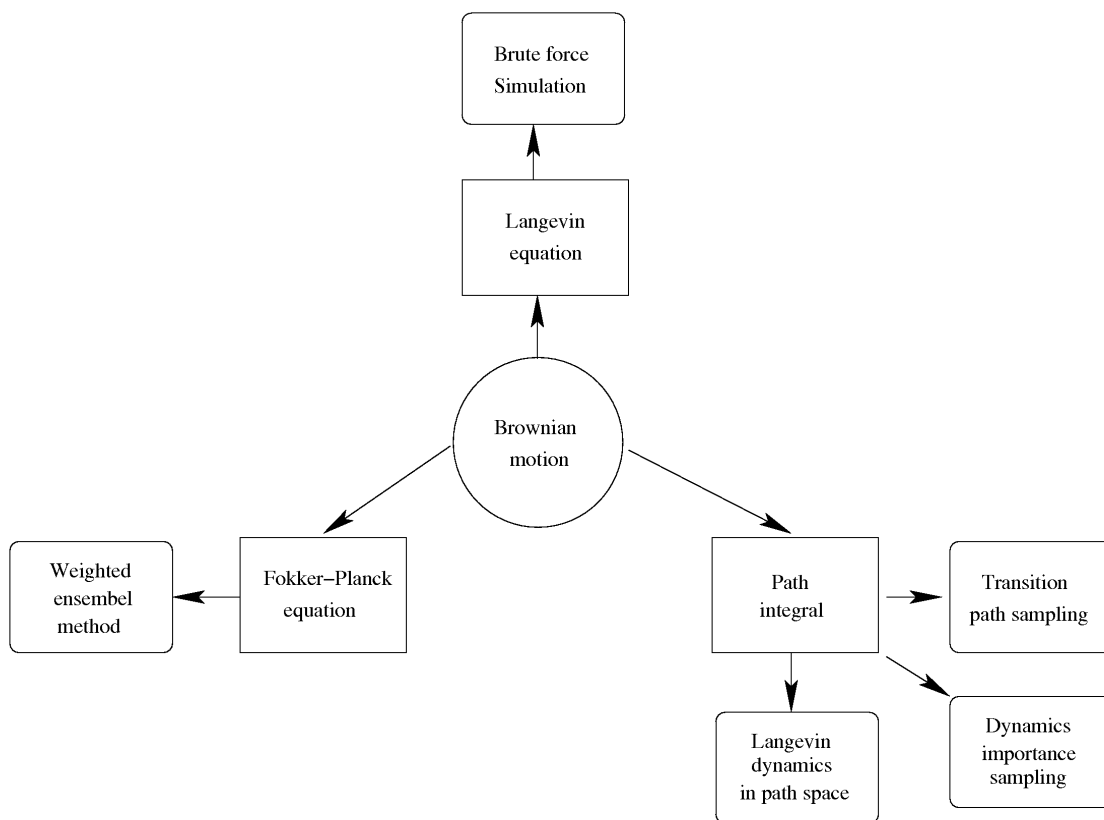


Figure 5: Basic physical ideas

In my research, simulations provide numerical confirmation of analytic results. On the other hand, based on the understanding of theory, we develop more efficient simulation

approaches to study the activated processes.

## D. OUTLINE OF THESIS

This thesis is set up as follows. In Chapter II, we will review the basic theoretical methods of Brownian motion, including the Langevin equation, the Fokker-Planck equation and the path integral technique. In Chapter III, several path sampling and path generating simulation approaches will be introduced. Then we will study the statistics of the duration of transition-events in a class of one-dimensional systems in detail, and also discuss implications for more complex systems in Chapter IV. In Chapter V, we will employ the weighted ensemble method for a model of the protein calmodulin. In Chapter VI we will apply the weighted ensemble method and the transition path sampling method to test system with multiple channels of paths. Summary and discussion of open questions is included in the final Chapter.

## II. THEORY OF BROWNIAN MOTION

### A. INTRODUCTION

#### 1. Historical background of Brownian motion

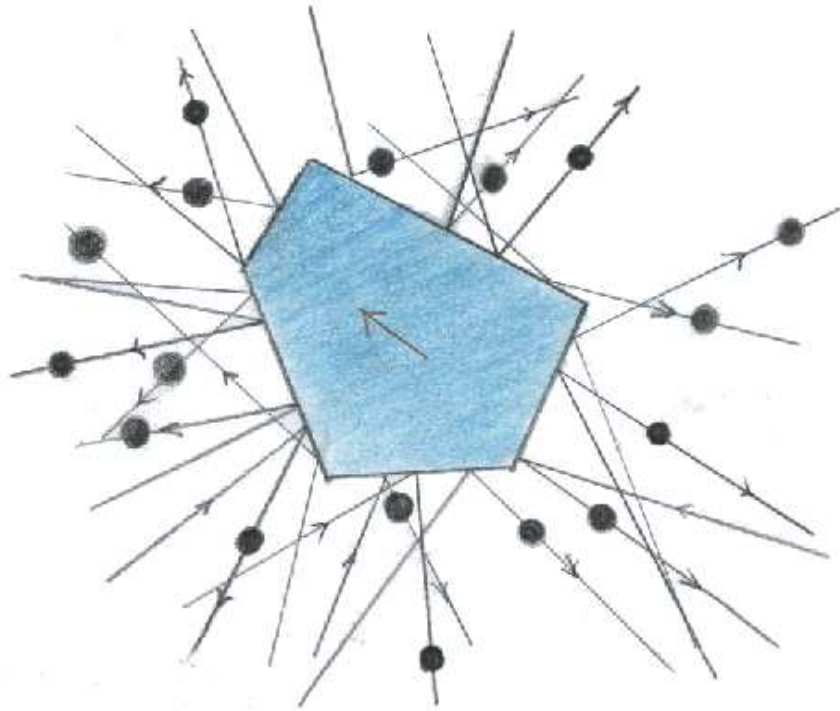


Figure 6: A schematic illustration of Brownian motion.

In 1827, Robert Brown, a botanist, was investigating the behavior of pollen during impregnation. He put granules of the pollen of a wildflower under a microscope and tried to observe their orientation. It is at that time when Brown noticed the incessant motion of these small particles suspended in fluid, which is called Brownian motion nowadays. Later Brown showed that this is a phenomenon of physical, rather than biological origin [10].

There had been no important research results on Brownian motion until 1905 when Einstein published his famous four papers [10]. Compared with the two papers on relativity theory, one paper on the photon hypothesis (ultimately worthy of a Nobel Prize), the paper on Brownian motion is probably the least well known [14]. Nonetheless one sees the brilliance of Einstein's analysis, which has been explained carefully in Gardiner's book [7].

Einstein pointed out that Brownian motion is caused by the impacts on the particle (pollen grain) of the molecules of the liquid, and the motion of the molecules is so complicated that its effect can only be described probabilistically. Then he introduced a separation of time scales, a time interval  $\tau$ , which is much shorter than the observable macroscopic time interval, but long enough that in two successive intervals of duration  $\tau$ , the motions of the particle are independent.

Einstein assumed that for a distribution of free Brownian particles in one-dimensional space, the respective positions will change by  $\Delta$  during time interval  $\tau$ . The displacement  $\Delta$  is different for each particle. The assumption is that there exists a probability density function  $\Phi(\Delta)$ , which satisfies

$$\int_{-\infty}^{\infty} \Phi(\Delta) d\Delta = 1 \quad (\text{II.1})$$

and

$$\Phi(\Delta) = \Phi(-\Delta). \quad (\text{II.2})$$

Let  $n(x, t)dx$  be the number of particles in the interval  $dx$ . Because of the independence of  $\Delta$  in the interval  $\tau$  of its previous history, one obtains

$$\begin{aligned} n(x, t + \tau)dx &= \left( \int_{-\infty}^{\infty} n(x - \Delta, t) \Phi(\Delta) d\Delta \right) dx \\ &= \left( \int_{-\infty}^{\infty} n(x + \Delta, t) \Phi(\Delta) d\Delta \right) dx. \end{aligned} \quad (\text{II.3})$$

For  $\tau$  and  $\Delta$  both small and with  $n(x, t)$  slowly varying on the macroscopic scale, we can expand  $n(x, t + \tau)$  and  $n(x + \Delta, t)$  in Taylor series, which yield

$$n(x, t + \tau) = n(x, t) + \tau \frac{\partial n}{\partial t} + \dots, \quad (\text{II.4})$$

$$n(x + \Delta, t) = n(x, t) + \Delta \frac{\partial n}{\partial x} + \frac{\Delta^2}{2!} \frac{\partial^2 n}{\partial x^2} + \dots. \quad (\text{II.5})$$

Then Eq.(II.3) becomes

$$\begin{aligned} n + \frac{\partial n}{\partial t} \tau &= n \int_{-\infty}^{\infty} \Phi(\Delta) d\Delta + \frac{\partial n}{\partial x} \int_{-\infty}^{\infty} \Delta \Phi(\Delta) d\Delta \\ &+ \frac{\partial^2 n}{\partial x^2} \int_{-\infty}^{\infty} \frac{\Delta^2}{2!} \Phi(\Delta) d\Delta + \dots. \end{aligned} \quad (\text{II.6})$$

Because of the reasonably assumed  $\Phi(\Delta) = \Phi(-\Delta)$ , the second term on the right side vanishes. If we define the diffusion coefficient

$$D = \frac{1}{\tau} \int_{-\infty}^{\infty} \frac{\Delta^2}{2!} \Phi(\Delta) d\Delta, \quad (\text{II.7})$$

Eq.(II.6) becomes

$$\frac{\partial n}{\partial t} = D \frac{\partial^2 n}{\partial x^2} + \mathcal{O}(\Delta^3), \quad (\text{II.8})$$

which is recognized as the differential equation of free diffusion. With open boundary condition its solution is well known as

$$n(x, t) = \frac{N}{\sqrt{4\pi Dt}} \exp\left(-\frac{x^2}{4Dt}\right), \quad (\text{II.9})$$

where  $N$  is the total number of particles. With the help of Eq.(II.9), we can calculate the mean of the square of the displacement in time  $t$ ; it is

$$\begin{aligned} \overline{x^2} &= \int_{-\infty}^{\infty} x^2 \left[ \frac{1}{\sqrt{4\pi Dt}} \exp\left(-\frac{x^2}{4Dt}\right) \right] dx \\ &= 2Dt, \end{aligned} \quad (\text{II.10})$$

which is probably the best known feature of random walks and Brownian motion, namely that the root-mean-square displacement grows at  $\sqrt{t}$ . This result is easily seen to hold in d-dimensional space.

There are several important concepts in Einstein's derivation. In fact Eq.(II.3) later became known as the Chapman-Kolmogorov equation, which contains a basic idea of Markov processes. As we will see Eq.(II.8) is the Fokker-Planck equation for free diffusion. At the time of Einstein's analysis none of these equations and concepts had been derived by the authors for whom they are named [7, 10].

In 1906, Smoluchowski published his results on Brownian motion after Einstein's paper [15]. The time scale  $\tau$  in Einstein's work is mesoscopic, but Smoluchowski's theory is microscopic. Smoluchowski used a more refined model. By beginning with the collision of two hard spheres and the free path kinetic theory of gases, he obtained results that differed from Einstein's (Eq.(II.10)) only by a numerical factor. (The discrepancy arose because of the approximations made in his theory. And Smoluchowski admitted later that Einstein's numerical factor was correct [10].) Compared with Einstein's theory, which is totally based on statistical assumptions, Smoluchowski's work yields more insight on microscopic dynamics. The details can be found in Mazo's book [10].

## 2. Application of Brownian motion

The best known case of Brownian motion is for particles suspended in a fluid; however, there are more exotic Brownian motions, i.e., an electron immersed in a black body radiation field, which is a gas of photons [10]. Brownian motion is also important in biology [16]. Besides ubiquitous cases in the real world, Brownian motion is also a useful mathematical model used to describe such random movements. For example, in Zwanzig's book on nonequilibrium [11], his first sentence is "The theory of Brownian motion is perhaps the simplest approximate way to treat the dynamics of nonequilibrium systems." A chemical or biological macroscopic system in the lab can often be treated as a Brownian particle moving in some abstract space described by a "reaction coordinate". Based on this idea, one famous result is Kramers' law [2], for the passage of particles over a potential barrier, which finds wide application in chemical kinetics and other areas [10]. We will discuss Kramers' work and related analysis in Sec.(II.E.1).

Brownian motion can also serve as a model for stock market fluctuations, and it is not surprising to find the theory of Brownian motion in the books about stochastic calculus for finance [17, 18].

## B. LANGEVIN EQUATION

In 1908, Langevin provided an approach to Brownian motion which he said was “infinitely more simple” than Einstein’s. [19, 20].

In this approach, for a Brownian particle suspended in the liquid, there are two forces on it. One is systematically caused by viscosity of the fluid, and the other is a fluctuating force  $X$ , presumably originating with rapid molecular motions. The equation of motion in the direction of  $x$  is

$$m \frac{d^2 x}{dt^2} = -\gamma \frac{dx}{dt} + X, \quad (\text{II.11})$$

where  $\gamma$  is the friction constant, proportional to the viscosity of the fluid.

### 1. Diffusion coefficient

Eq.(II.11) is known as the Langevin equation for a free Brownian particle moving in  $x$  direction. We can get the coefficient of diffusion from this equation following [7]. Multiply both sides of Eq.(II.11) by  $x$ , obtaining

$$\frac{m}{2} \frac{d^2}{dt^2}(x^2) - mv^2 = -\frac{\gamma}{2} \frac{d(x^2)}{dt} + Xx, \quad (\text{II.12})$$

where  $v = dx/dt$ . For a Brownian particle, its mean kinetic energy (averaged over a large number of particles) in equilibrium is

$$\left\langle \frac{1}{2}mv^2 \right\rangle = \frac{1}{2}k_B T. \quad (\text{II.13})$$

where  $k_B$  is Boltzmann's constant, and  $T$  is the temperature. Averaging Eq.(II.12) in equilibrium yields an equation for  $\langle x^2 \rangle$ :

$$\frac{m}{2} \frac{d^2 \langle x^2 \rangle}{dt^2} + \frac{\gamma}{2} \frac{d \langle x^2 \rangle}{dt} = k_B T, \quad (\text{II.14})$$

where we set  $\langle xX \rangle = 0$  assuming  $X$  is not correlated with the position  $x$ . Then the solution for  $\frac{d \langle x^2 \rangle}{dt}$  from Eq.(II.14) is

$$\frac{d \langle x^2 \rangle}{dt} = \frac{2k_B T}{\gamma} + c \exp\left(-\frac{\gamma t}{m}\right), \quad (\text{II.15})$$

where  $c$  is a constant specified by  $\langle \frac{dx}{dt} x \rangle$  at  $t = 0$ .

The decay time of the second term in Eq.(II.15) is much shorter than any practical observation, usually  $m/\gamma$  is at the order of  $10^{-7} s$  for typical situations. [7, 10], so we ignore it and integrate Eq.(II.15) once more to get

$$\langle x^2 \rangle - \langle x_0^2 \rangle = \frac{2k_B T}{\gamma} t. \quad (\text{II.16})$$

Comparison with Eq.(II.10), Eq.(II.16) provides the diffusion coefficient:

$$D = \frac{k_B T}{\gamma}. \quad (\text{II.17})$$

Eq.(II.17) is known as the Einstein relation.

## 2. Over-Damped Langevin equation

If a Brownian particle moves in a one-dimensional potential field  $U(x)$ , another force term will appear in Langevin equation, which becomes

$$m \frac{d^2 x}{dt^2} = -\frac{\partial U}{\partial x} - \gamma \frac{dx}{dt} + X. \quad (\text{II.18})$$

If the viscosity of the medium is so large that the Brownian particle will arrive at a constant velocity immediately (which means the accelerating period  $m/\gamma$  is much shorter than timescale  $\tau$  mentioned in Sec. II.A.1), the left side of Eq.(II.18) can be set to equal zero. Then the Langevin equation becomes

$$0 = -\frac{\partial U}{\partial x} - \gamma \frac{dx}{dt} + X, \quad (\text{II.19})$$

The velocity in this short timescale  $\tau$  becomes

$$\frac{dx}{dt} = \frac{F}{\gamma} + R(t), \quad (\text{II.20})$$

where

$$F = -\frac{\partial U(x)}{\partial x}. \quad (\text{II.21})$$

is the physical force in  $x$  direction based on the potential energy  $U(x)$ , and  $R(t) = X/\gamma$  is the contribution from noise. In this thesis we will only study Gaussian white noise with zero mean and correlation

$$\langle R(t)R(t') \rangle = \left( \frac{2k_B T}{\gamma} \right) \delta(t - t') = 2D\delta(t - t'). \quad (\text{II.22})$$

The constant before the delta function is determined so that Eq.(II.13) is satisfied [8]. Eq.(II.20) is known as the over-damped Langevin equation. Individual realizations of the noise in Eq.(II.20) generate stochastic trajectories  $x(t)$ , which are routinely simulated numerically as described in Section III.B.

## C. FOKKER-PLANCK EQUATION

### 1. Derivation of Fokker-Planck equation

In this section, we will derive the Fokker-Planck equation from the over-damped Langevin equation in one dimension (II.20) following Zwanzig's book [11]. The Fokker-Planck equation gives the time evolution of the probability density function for the system. A more complete discussion of the Fokker-Planck equation corresponding to the over-damped Langevin equation and related applications appears in [7].

At the beginning, we need to assume that the noise is white and has a Gaussian distribution, which has zero mean and satisfies

$$\langle R(t)R(t') \rangle = 2D\delta(t - t'). \quad (\text{II.23})$$

One defines  $P(x, t)$  as the probability distribution of  $x$  at time  $t$ .  $P(x, t)$  must satisfy the conservation law

$$\frac{\partial P(x, t)}{\partial t} + \frac{\partial}{\partial x} [v(x, t)P(x, t)] = 0, \quad (\text{II.24})$$

which means the time derivative of  $P(x, t)$  is balanced by the divergence of the flux. After replacing the velocity  $v(x, t)$  by the right side of Eq.(II.20), we get

$$\frac{\partial P(x, t)}{\partial t} + \frac{\partial}{\partial x} \left[ \frac{F(x)}{\gamma} P(x, t) + R(t)P(x, t) \right] = 0. \quad (\text{II.25})$$

Following [11], we now define an operator  $\mathcal{L}$ , whose action on any function  $\Phi(x, t)$  is

$$\mathcal{L}\Phi(x, t) \equiv \frac{\partial}{\partial x} \left[ \frac{F(x)}{\gamma} \Phi(x, t) \right]. \quad (\text{II.26})$$

For a noise-free fully deterministic case, we take  $P = P_0$  satisfying

$$\frac{\partial P_0(x, t)}{\partial t} = -\mathcal{L}P_0(x, t), \quad (\text{II.27})$$

the formal solution of Eq.(II.27) is

$$P_0(x, t) = e^{-t\mathcal{L}}P_0(x, 0), \quad (\text{II.28})$$

where  $P_0(x, 0)$  is the initial value of  $P_0(x, t)$  at  $t = 0$ .

Now we add back the noise term for Eq.(II.27), and it becomes

$$\frac{\partial P(x, t)}{\partial t} = -\mathcal{L}P(x, t) - \frac{\partial}{\partial x}[R(t)P(x, t)]. \quad (\text{II.29})$$

The formal solution of Eq.(II.29) is

$$P(x, t) = P_0(x, t) - P'(x, t) = e^{-t\mathcal{L}}P_0(x, 0) - \int_0^t ds e^{-(t-s)\mathcal{L}} \frac{\partial}{\partial x} R(s)P(x, s). \quad (\text{II.30})$$

Let's check it briefly. One finds explicitly

$$\begin{aligned} \frac{\partial P'(x, t)}{\partial t} &= \frac{\partial}{\partial t} \left[ e^{-t\mathcal{L}} \int_0^t ds e^{s\mathcal{L}} \frac{\partial}{\partial x} R(s)P(x, s) \right] \\ &= -\mathcal{L} \left[ e^{-t\mathcal{L}} \int_0^t ds e^{s\mathcal{L}} \frac{\partial}{\partial x} R(s)P(x, s) \right] + \frac{\partial}{\partial x} R(t)P(x, t) \\ &= -\mathcal{L}P' + \frac{\partial}{\partial x} R(t)P(x, t), \end{aligned} \quad (\text{II.31})$$

so that

$$\begin{aligned} \frac{\partial P(x, t)}{\partial t} &= \frac{\partial P_0(x, t)}{\partial t} - \frac{\partial P'(x, t)}{\partial t} \\ &= -\mathcal{L}P_0(x, t) + \mathcal{L}P' - \frac{\partial}{\partial x} R(t)P(x, t) \\ &= -\mathcal{L}P(x, t) - \frac{\partial}{\partial x} R(t)P(x, t), \end{aligned} \quad (\text{II.32})$$

confirming that a particular solution has been found.

By replacing  $P(x, t)$  in the second term of Eq.(II.29) with this symbolic solution, it becomes

$$\begin{aligned} \frac{\partial P(x, t)}{\partial t} &= -\mathcal{L}P(x, t) - \frac{\partial}{\partial x} [R(t)e^{-t\mathcal{L}}P_0(x, 0)] \\ &\quad + \frac{\partial}{\partial x} \left[ R(t) \int_0^t ds e^{-(t-s)\mathcal{L}} \frac{\partial}{\partial x} R(s)P(x, s) \right]. \end{aligned} \quad (\text{II.33})$$

Before we take the noise average of Eq.(II.33), a lemma about Gaussian random variables is required. Let's consider a set of Gaussian random variables  $\vec{R} = [R_1, R_2, R_3 \dots R_n]$ . For simplicity, all these random variables have zero mean. The density distribution function is

$$\rho(\vec{R}) = \frac{1}{\sqrt{\det(2\pi M)}} \exp \left( -\frac{1}{2} \sum_j \sum_k R_j (M^{-1})_{jk} R_k \right), \quad (\text{II.34})$$

where  $M_{jk}$  is their mean squared fluctuations

$$M_{jk} = \int d\vec{R} R_j R_k \rho(\vec{R}). \quad (\text{II.35})$$

In fact we will only require Gaussian random variables without correlations in this thesis, but let's keep the general format now. Using Eq.(II.34) and the symmetry of  $M$ , one finds

$$\begin{aligned} - \sum_k M_{jk} \frac{\partial}{\partial R_k} \rho(\vec{R}) &= - \sum_k M_{jk} \rho(\vec{R}) \left( - \sum_{j'} (M^{-1})_{j'k} R_{j'} \right) \\ &= \sum_k \sum_{j'} (M^{-1})_{j'k} M_{kj} R_{j'} \rho(\vec{R}) \\ &= R_j \rho(\vec{R}). \end{aligned} \quad (\text{II.36})$$

Then the average of  $R_j \mathcal{F}(\vec{R})$  over noise, where  $\mathcal{F}(\vec{R})$  is an arbitrary function of  $\vec{R}$ , is

$$\begin{aligned} \langle R_j \mathcal{F}(\vec{R}) \rangle &= \int [R_j \mathcal{F}(\vec{R})] \rho(\vec{R}) d\vec{R} \\ &= - \int d\vec{R} \sum_k M_{jk} \mathcal{F}(\vec{R}) \frac{\partial}{\partial R_k} \rho(\vec{R}) \\ &= \int d\vec{R} \rho(\vec{R}) \frac{\partial}{\partial R_k} \left[ \sum_k M_{jk} \mathcal{F}(\vec{R}) \right] \\ &= \sum_k M_{jk} \left\langle \frac{\partial}{\partial R_k} \mathcal{F}(\vec{R}) \right\rangle. \end{aligned} \quad (\text{II.37})$$

Eq.(II.37) will help us to calculate the noise average for the last right term in Eq.(II.33). In the integral over time from 0 to  $t$ , the noises in different time intervals  $ds$ , can be treated as a set of Gaussian random variables, thus

$$\begin{aligned} &\left\langle \frac{\partial}{\partial x} \left[ R(t) \int_0^t ds e^{-(t-s)\mathcal{L}} \frac{\partial}{\partial x} R(s) P(x, s) \right] \right\rangle \\ &= \frac{\partial}{\partial x} \left[ \int_0^t ds e^{-(t-s)\mathcal{L}} \left\langle R(t) \frac{\partial}{\partial x} R(s) P(x, s) \right\rangle \right] \\ &= \frac{\partial}{\partial x} \left\{ \int_0^t ds e^{-(t-s)\mathcal{L}} \left[ \sum_{s'} M_{ts'} \left\langle \frac{\partial}{\partial R(s')} \left( \frac{\partial}{\partial x} R(s) P(x, s) \right) \right\rangle \right] \right\}. \end{aligned} \quad (\text{II.38})$$

Now let's check the part in the square brackets. There are noise factors  $R(s')$  implicit in  $P(x, s)$ , but their time points are previous to  $s$ , so  $s' \leq s$ ; otherwise the derivative with respect to  $R(s')$  is zero. Then one can divide the summation into two parts

$$\begin{aligned} & \sum_{s'} M_{ts'} \left\langle \frac{\partial}{\partial R(s')} \left( \frac{\partial}{\partial x} R(s) P(x, s) \right) \right\rangle \\ = & \sum_{s' < s} M_{ts'} \left\langle \frac{\partial}{\partial R(s')} \left( \frac{\partial}{\partial x} R(s) P(x, s) \right) \right\rangle + M_{ts} \left\langle \frac{\partial}{\partial R(s)} \left( \frac{\partial}{\partial x} R(s) P(x, s) \right) \right\rangle \end{aligned} \quad (\text{II.39})$$

Eq.(II.23) shows the assumption that the noise is delta-function correlated, so

$$M_{ts} = 2D\delta(s - t), \quad (\text{II.40})$$

which means the summation part in the second line of Eq.(II.39) will always vanish because  $s' < s \leq t$ . Continuing the calculation of Eq.(II.38)

$$\begin{aligned} & \frac{\partial}{\partial x} \left\{ \int_0^t ds e^{-(t-s)\mathcal{L}} \left[ \sum_{s'} M_{ts'} \left\langle \frac{\partial}{\partial R(s')} \left( \frac{\partial}{\partial x} R(s) P(x, s) \right) \right\rangle \right] \right\} \\ = & \frac{\partial}{\partial x} \left\{ \int_0^t ds e^{-(t-s)\mathcal{L}} M_{ts} \left\langle \frac{\partial}{\partial R(s)} \left( \frac{\partial}{\partial x} R(s) P(x, s) \right) \right\rangle \right\} \\ = & \frac{\partial}{\partial x} \left[ \int_0^t ds (2D)\delta(s - t) e^{-(t-s)\mathcal{L}} \left\langle \frac{\partial}{\partial x} P(x, s) \right\rangle \right] \\ = & D \frac{\partial^2}{\partial x^2} \langle P(x, t) \rangle. \end{aligned} \quad (\text{II.41})$$

For the other term containing  $R(t)$  in Eq.(II.33),  $e^{-t\mathcal{L}} P_0(x, 0) = P_0(x, t)$  is uncorrelated with  $R(t)$ , so the average over noise becomes

$$\left\langle \frac{\partial}{\partial x} [R(t) e^{-t\mathcal{L}} P_0(x, 0)] \right\rangle = 0, \quad (\text{II.42})$$

using  $\langle R(t) \rangle = 0$ .

Finally, the noise average of Eq.(II.33) is

$$\frac{\partial}{\partial t} \langle P(x, t) \rangle = -\frac{\partial}{\partial x} \left[ \frac{F(x)}{\gamma} \langle P(x, t) \rangle \right] + D \frac{\partial^2}{\partial x^2} \langle P(x, t) \rangle \quad (\text{II.43})$$

We can omit the angular brackets because we will only deal with the average distribution.

The Fokker-Planck equation for over-damped Brownian motion is then

$$\frac{\partial P(x, t)}{\partial t} = -\frac{\partial}{\partial x} \left\{ -D \left[ \frac{dU^*(x)}{dx} + \frac{\partial}{\partial x} \right] P(x, t) \right\}, \quad (\text{II.44})$$

where  $U^*(x) = U(x)/k_B T$  is the dimensionless physical potential.

The Fokker-Planck equation can be derived from the master equation, readers who are interested can find it in van Kampen's books [9].

## 2. Discussion of Fokker-Planck equation

In this section we introduce some properties and operations that will be useful in what follows.

### a. Current

In Sec.(II.C.1), the Fokker-Planck equation was derived from the over-damped Langevin equation, and the conservation law

$$\frac{\partial P(x, t)}{\partial t} = -\frac{\partial J(x, t)}{\partial x}, \quad (\text{II.45})$$

where  $J(x, t)$  is the current. We compare Eq.(II.45) with Eq.(II.44) and identify

$$J(x, t) = -D \left[ \frac{dU^*(x)}{dx} + \frac{\partial}{\partial x} \right] P(x, t), \quad (\text{II.46})$$

where the first term represents the systematic drift contribution while the second term represents the diffusion contribution.

### b. Boundary conditions

To get the time evolution of the probability density function for the system, one needs to solve the Fokker-Planck equation with appropriate initial and boundary conditions. Here several simple boundary conditions are considered [8].

- Reflecting barrier (R)

If the Brownian particle cannot leave a region, at the boundary  $a$  it will be reflected.

Because the net flow across the boundary is zero, the current satisfies

$$J(a, t) = 0. \quad (\text{II.47})$$

- Absorbing barrier (A)

If the Brownian particle reaches this type boundary  $a$ , it will be removed from the system immediately. The boundary acts as an absorbing wall and the probability satisfies

$$P(a, t) = 0. \quad (\text{II.48})$$

- Natural boundary condition (N)

If we have reflecting walls at  $x \rightarrow -\infty$  and  $x \rightarrow \infty$ , the probability currents will vanish there. The total probability is conserved with  $\int_{-\infty}^{\infty} P(x, t) dx = 1$ . This boundary condition is called *natural boundary condition*, which is represented by

$$J(-\infty, t) = J(\infty, t) = 0. \quad (\text{II.49})$$

- Periodic boundary condition (P)

If the process takes place in an interval  $[a, b]$  whose two ends are identified with each other (as if the interval is wrapped in a ring), the current and probability will satisfy

$$\begin{aligned} \lim_{x \rightarrow b^-} P(x, t) &= \lim_{x \rightarrow a^+} P(x, t) \\ \lim_{x \rightarrow b^-} J(x, t) &= \lim_{x \rightarrow a^+} J(x, t). \end{aligned} \quad (\text{II.50})$$

### c. Construction of a Hermitian operator [8]

It will prove useful to convert the operator  $\mathcal{L}_{FP}$  to Hermitian form. Let us consider again the Fokker-Planck operator

$$\begin{aligned} \mathcal{L}_{FP} &= D \frac{\partial}{\partial x} \left( \frac{dU^*}{dx} + \frac{\partial}{\partial x} \right) \\ &= D \frac{\partial}{\partial x} \exp(-U^*) \frac{\partial}{\partial x} \exp(U^*), \end{aligned} \quad (\text{II.51})$$

which is not a Hermitian operator. If there are two functions  $P_1$  and  $P_2$ , both satisfying the same boundary condition, which can be the natural boundary condition (N), or periodic

boundary condition (P), or any combination of reflecting (R) and absorbing (A) boundary conditions, we have

$$\begin{aligned}
& \int_a^b P_1 \exp(U^*) \mathcal{L}_{FP} P_2 dx \\
&= \int_a^b P_1 \exp(U^*) D \frac{\partial}{\partial x} \exp(-U^*) \frac{\partial}{\partial x} \exp(U^*) P_2 dx \\
&= P_1 \exp(U^*) \exp(-U^*) D \frac{\partial}{\partial x} \exp(U^*) P_2 \Big|_a^b \\
&\quad - \int_a^b \left[ \frac{\partial}{\partial x} (P_1 \exp(U^*)) \right] D \exp(-U^*) \left[ \frac{\partial}{\partial x} (\exp(U^*) P_2) \right] dx \\
&= -P_1 \exp(U^*) J_2|_a^b - P_2 \exp(U^*) \exp(-U^*) D \frac{\partial}{\partial x} \exp(U^*) P_1 \Big|_a^b \\
&\quad + \int_a^b P_2 \exp(U^*) D \frac{\partial}{\partial x} \exp(-U^*) \frac{\partial}{\partial x} \exp(U^*) P_1 dx \\
&= -P_1 \exp(U^*) J_2|_a^b + P_2 \exp(U^*) J_1|_a^b \\
&\quad + \int_a^b P_2 \exp(U^*) D \frac{\partial}{\partial x} \exp(-U^*) \frac{\partial}{\partial x} \exp(U^*) P_1 dx. \tag{II.52}
\end{aligned}$$

In deriving Eq.(II.52), we have used

$$D \frac{\partial}{\partial x} \exp(U^*(x)) P(x, t) = -\exp(U^*) J(x, t), \tag{II.53}$$

where  $J(x, t)$  is the probability current. Because of the boundary conditions, we have

$$P_1 \exp(U^*) J_2|_a^b = P_2 \exp(U^*) J_1|_a^b = 0. \tag{II.54}$$

Then from Eq.(II.52) the operator  $\exp(U^*) \mathcal{L}_{FP}$  is a Hermitian operator, which satisfies

$$\int_a^b P_1 \exp(U^*) \mathcal{L}_{FP} P_2 dx = \int_a^b P_2 \exp(U^*) \mathcal{L}_{FP} P_1 dx. \tag{II.55}$$

#### d. Construction of a Schrödinger-like operator [8]

We have already shown that  $\exp(U^*)\mathcal{L}_{FP}$  is a Hermitian operator; then

$$\begin{aligned}\mathcal{L}_s &\equiv \exp(-U^*/2)\exp(U^*)\mathcal{L}_{FP}\exp(-U^*/2) \\ &= \exp(U^*/2)\mathcal{L}_{FP}\exp(-U^*/2)\end{aligned}\tag{II.56}$$

is also a Hermitian operator. Expanding  $\mathcal{L}_s$ , one finds

$$\begin{aligned}\mathcal{L}_s &= \exp(U^*/2)\mathcal{L}_{FP}\exp(-U^*/2) \\ &= \exp(U^*/2)D\frac{\partial}{\partial x}\left(\frac{dU^*}{dx} + \frac{\partial}{\partial x}\right)\exp(-U^*/2) \\ &= D\exp(U^*/2)\frac{\partial}{\partial x}\left[\frac{dU^*}{dx}\exp(-U^*/2)\right] + D\exp(U^*/2)\frac{\partial^2}{\partial x^2}\exp(-U^*/2) \\ &= D\frac{\partial^2}{\partial x^2} + \frac{D}{2}\frac{d^2U^*}{dx^2} - \frac{D}{4}\left(\frac{dU^*}{dx}\right)^2 \\ &= D\frac{\partial^2}{\partial x^2} - V_S(x),\end{aligned}\tag{II.57}$$

where

$$V_S = -\frac{D}{2}\frac{d^2U^*}{dx^2} + \frac{D}{4}\left(\frac{dU^*}{dx}\right)^2.\tag{II.58}$$

Hence we have changed the Fokker-Planck operator  $\mathcal{L}_{FP}$  into a Schrödinger-like operator  $\mathcal{L}_s$ .

In brief, if we define  $P_S \equiv \exp(U^*/2)P$ ,  $P_S$  will obey a Schrödinger-like equation

$$-\frac{dP_S}{dt} = \left[-D\frac{\partial^2}{\partial x^2} + V_S(x)\right]P_S,\tag{II.59}$$

where  $V_S$  is given by Eq.(II.58). The Schrödinger equation must be one of the most studied partial differential equations in physics, so now techniques developed for the Schrödinger equation can be borrowed for application to Fokker-Planck equation [8].

**e. Solution of the Fokker-Planck equation expressed as an eigenfunction expansion** [8]

A separation ansatz for  $P(x, t)$

$$P(x, t) = \phi(x) \exp(-\lambda t), \quad (\text{II.60})$$

will give us

$$\mathcal{L}_{FP}\phi = -\lambda\phi, \quad (\text{II.61})$$

where  $\phi(x)$  and  $\lambda$  are the eigenfunction and eigenvalue respectively of the Fokker-Planck equation. Let  $\psi(x) = \exp(U^*(x)/2)\phi(x)$ ; then

$$\mathcal{L}_s\psi = -\lambda\psi, \quad (\text{II.62})$$

where  $\mathcal{L}_s$  has been defined by Eq.(II.56).  $\mathcal{L}_s$  is a Schrödinger-like operator, so following the standard derivation in quantum mechanics, we can get the orthogonality and completeness of the eigenfunctions  $\psi_n$ . For discrete eigenvalues,

$$\begin{aligned} \int_a^b \psi_n \psi_m dx &= \int_a^b \exp(U^*) \phi_n \phi_m dx = \delta_{m,n}, \\ \delta(x - x') &= \sum_n \psi_n(x) \psi(x') \\ &= \exp\left[\frac{1}{2}(U^*(x) + U^*(x'))\right] \sum_n \phi_n(x) \phi(x'). \end{aligned} \quad (\text{II.63})$$

Because  $\mathcal{L}_s$  is a Hermitian operator, the eigenvalues  $\lambda_n$  are real. We also can prove that they will be non-negative when the boundary condition is of the type (R), (A), (N), (P), or any combination of (R) and (A),

$$\begin{aligned} \lambda_n &= - \int_a^b \psi_n \mathcal{L}_s \psi_n dx \\ &= - \int_a^b \phi_n \exp(U^*) \mathcal{L}_{FP} \phi_n dx \\ &= - \int_a^b \phi_n \exp(U^*) D \frac{\partial}{\partial x} \exp(-U^*) \frac{\partial}{\partial x} \exp(U^*) \phi_n dx \\ &= -D \phi_n \frac{\partial}{\partial x} \exp(U^*) \phi_n \Big|_a^b + \int_a^b D \exp(-U^*) \left[ \frac{\partial}{\partial x} (\exp(U^*) \phi_n) \right]^2 dx \\ &= \int_a^b D \exp(-U^*) \left[ \frac{\partial}{\partial x} (\exp(U^*) \phi_n) \right]^2 dx \geq 0. \end{aligned} \quad (\text{II.64})$$

If the boundary conditions and potential admit a solution with  $\lambda_0 = 0$ , then  $P(x, t) = \psi_0$ , represents a stationary solution.

#### D. PATH INTEGRAL REPRESENTATION

Path integral methods provide a useful tool and a different perspective for the study of Brownian motion [12, 13, 21]. In this section, we will following Wiegel's book [12] to derive the path integral approach to Brownian motion and its approximation.

##### 1. A simple illustration

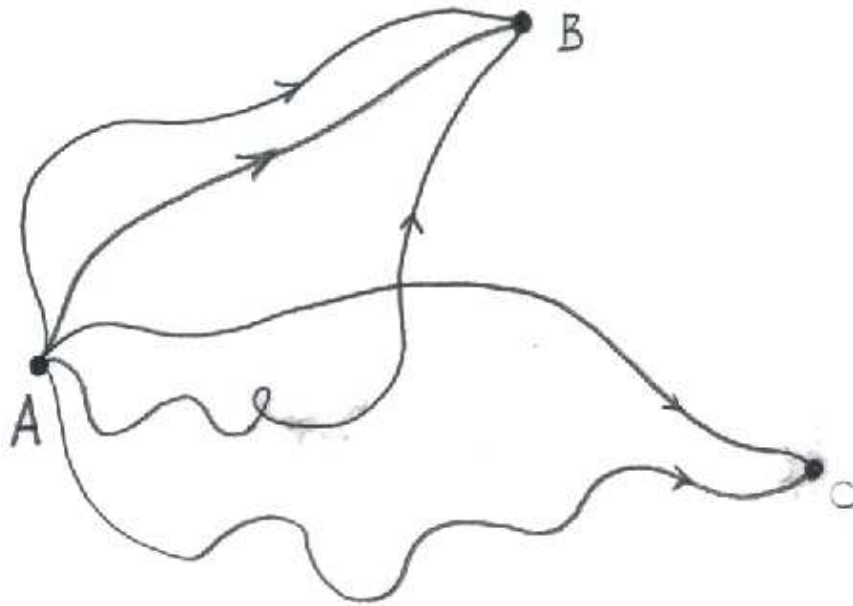


Figure 7: A simple illustration for the basic idea of path integral.

Before we jump into tons of equations, for readers who are not familiar with the basic idea of path integral, let's study a simple illustration first. In Fig. 7, there is a particle at point  $A$  at time  $t_0$ . Let  $P(x, t)$  represent the probability that the particle will be found at position  $x$  at

time  $t$ , then  $P(A, t_0) = \delta(x - A)$  is our initial condition. How can we calculate an arbitrary  $P(x, t)$  using path integral techniques?

In Fig. 7, we show two final points  $B$  and  $C$  at time  $t$ . After careful search, suppose there are only three paths found connecting points  $A$  and  $B$  during this time interval, their probabilities are  $p_{B1}$ ,  $p_{B2}$  and  $p_{B3}$ . For point  $C$ , suppose there are two paths with probabilities  $p_{C1}$  and  $p_{C2}$ . Then we will come to conclusion that

$$\frac{P(B, t)}{P(C, t)} = \frac{p_{B1} + p_{B2} + p_{B3}}{p_{C1} + p_{C2}}. \quad (\text{II.65})$$

Roughly, this is the basic idea of path integral. But for a real case, it will be much more difficult, since usually there are an infinite numbers of paths in phase space connecting the initial and final states, and even for one particular trajectory, the system can walk through it with infinitely diverse velocity histories. To study the Brownian motion, formal path integral methods will take care all the possible paths and provide a formal solution of the Fokker-Planck equation.

## 2. Path integral formulation for free Brownian motion

First let's consider the free Brownian motion (i.e.,  $U^* = 0$ ), which is described by the equation and initial condition

$$\begin{aligned} \frac{\partial P(x, t)}{\partial t} &= D \frac{\partial^2 P(x, t)}{\partial x^2} \\ P(x, t_0) &= \delta(x - x_0). \end{aligned} \quad (\text{II.66})$$

The solution is well known as (see, e.g. [7])

$$P(x, t) = [4\pi D(t - t_0)]^{-1/2} \exp \left[ -\frac{(x - x_0)^2}{4D(t - t_0)} \right], (t > t_0). \quad (\text{II.67})$$

Eq.(II.67) is variously called the Green function for the free diffusion equation or the propagator of the free Brownian particle.

Path integrals will calculate the total probability of paths connecting  $x_0$  at time  $t_0$  and  $x$  at time  $t$ . If we cut the time interval  $(t_0, t)$  into  $(N + 1)$  equal intervals  $\epsilon$ , the question reduces

to finding the probability a particle is at the sequence of coordinates  $(x_0, x_1, x_2 \dots x_N, x)$  at corresponding times  $(t_0, t_1, t_2 \dots t_N, t)$  within ranges  $(0, dx_1, dx_2 \dots dx_N, 0)$ . It is obvious that this probability would equal the product of successive propagators

$$(4\pi D\epsilon)^{-(N+1)/2} \exp \left[ -\frac{1}{4D\epsilon} \sum_{j=0}^{j=N} (x_{j+1} - x_j)^2 \right] \prod_{j=1}^{j=N} dx_j, \quad (\text{II.68})$$

where  $x_{N+1}$  equals  $x$ . While taking the limit  $\epsilon \rightarrow 0$ ,  $N \rightarrow \infty$  and  $(N + 1)\epsilon = (t - t_0)$ , the exponential part can be written as

$$\exp \left[ -\frac{1}{4D} \int_{t_0}^t \left( \frac{dx}{d\tau} \right)^2 d\tau \right]. \quad (\text{II.69})$$

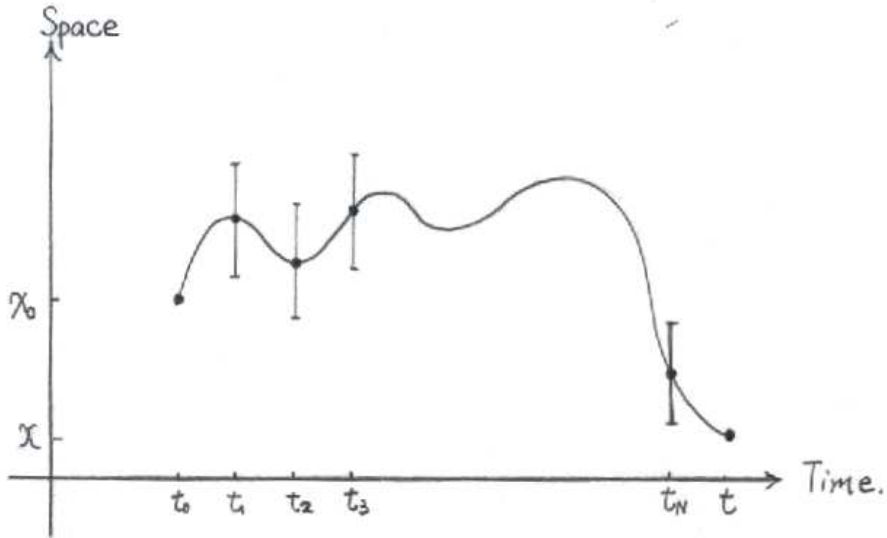


Figure 8: A path goes through the sequence of coordinates  $(x_0, x_1, x_2 \dots x_N, x)$  at corresponding times  $(t_0, t_1, t_2 \dots t_N, t)$  within ranges  $(0, dx_1, dx_2 \dots dx_N, 0)$ .

Then the propagator of a free Brownian particle can be symbolically written

$$P(x, t) = \int_{x_0, t_0}^{x, t} \exp \left[ -\frac{1}{4D} \int_{t_0}^t \left( \frac{dx}{d\tau} \right)^2 d\tau \right] d[x(\tau)], \quad (\text{II.70})$$



Then we can explicitly take the limit

$$\begin{aligned}
P(x, t) &= (4\pi D\epsilon)^{-(N+1)/2} \int_{-\infty}^{\infty} \cdots \int_{-\infty}^{\infty} \prod_{i=1}^N dx_i \exp \left[ -\frac{1}{4D\epsilon} \sum_{j=0}^{j=N} (x_{j+1} - x_j)^2 \right] \\
&= (4\pi D\epsilon)^{-(N+1)/2} \pi^{N/2} (N+1)^{-1/2} (4D\epsilon)^{N/2} \exp \left\{ \frac{1}{4D\epsilon} \left[ \left( \frac{1}{4} \right) \frac{N}{N+1} (2x)^2 - x^2 \right] \right\} \\
&= \frac{1}{\sqrt{4\pi D\epsilon(N+1)}} \exp \left[ -\frac{x^2}{4D\epsilon(N+1)} \right] \\
&= \frac{1}{\sqrt{4\pi Dt}} \exp \left( -\frac{x^2}{4Dt} \right), \tag{II.77}
\end{aligned}$$

which is in agreement with Eq.(II.67).

### 3. Path integral formulation for Brownian motion in an absorbing medium

In this section we study Brownian motion in a medium in which the particle can be annihilated with a probability  $A(x, t)$ . The result will help us to give the path integral for Brownian motion in a field of force later. The Fokker-Planck equation for this problem is [12]

$$\begin{aligned}
\frac{\partial P(x, t)}{\partial t} &= D \frac{\partial^2 P(x, t)}{\partial x^2} - A(x, t)P(x, t) \\
P(x, t_0) &= \delta(x - x_0). \tag{II.78}
\end{aligned}$$

Let us ignore diffusion at first. In a short time interval  $[\tau, \tau + \Delta\tau]$ , the probability change for a stationary particle is

$$dP(x, t) = -P(x, t)A(x, t)dt. \tag{II.79}$$

If the time interval is very short so that  $A(x, t)$  will stay as a constant  $A(x, \tau)$  during  $\Delta\tau$ , the solution of Eq.(II.79) is

$$P(x, \tau + \Delta\tau) = P_0(x, \tau) \exp(-A(x, \tau)\Delta\tau), \tag{II.80}$$

where  $P_0$  is the initial probability. Then for a path of a Brownian particle, the surviving probability is

$$\exp \left[ - \int_{t_0}^t A(x(\tau), \tau) d\tau \right], \quad (\text{II.81})$$

and the propagator of this Brownian particle in this medium is

$$P(x, t) = \int_{x_0, t_0}^{x, t} \exp \left[ - \frac{1}{4D} \int_{t_0}^t \left( \frac{dx}{d\tau} \right)^2 d\tau - \int_{t_0}^t A(x(\tau), \tau) d\tau \right] d[x(\tau)]. \quad (\text{II.82})$$

This result will be the key to finding the path integral of Brownian motion in a field of force in the next subsection.

#### 4. Path integral formulation of Brownian motion in a field of force

Now we are ready to give the path integral formulation for Brownian motion in a field of force. The Fokker-Planck equation is

$$\frac{\partial P(x, t)}{\partial t} = - \frac{\partial}{\partial x} \left\{ -D \left[ \frac{dU^*(x)}{dx} + \frac{\partial}{\partial x} \right] P(x, t) \right\}, \quad (\text{II.83})$$

Let's write

$$P(x, t) = \exp(-U^*/2) P_s(x, t). \quad (\text{II.84})$$

In Sec.(II.C.2) we showed that this will change the Fokker-Planck equation into a Schrödinger-like equation

$$\frac{\partial P_s(x, t)}{\partial t} = \left( D \frac{\partial^2}{\partial x^2} - V_s(x) \right) P_s(x, t), \quad (\text{II.85})$$

where  $V_s$  is given by Eq.(II.58). By comparing with Eq.(II.78), one knows the normalized path integral for  $P_s$  has already been given by Eq.(II.82). From the initial condition

$$P(x, t_0) = \delta(x - x_0), \quad (\text{II.86})$$

and Eq(II.84), the initial condition for  $P_s(x, t)$  is

$$P_s(x, t_0) = \exp(U^*(x_0)/2) \delta(x - x_0). \quad (\text{II.87})$$

Then the path integral for  $P_s$  is

$$P_s(x, t) = \exp(U^*(x_0)/2) \int_{x_0, t_0}^{x, t} \exp \left[ -\frac{1}{4D} \int_{t_0}^t \left( \frac{dx}{d\tau} \right)^2 d\tau - \int_{t_0}^t V_s(x(\tau), \tau) d\tau \right] d[x(\tau)]. \quad (\text{II.88})$$

Substituting Eq.(II.88) into Eq.(II.84), we get the propagator for Brownian motion in a field of force [12]

$$P(x, t) = \exp \left( \frac{U^*(x_0) - U^*(x)}{2} \right) \int_{x_0, t_0}^{x, t} \exp \left[ -\frac{1}{4D} \int_{t_0}^t \left( \frac{dx}{d\tau} \right)^2 d\tau - \int_{t_0}^t V_s(x(\tau), \tau) d\tau \right] d[x(\tau)]. \quad (\text{II.89})$$

## 5. Optimal path

From Eq.(II.89), one can identify the probability-density function for the Brownian particle following a specific trajectory  $x(\tau)$  is

$$\begin{aligned} W[x(\tau)] &\equiv \exp \left[ \frac{U^*(x_0) - U^*(x)}{2} - \frac{1}{4D} \int_{t_0}^t \left( \frac{dx}{d\tau} \right)^2 d\tau - \int_{t_0}^t V_s d\tau \right] \\ &= \exp \left( \frac{U^*(x_0) - U^*(x)}{2} \right) \exp \left\{ - \int_{t_0}^t \mathbb{L}[x(\tau)] d\tau \right\}, \end{aligned} \quad (\text{II.90})$$

where

$$\mathbb{L}[x(\tau)] = \frac{1}{4D} \left( \frac{dx}{d\tau} \right)^2 + V_s. \quad (\text{II.91})$$

The extremal (optimal) path will minimize  $\int_{t_0}^t \mathbb{L} d\tau$  and will satisfy equation [23]

$$\frac{\partial \mathbb{L}}{\partial x} - \frac{d}{d\tau} \frac{\partial \mathbb{L}}{\partial \dot{x}} = 0, \quad (\text{II.92})$$

where  $\dot{x} = \frac{dx}{d\tau}$ . Substituting Eq.(II.91) into Eq.(II.92), the optimal trajectory will satisfy

$$\ddot{x}_c = 2D \frac{dV_s}{dx_c}. \quad (\text{II.93})$$

Note that from Eq.(II.92), in the time interval of  $(t - t_0)$ , the optimal path  $x_c(t)$  of the Brownian particle connecting  $x_0$  and  $x$  is identical to the trajectory of a fictitious Newtonian particle of unit mass moving in potential  $-2DV_s$  [12].

For small values of the diffusion coefficient, one expects that the trajectories of the Brownian particle will be very close to the optimal path. An approximate propagator is simply given by

$$P(x, t) \cong K(t) \exp \left\{ - \int_{t_0}^t \mathbb{L}[x_c(\tau)] d\tau \right\}, \quad (\text{II.94})$$

where  $K(t)$  is the normalizing constant chosen to make  $P(x, t)$  satisfy

$$\int_{-\infty}^{\infty} P(x, t) dx = 1. \quad (\text{II.95})$$

This approximation will be useful when  $D \rightarrow 0$  and the largest contribution of the path integral Eq.(II.89) only comes from the optimal path.

## 6. The quadratic approximation

The next approximation to the path integral solution is generally known as the quadratic approximation <sup>1</sup>. Let's consider the propagator given by Eq.(II.89)

$$\begin{aligned} P(x, t) &= \exp \left( \frac{U^*(x_0) - U^*(x)}{2} \right) \\ &\times \int_{x_0, t_0}^{x, t} \exp \left[ - \frac{1}{4D} \int_{t_0}^t \left( \frac{dx}{d\tau} \right)^2 d\tau - \int_{t_0}^t V_s(x(\tau), \tau) d\tau \right] d[x(\tau)]. \end{aligned} \quad (\text{II.96})$$

Write

$$x(\tau) = x_c(\tau) + \delta(\tau), \quad (\text{II.97})$$

where  $x_c(\tau)$  is the optimal path and  $\delta(\tau)$  denotes the deviation from it. Hence at the start and end points of path,  $\delta(t_0) = 0$  and  $\delta(t) = 0$ . Expand the exponential in Eq.(II.96) in powers of  $\delta$ , the zero order term is

$$\exp \left[ - \frac{1}{4D} \int_{t_0}^t \left( \frac{dx_c}{d\tau} \right)^2 d\tau - \int_{t_0}^t V_s(x_c(\tau)) d\tau \right]. \quad (\text{II.98})$$

---

<sup>1</sup>It is also called WKB approximation in Schulman's book [13].

The term of first order in  $\delta$  will vanish because of the definition of the optimal path. The term of second order in  $\delta$  is of the form

$$\exp \left[ \int_{t_0}^t \left( \frac{d\delta}{d\tau} \right)^2 d\tau - \int_{t_0}^t \frac{V_s''(x_c(\tau))}{2} (\delta(\tau))^2 d\tau \right], \quad (\text{II.99})$$

where primes denote differentiation with respect to the argument. By throwing away terms of higher order in  $\delta$ , we arrive at the approximation for the probability

$$P(x, t) \approx \exp \left( \frac{U^*(x_0) - U^*(x)}{2} \right) F(x, t) \\ \times \exp \left[ -\frac{1}{4D} \int_{t_0}^t \left( \frac{dx_c}{d\tau} \right)^2 d\tau - \int_{t_0}^t V_s(x_c) d\tau \right] \quad (\text{II.100})$$

$$F(x, t) = \lim (4\epsilon\pi D)^{-(N+1)/2} \int_{-\infty}^{\infty} d\delta_1 \int_{-\infty}^{\infty} d\delta_2 \cdots \int_{-\infty}^{\infty} d\delta_N \\ \exp \left[ -\frac{1}{4D\epsilon} \sum_{j=0}^N (\delta_{j+1} - \delta_j)^2 - \frac{1}{2} \epsilon \sum_{j=1}^N V_j'' \delta_j^2 \right], \quad (\text{II.101})$$

where  $V_j'' = V_s''(x_c(\tau_j))$  and  $\delta_0 = \delta_{N+1} = 0$ .

To calculate  $F(x, t)$ , we need to use the Gaussian integration formula Eq.(II.72) again. The result is

$$F(x, t) = \lim (4\pi\epsilon D \det B_N)^{-1/2}, \quad (\text{II.102})$$

where  $B$  is the matrix whose elements are

$$B_{k,k} = 2 + 2D\epsilon^2 V_k'' \\ B_{k,k-1} = B_{k,k+1} = -1. \quad (\text{II.103})$$

It is not easy to get the determinant of matrix  $B$  this time. Let's follow Wiegel's work [12]. First, from the calculation of the determinant of the matrix, one can get the recursive relation

$$\det B_N = (2 + 2D\epsilon^2 V_N'') \det B_{N-1} - \det B_{N-2}. \quad (\text{II.104})$$

To change this into a differential equation, let  $\det B_N = (N+1)C_N$ , then Eq.(II.104) becomes

$$C_N - 2C_{N-1} + C_{N-2} = -\frac{2}{N+1} (C_{N-1} - C_{N-2}) + 2\epsilon^2 D \frac{NV_N''}{N+1} C_{N-1}. \quad (\text{II.105})$$

After taking the limit  $\epsilon \rightarrow 0$ ,  $N \rightarrow \infty$  and  $N\epsilon = (t-t_0)$ , Eq.(II.105) changes into a differential equation

$$\frac{d^2C}{dt^2} + \frac{2}{t-t_0} \frac{dC}{dt} = 2DV_s''C, \quad (\text{II.106})$$

with initial conditions at  $t = t_0$ ,  $C = 1$  and  $\frac{dC}{dt} = 0$ . To solve Eq.(II.106), one can let  $H = (t-t_0)C$ . Then the differential equation for  $H$  is of the form

$$\frac{d^2H}{dt^2} = 2DV_s''H, \quad (\text{II.107})$$

at  $t = t_0$ ,  $H = 0$  and  $\frac{dH}{dt} = 1$ . Next one changes the independent variable from  $t$  to  $x_c$  to make this equation easier. Recalling that the optimal path of the Brownian particle is identical to the trajectory of a fictitious Newtonian particle of unit mass moving in potential  $-2DV_s$ , one finds

$$\begin{aligned} \frac{d^2x_c}{dt^2} &= 2D \frac{dV_s}{dx_c} \\ \frac{dx_c}{dt} &= (2E + 4DV_s)^{1/2}, \end{aligned} \quad (\text{II.108})$$

where  $E$  denotes the total mechanical energy of the Newtonian particle. With the change of variables the left side of Eq.(II.107) becomes

$$\begin{aligned} \frac{d^2H}{dt^2} &= \frac{d}{dt} \left( \frac{dH}{dx_c} \frac{dx_c}{dt} \right) \\ &= \left( \frac{d}{dt} \frac{dH}{dx_c} \right) \frac{dx_c}{dt} + \frac{dH}{dx_c} \frac{d^2x_c}{dt^2} \\ &= \frac{d^2H}{dx_c^2} \left( \frac{dx_c}{dt} \right)^2 + \frac{dH}{dx_c} \frac{d^2x_c}{dt^2} \\ &= H''(2E + 4DV_s) + 2H'DV_s'. \end{aligned} \quad (\text{II.109})$$

Now one finds that Eq.(II.107) will become

$$[(2E + 4DV_s)H]'' = (6DHV_s')', \quad (\text{II.110})$$

with initial conditions at  $x_c = x_0$ ,  $H = 0$  and  $\frac{dH}{dx_c} = (2E + 4DV_s)^{1/2}$ .

By integrating both sides of Eq.(II.110) once and applying the initial conditions, one gets

$$(2E + 4DV_s)H' - 2DHV_s' = (2E + 4DV_s(x_0))^{1/2}. \quad (\text{II.111})$$

Divided by  $(2E + 4DV_s)$ , Eq.(II.111) becomes a Bernoulli equation [24]

$$H' + W(x_c)H = Q(x_c), \quad (\text{II.112})$$

where

$$\begin{aligned} W(x_c) &= -\frac{2DV'_s}{2E + 4DV_s} \\ Q(x_c) &= \frac{(2E + 4DV_s(x_0))^{1/2}}{2E + 4DV_s}. \end{aligned} \quad (\text{II.113})$$

Then the solution is

$$\begin{aligned} H(x_c) &= e^{-\int W(x_c)dx_c} \int e^{\int W(x_c)dx_c} Q(x_c)dx_c + ce^{-\int W(x_c)dx_c} \\ &= (2E + 4DV_s)^{1/2}(2E + 4DV_s(x_0))^{1/2} \int_{x_0}^{x_c} (2E + 4DV_s(y))dy + c(2E + 4DV_s)^{1/2} \\ &= (2E + 4DV_s)^{1/2}(2E + 4DV_s(x_0))^{1/2} \int_{x_0}^{x_c} (2E + 4DV_s(y))dy. \end{aligned} \quad (\text{II.114})$$

In the derivation we used  $H = 0$  when  $x_c = x_0$  to find the constant  $c$  equals zero.

Finally one can write explicitly

$$\begin{aligned} F(x, t) &= \lim(4\pi\epsilon D \det B_N)^{-1/2} \\ &= [4\pi D(t - t_0)C(x, t)]^{1/2} \\ &= [4\pi DH(x, t)]^{1/2} \\ &= \left[ 4\pi D(2E + 4DV_s(x_0))^{1/2}(2E + 4DV_s(x))^{1/2} \right. \\ &\quad \left. \times \int_{x_0}^x (2E + 4DV_s(y))dy \right]^{1/2}. \end{aligned} \quad (\text{II.115})$$

Hence under the quadratic approximation, the propagator for a Brownian motion in a field of force is

$$\begin{aligned} P(x, t) &\approx \exp\left(\frac{U^*(x_0) - U^*(x)}{2}\right) \left[ 4\pi D(2E + 4DV_s(x_0))^{1/2} \right. \\ &\quad \left. \times (2E + 4DV_s(x))^{1/2} \int_{x_0}^x (2E + 4DV_s(y))dy \right]^{1/2} \\ &\quad \times \exp\left[-\frac{1}{4D} \int_{t_0}^t \left(\frac{dx_c}{d\tau}\right)^2 d\tau - \int_{t_0}^t V_s(x_c)d\tau\right]. \end{aligned} \quad (\text{II.116})$$

If the probability of path decreases sufficiently rapidly with increasing deviation from the optimal path, i.e.,  $D \rightarrow 0$ , Eq.(II.116) will be a good approximation [12, 25].

## E. EXAMPLES

In this section we will review several Brownian motion problems. The examples will be solved using the techniques and approximations discussed above.

### 1. Reaction rate

Problem: In one-dimensional space, there is an over-damped Brownian particle in the left well of the double-well potential. What is the average time this particle will wait before the noise drives it over the barrier to reach the right well for the first time?

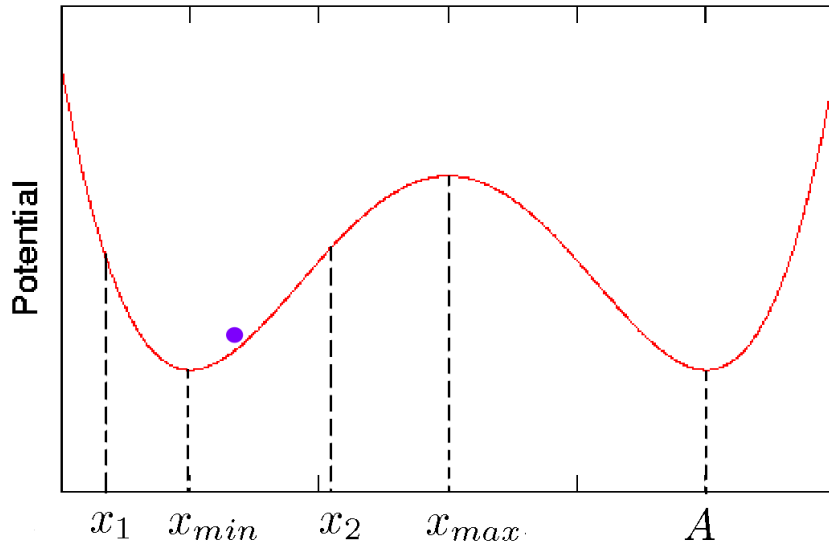


Figure 9: An over-damped Brownian particle in a double-well potential.

Solving for the rate at which a Brownian particle escapes from a potential well is called the *Kramers problem* [2]. The results can be derived by different methods [7, 8, 11]. Here we will follow the method of solution given by Risken [8].

From Sec.II.C.1, the probability that this particle is found at position  $x$  at time  $t$ ,  $P(x, t)$  is given by the Fokker-Planck equation Eq.(II.44). According to Eq.(II.53), the current

satisfies

$$J(x, t) \exp(U^*(x)) = -D \frac{\partial}{\partial x} \exp(U^*(x)) P(x, t). \quad (\text{II.117})$$

Integrating Eq.(II.117) between  $x_{min}$  and  $A$  yields

$$\begin{aligned} \int_{x_{min}}^A J(x, t) \exp(U^*(x)) dx &= -D \int_{x_{min}}^A \frac{\partial}{\partial x} \exp(U^*(x)) P(x, t) dx \\ &= D [\exp(U^*(x_{min})) P(x_{min}, t) - \exp(U^*(A)) P(A, t)] \end{aligned} \quad (\text{II.118})$$

Assuming the barrier is high, at least several  $k_B T$ , then the leak of the probability in the left well to the right will only make negligible probability distribution change everywhere. The whole system is approximately in a stationary state, and both sides of Fokker-Planck equation will be very close to zero,

$$\frac{\partial P(x, t)}{\partial t} = -\frac{\partial J(x, t)}{\partial x} \approx 0. \quad (\text{II.119})$$

Hence the current  $J(x, t)$  is independent of position  $x$ , and from Eq.(II.118) it is given by

$$J(t) = D [\exp(U^*(x_{min})) P(x_{min}, t) - \exp(U^*(A)) P(A, t)] / \int_{x_{min}}^A \exp(U^*(x)) dx. \quad (\text{II.120})$$

Because of the high barrier, the probability at position  $A$  will be negligible for a long time, so we can put  $P(A, t) = 0$  in Eq.(II.120), which becomes

$$J(t) = D \exp(U^*(x_{min})) P(x_{min}, t) / \int_{x_{min}}^A \exp(U^*(x)) dx. \quad (\text{II.121})$$

Because the system is close to a stationary state, in the left well we have

$$P(x, t) = P(x_{min}, t) \frac{\exp(-U^*(x))}{\exp(-U^*(x_{min}))}, \quad (\text{II.122})$$

and the total probability in the left well is

$$\begin{aligned} \mathbb{P}(t) &\approx \int_{x_1}^{x_2} P(x, t) dx \\ &= \int_{x_1}^{x_2} P(x_{min}, t) \exp(U^*(x_{min}) - U^*(x)) dx \\ &= P(x_{min}, t) \exp(U^*(x_{min})) \int_{x_1}^{x_2} \exp(-U^*(x)) dx, \end{aligned} \quad (\text{II.123})$$

where  $x_1$  and  $x_2$  don't need to be specified, but  $(U^*(x_1) - U^*(x_{min}))$  and  $(U^*(x_2) - U^*(x_{min}))$  are large enough so the probability outside of these two ends can be neglected. From Eq.(II.121) and (II.123) the average waiting time is

$$\begin{aligned}\tau = \frac{1}{\gamma} &\equiv \frac{\mathbb{P}(t)}{J(t)} \\ &= \frac{1}{D} \int_{x_1}^{x_2} \exp(-U^*(x)) dx \int_{x_{min}}^A \exp(U^*(x)) dx, \end{aligned} \quad (\text{II.124})$$

where  $\gamma$  is the escape rate. Because the barrier height is large, the main contribution to the first integral in Eq.(II.124) comes from the region around  $x_{min}$ , and the main contribution to the second integral comes from the region around  $x_{max}$ . We can use the steepest descent approximation to evaluate them,

$$\begin{aligned}\tau &= \frac{1}{D} \int_{x_1}^{x_2} \exp(-U^*(x)) dx \int_{x_{min}}^A \exp(U^*(x)) dx \\ &= \frac{1}{D} \left\{ -\exp(U^*(x_{min})) \int_{-\infty}^{\infty} \exp \left[ -\frac{1}{2} U^{*''}(x_{min})(x - x_{min})^2 \right] dx \right\} \\ &\times \left\{ \exp(U^*(x_{max})) \int_{-\infty}^{\infty} \exp \left[ \frac{1}{2} U^{*''}(x_{max})(x - x_{max})^2 \right] dx \right\} \\ &= \frac{2\pi}{D \sqrt{-U^{*''}(x_{min})U^{*''}(x_{max})}} \exp(U^*(x_{max}) - U^*(x_{min})). \end{aligned} \quad (\text{II.125})$$

The escape rate is then

$$\gamma = \frac{\sqrt{-U^{*''}(x_{min})U^{*''}(x_{max})}}{2\pi} \exp[-(U^*(x_{max}) - U^*(x_{min}))]. \quad (\text{II.126})$$

In fact, the meaning of Eq.(II.126) is very important. As we mentioned in Sec.II.A.2, a chemical or biological, macroscopic system in the lab can often be treated as a Brownian particle moving along some reaction coordinate. If we use the double well as a simplest model for a chemical or biological reaction, the escape rate  $\gamma$  gives its reaction rate. This rate  $\gamma$  is determined by the barrier height and the curvatures at  $x_{min}$  and  $x_{max}$ ; the waiting time will increase exponentially as the barrier height increases. Readers can find more discussion about this important topic in the article of Borkovec and Hänggi [2].

The waiting time follows an exponential distribution [26]. Eq.(II.124) and the definition of current  $J(t)$  gives rise to an differential equation of  $\mathbb{P}(t)$

$$J(t) = \mathbb{P}(t)\gamma = -\frac{d\mathbb{P}}{dt}, \quad (\text{II.127})$$

whose solution is

$$\mathbb{P}(t) = \exp(-\gamma t), \quad (\text{II.128})$$

with the initial condition  $\mathbb{P}(0) = 1$ . The distribution of waiting time  $f(t)$  is given by

$$f(t) = J(t) = -\frac{d\mathbb{P}}{dt} = \gamma \exp(-\gamma t), \quad (\text{II.129})$$

which is an exponential distribution.

## 2. Splitting probability

Problem: Sparta was a militarist state, and all individuals would be trained strictly to be warriors. Let's make a simple model for the training. Suppose there is one quantity, fighting power  $x$ , which measures how good a warrior is (like in computer or D&D games [27]). The training begins from their childhood, every child has the same initial fighting power  $x_0$ . During the training, a Spartan grows up and becomes stronger and stronger, so  $x$  will increase linearly with a slope  $Dk$ . But the effect of training is unpredictable, because one can become more skillful or be hurt badly, which is given by a Gaussian noise  $R(t)$  with zero mean and satisfying  $\langle R(t)R(t') \rangle = 2D\delta(t - t')$ . If one's fighting power reaches  $x_f$ , the individual will be treated as a grown-up warrior. But one will die or be banished if fighting power is zero. Under this model, what fraction of Spartans will succeed the in military training?

In Gardiner's book [7], this fraction is called the probability of exit through a particular end of an interval. The picture in physics is, a Brownian particle starts from the initial position  $x_0$  and walks in an interval  $(a, b)$  which has absorbing walls at two ends. What is the probability that it will be absorbed at  $a$  or  $b$ ?

The probability of being absorbed by  $a$  is the integrated current at  $a$

$$\begin{aligned}\Pi_a(x_0) &= -\int_0^\infty J(a, s|x_0, 0)ds \\ &= D\int_0^\infty \left[ U^{*\prime}(a)P(a, s|x_0, 0) + \frac{\partial P(x, s|x_0, 0)}{\partial x} \Big|_{x=a} \right] ds.\end{aligned}\quad (\text{II.130})$$

One can solve the Fokker-Planck equation under this special boundary condition and calculate the probability  $\Pi_a$  using Eq.(II.130). However, in general it will be very difficult for arbitrary potential  $U^*$ . Here we follow Gardiner's book [7] to find the solution. First one can prove the  $P(x, s|x_0, 0)$  will also satisfy the so-called ‘‘backward Fokker-Planck equation’’

$$\frac{\partial P(x, s|x_0, 0)}{\partial s} = -D\left(\frac{dU^*}{dx}\right)\frac{\partial P(x, s|x_0, 0)}{\partial x_0} + D\frac{\partial^2 P(x, s|x_0, 0)}{\partial x_0^2}.\quad (\text{II.131})$$

Note the derivatives are with respect to the initial value of  $x$ . The proof will not be given here; readers who are interested can find the details in Gardiner's or Risken's books [7, 8]. The backward Fokker-Planck equation carries the same information as the regular Fokker-Planck equation; the difference is which set of variables are fixed.

Now we want to build up a differential equation for  $\Pi_a(x_0)$ . Inspired by Eq.(II.131), one can find

$$\begin{aligned}& -D\left(\frac{dU^*}{dx}\right)\frac{d\Pi_a(x_0)}{dx_0} + D\frac{d^2\Pi_a(x_0)}{dx_0^2} \\ &= D\int_0^\infty \left[ U^{*\prime}(a)\frac{\partial P(a, s|x_0, 0)}{\partial s} + \frac{\partial}{\partial x}\frac{\partial P(x, s|x_0, 0)}{\partial s} \Big|_{x=a} \right] ds \\ &= \int_0^\infty \frac{\partial J(a, s|x_0, 0)}{\partial s} ds \\ &= J(a, \infty|x_0, 0) - J(a, 0|x_0, 0).\end{aligned}\quad (\text{II.132})$$

Since the current at  $a$  when  $s = 0$  or  $s = \infty$  is zero, Eq.(II.132) will become

$$-\left(\frac{dU^*}{dx}\right)\frac{d\Pi_a(x_0)}{dx_0} + \frac{d^2\Pi_a(x_0)}{dx_0^2} = 0.\quad (\text{II.133})$$

For the absorbing boundary conditions, if a particle starts from  $a$  or  $b$ , it will be absorbed immediately, which means  $\Pi_a(a) = 1$  and  $\Pi_a(b) = 0$ . Then it is easy to get the solution of  $\Pi_a(x_0)$  and  $\Pi_b(x_0)$

$$\begin{aligned}\Pi_a(x_0) &= \frac{\int_{x_0}^b \exp(U^*(x))dx}{\int_a^b \exp(U^*(x))dx} \\ \Pi_b(x_0) &= 1 - \Pi_a(x_0) = \frac{\int_a^{x_0} \exp(U^*(x))dx}{\int_a^b \exp(U^*(x))dx}.\end{aligned}\tag{II.134}$$

$\Pi_a$  and  $\Pi_b$  are the “splitting probabilities”.

Returning to our problem of the Spartan training, the potential is  $U^* = -kx$ ,  $a = 0$  and  $b = x_f$ ; then the probability of success is

$$\Pi_{x_f}(x_0) = \frac{1 - \exp(-kx_0)}{1 - \exp(-kx_f)}.\tag{II.135}$$

### III. SIMULATION METHODS

#### A. IMPORTANCE OF SIMULATION

In this chapter, we will discuss a variety of simulation methods for rare events, which is another important part of my research described in this thesis. The first topic I want to discuss here is why simulations are important [1, 28–30].

From my review, the first reason is the limit of our analytical tools. We may be able to do the analysis of some linear problems, but many natural phenomena are nonlinear. Even for the simple laws of Newtonian mechanics, when the system we want to study has multiple degrees of freedom - for example, the motion of more than two interacting bodies - it is very difficult to obtain an analytical solution. A protein built up from hundreds of amino acid in solvent is completely out of reach. But simulation can provide numerical results for these problems, and it is a potential tool to help understand natural phenomena.

Because of the ability to obtain the numerical results, simulations are a bridge between laboratory experiments and theory. After a theoretical model is given, it will generally be checked against experiments. Sometimes physicists are lucky because their model can be solved analytically, but this does not occur very often. When the model is too complex, approximate methods are often applied. If the theoretical results don't agree with the experimental data, it may mean the model is wrong, or we have used an inadequate approximation. Now simulations help us to get numerical results (with 'generally' statistical errors) from a given model system without using approximate methods, so that the theoretical model and experiments can be compared directly.

Another important role that simulation plays is the possible replacement of some experiments. First, it will save a lot of money by replacing experiments under extreme conditions

with simulations. The case of a computer will not explode when it simulates a high pressure container, and the CPU will not smoke when the simulation temperature is  $6000^{\circ}\text{C}$ . Second, simulation can get information which is very hard to obtain by available experimental techniques. For example, in the study of the transition path for the conformational change of a particular protein, experiments at this point seem powerless. The most effective techniques for structure determination, like X-ray and NMR, are more compliant for stable states. They may be able to give the two ends of the transition, but it is difficult to find intermediate states by using these techniques, and more difficult still to get a continuous pathway, which is much easier for simulations.

Then there is an important issue to consider: How good are the results given by simulation? Can we really reproduce what happens in a laboratory experiment on a computer today? I have doubts about it myself. But considering that computer simulation only began in the early 1950s, I have no doubts that it will be better in the future. To make the simulations more realistic is always an essential topic. Proper (simplified or idealized) description for a system or process is the job of molecular modelling [28]. But it is not what I concentrate on in my research, so the discussion will stop here. More discussion and background will be found in these books [1, 28–30].

## B. BRUTE FORCE SIMULATION

To simulate rare events, the most straightforward way is running a long simulation and collecting the rare events which happen to occur.

For example, to study rare events in one-dimensional over-damped Brownian motion, one can just run a brute force simulation by using the over-damped Langevin equation (II.20). Standard simulations of the over-damped Langevin Eq.(II.20) employ a simple first-order scheme with fixed time step  $\Delta t$ , such that

$$x_j = x(j\Delta t), \quad j = 0, 1, 2, \dots \quad (\text{III.1})$$

and [31]

$$x_{j+1} = x_j + \frac{F(x_j)}{\gamma} \Delta t + \Delta x_R. \quad (\text{III.2})$$

Consistent with Eq.(II.22) the thermal fluctuation (noise increment)  $\Delta x_R$  is chosen from a Gaussian distribution of zero mean and variance

$$\sigma^2 = 2 \left( \frac{k_B T}{\gamma} \right) \Delta t = 2D\Delta t. \quad (\text{III.3})$$

However, this direct approach proves inadequate to simulate rare events, even in one dimension. Such a program running on a single CPU can provide an ensemble of transition trajectories (with hundreds or thousands of transition-events) only for low barrier height (less than  $10 k_B T$ ). For high barriers, the waiting time between successful events will become unacceptably long, which has been discussed in Sec. II.E.1.

### C. PATH SAMPLING APPROACHES

Traditional molecular simulations are limited to less than 100 nsec [32], making them inadequate to the task of studying rare events, such as the large conformational transitions in macromolecules, which may occur on  $\mu\text{sec}$  - msec timescales or beyond [33]. Yet the situation is actually worse than it first appears: even if such long simulations could be achieved, the observation of a *single* transition-event would hardly be a full scientific description of the process. Because structural transitions are driven by thermal fluctuations, some degree of variability among events must be expected — in turn requiring the observation of many events to draw statistically satisfactory conclusions. Such a statistical outlook has most famously been exploited in studies of protein folding paths (e.g., Ref. [34–37]).

Three basic approaches to the problem of long-time macromolecular dynamics have been explored by a number of investigators. Coarse-graining is probably the oldest strategy, dating from the very earliest molecular simulations [38, 39]. By reducing the number of degrees of freedom, coarse-grained models of proteins can drastically reduce the intrinsic cost of simulating a time step, as well as increasing the duration of each step. The strategy has been pursued for many different problems over the years from protein folding to aggregation

to conformational change [40–53]. Although coarse-grained models fail to capture atomistic detail and may have limited biochemical accuracy, recent work may permit the use of simplified ensembles in accelerating atomistic sampling [54, 55].

A second approach pursues a severe discretization of conformation-state space which enables the use of master-equation stochastic kinetics [56–58]. Although an exact kinetic description can be obtained, a comprehensive and accurate discretization of configuration space is required. In other words, all states must be known with equilibrium probabilities and transition rates. Thus, at present, such a description is limited to cases where rather complete sampling can be obtained by some other means.

The third strategy, path sampling, is of greatest relevance to my research. Path sampling approaches [59–71] can, in principle, be applied to models of any level of detail, without approximation to the correct statistical mechanics. The potential for efficiency in these approaches stems from an extreme separation of timescales: *rare events are rare because they are infrequent, not because the events are slow*. As shown in Fig. 1, the duration of an event itself typically is orders of magnitude less than the associated waiting time between events [59, 72]. Path-sampling approaches make practical use of this separation by focusing computer resources exclusively on rare transition events — as opposed to random equilibrium motions which prove unproductive of transitions. Path sampling approaches, it should be noted, have recently been applied to atomistic models of proteins and nucleic acids [65, 66, 71].

## 1. Transition path sampling

To generate a sufficient quantity of transition-events, perhaps the best known method is a Monte Carlo path-sampling approach, transition path sampling (TPS). The approach has its roots in path integral Monte Carlo for quantum systems [73, 74], but Pratt provided an important advance in recognizing the analogous application in classical and, particularly, chemical systems [59].

Pratt’s approach has recently been taken up with some vigor by Chandler and co-workers [75, 76]. Related work was presented by Zimmer and Paniconi [77, 78].

The basic strategy behind path-sampling is simple: focus computer time on the rare transition-events of interest, rather than on the waiting time between events, which can be longer by many orders of magnitude. The transition path sampling methods primarily follows Pratt’s approach, which is based on two facts: (i) Path (i.e., trajectory) probabilities are readily computed for stochastic processes, so that trajectories themselves may be viewed as  $N \times d$  dimensional equilibrium “objects”, when there are  $N$  time steps and  $d$  spatial dimensions. (ii) Wherever equilibrium probabilities can be computed for all such “objects” in an abstract space, Metropolis sampling can be performed.

As in any Metropolis simulation, we require that detailed balance is satisfied. That is, for arbitrary paths  $\zeta_i$  and  $\zeta_j$  with equilibrium probabilities  $P(\zeta)$  and overall transition rates  $\Gamma$ , we require

$$P(\zeta_i)\Gamma(\zeta_i \rightarrow \zeta_j) = P(\zeta_j)\Gamma(\zeta_j \rightarrow \zeta_i). \quad (\text{III.4})$$

The rate  $\Gamma$  is decomposed into the usual product of the generating ( $D$ ) and acceptance ( $acc$ ) components [1, 76], which are proportional to the conditional probability for generating and accepting the trial path  $j$ , starting from  $i$ . Then trial moves should be accepted with probability  $\min[1, R]$ , where

$$R = \frac{acc(\zeta_i \rightarrow \zeta_j)}{acc(\zeta_j \rightarrow \zeta_i)} = \frac{P(\zeta_j) \times D(\zeta_j \rightarrow \zeta_i)}{P(\zeta_i) \times D(\zeta_i \rightarrow \zeta_j)}. \quad (\text{III.5})$$

All paths in the ensemble will have the same total number of steps  $N$ , so that the probability of two paths can be compared.

To proceed we need to discuss how to generate new paths. If we just make a small change to the start position of the old path, and run the simulation, the probability that the new path ends in the final state will be small [1]. Then the Monte Carlo acceptance will be very low. Dellago, Bolhuis and Chandler suggested a better approach called a “shooting algorithm” [76]. As shown in Fig. 10, instead of the initial point, they randomly choose one point in the middle of the “old” path and run the simulation. Because the state in the middle of a path usually, under the conditions of the simulation, is unstable, the system will most likely relax to the initial or final state. Gluing the new relaxation part and the part in the old path heading the opposite direction gives a new path. However, one can also relax the system from the middle state several times so that one can get successful parts connecting

both sides. Then the new path has only one common point with the old one. This is the approach that has been used and that is illustrated below.

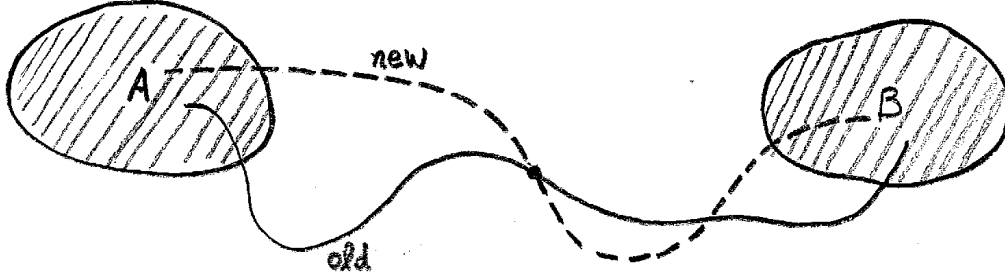


Figure 10: Shooting algorithm to generate new path [76].

Let's consider the transition path sampling method for over-damped Brownian motion in one-dimensional space with arbitrary potential  $U^*(x)$  as an example. For a path  $\zeta = \zeta(\{x_0, x_1, \dots, x_N\})$ , the probability is

$$P(\zeta) \propto \exp[-U^*(x_0)] \times [\prod_{i=0}^{N-1} p(x_i, x_{i+1}; U^*)], \quad (\text{III.6})$$

where the single-step transition probability corresponding to Eqs.(III.2) and (III.3) is a Gaussian density, namely

$$p(x_i, x_{i+1}; U^*) = \frac{1}{\sqrt{2\pi}\sigma} \exp \left\{ -\frac{\left[ x_{i+1} - x_i - \frac{1}{2} \left( -\frac{dU^*}{dx} \right) (2D\Delta t) \right]^2}{2\sigma^2} \right\}. \quad (\text{III.7})$$

where  $\frac{dU^*}{dx_i} \equiv \frac{dU^*(x)}{dx} \Big|_{x_i}$ .

Then let's suppose that we already have one "old" path  $\zeta_o = \zeta(\{y_0, y_1, \dots, y_N\})$ , which connects the initial and final states, and which has  $M_o$  steps in the transition region, where  $M_o < N$ . By using the shooting algorithm described above we find a "new" path  $\zeta_n = \zeta(\{x_0, x_1, \dots, x_N\})$ , which connects the initial and final states by  $M_n$  steps, where  $M_n < N$ . These two paths share one point  $y_{m(o)} = x_{m(n)}$ . Then the generating probability from path  $\zeta_o$  to  $\zeta_n$  is

$$D(\zeta_o \rightarrow \zeta_n) \propto \frac{1}{M_o} [\prod_{i=0}^{m(n)-1} p'(x_i, x_{i+1}; U^*)] [\prod_{i=m(n)}^{N-1} p(x_i, x_{i+1}; U^*)]. \quad (\text{III.8})$$

On the right side of Eq.(III.8), the factor  $\frac{1}{M_o}$  raises because we randomly choose one point from part of the old path  $\{y_0, y_1, \dots, y_{M_o}\}$  to start the shooting algorithm. The single-step transition probability  $p(x_i, x_{i+1}; U^*)$  for steps from  $x_{m(n)}$  to  $x_N$  is the same as Eq.(III.7). For the steps from  $x_0$  to  $x_{m(n)}$ , because this part is generated by shooting backward to the initial state, the single-step transition probability is

$$p'(x_i, x_{i+1}; U^*) = \frac{1}{\sqrt{2\pi}\sigma} \exp \left\{ -\frac{\left[ x_i - x_{i+1} - \frac{1}{2} \left( -\frac{dU^*}{dx_{i+1}} \right) (2D\Delta t) \right]^2}{2\sigma^2} \right\}. \quad (\text{III.9})$$

where  $\frac{dU^*}{dx_{i+1}} \equiv \frac{dU^*(x)}{dx} \Big|_{x_{i+1}}$ . Similarly the generating probability from path  $\zeta_n$  to  $\zeta_o$  is

$$D(\zeta_n \rightarrow \zeta_o) \propto \frac{1}{M_n} [\prod_{i=0}^{m(o)-1} p'(y_i, y_{i+1}; U^*)] [\prod_{i=m(o)}^{N-1} p(y_i, y_{i+1}; U^*)]. \quad (\text{III.10})$$

Finally this trial move will be accepted with probability  $\min[1, R]$ , where

$$R = \frac{M_o \exp[-U^*(x_0)] \times [\prod_{i=0}^{m(n)-1} p(x_i, x_{i+1}; U^*)] \times [\prod_{i=0}^{m(o)-1} p'(y_i, y_{i+1}; U^*)]}{M_n \exp[-U^*(y_0)] \times [\prod_{i=0}^{m(o)-1} p(y_i, y_{i+1}; U^*)] \times [\prod_{i=0}^{m(n)-1} p(x_i, x_{i+1}; U^*)]}. \quad (\text{III.11})$$

For different problems, different generating methods can be applied to gain better efficiency for Monte Carlo simulation. For example, we use a new generating method in the studying of the duration of transition-events in one-dimensional space, which will be discussed in Sec.IV.B.

The transition path sampling method is one well accepted path sampling approach and has been coded into popular simulation software, like CHARMM [79].

What are the strengths and weaknesses of transition path sampling? It generates the correct path ensemble, and it can be very fast in some cases. To apply transition path sampling, one needs an initial path, which may be difficult to obtain. And it is also difficult to code a path sampling method based on brute force simulation programs. A more serious problem is that as a Monte Carlo simulation in the path space, it is possible to be trapped in a local minimum, and miss other channels. We will come back to check this carefully in a later chapter.

## 2. Weighted ensemble method

The second advanced path sampling method discussed here is called Weighted Ensemble (WE) method, which was first introduced by Huber and Kim [63]. It has been applied to study diffusion effects in binding [63, 80–82] and the folding of a simple model protein [83]. A similar idea has been used by Huber and McCammon to find the global minimum of complicated functions [84]. We have shown it is a very promising simulation approach to investigate conformational transitions [85].

### a. Method

As we mentioned before, one can run multiple brute-force simulations simultaneously, as a statistical ensemble, to get an approximate solution of the Fokker-Planck equation. Of course running all these brute-force simulations simultaneously doesn't save any computer time. The weighted ensemble approach also runs multiple brute-force simulations simultaneously. However, by assigning a different weight for every simulation, and distributing computing resources toward the evolving tail of the probability distribution (in the direction of the target), it turns out to be much more efficient to sample rare events than the regular brute-force simulation.

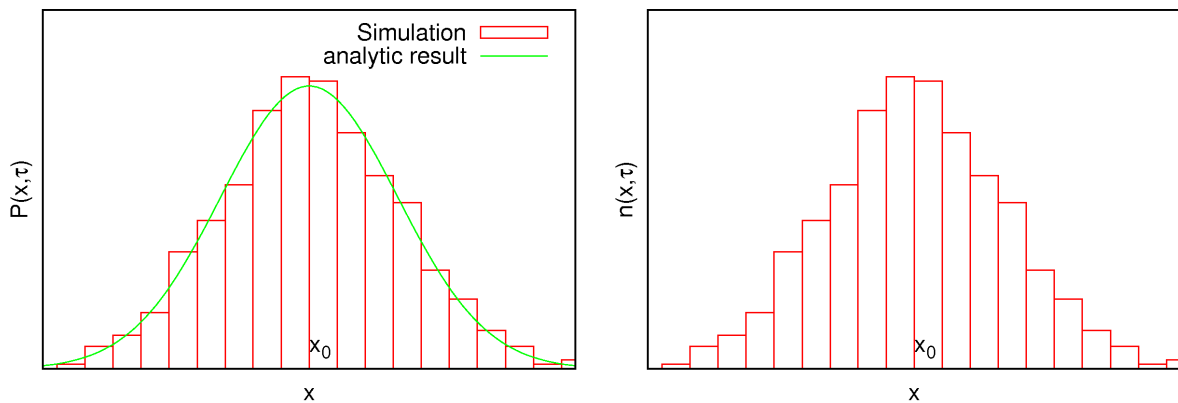


Figure 11: Probability distribution and histogram of simulations for a regular brute-force simulation.

Let's use a simple example to explain the weighted ensemble method. Suppose one wants

to get the solution to the Fokker-Planck equation for free diffusion with initial condition

$$\begin{aligned}\frac{\partial P(x, t)}{\partial t} &= D \frac{\partial^2 P(x, t)}{\partial x^2} \\ P(x, t_0) &= \delta(x - x_0).\end{aligned}\tag{III.12}$$

Assume one runs  $N$  standard brute-force Langevin equation simulations for time  $\tau$  simultaneously. Let  $n(x, \tau)dx$  represent the number of Brownian particles found in the interval  $x$  and  $x + dx$  at time  $\tau$ , satisfying

$$\int_{-\infty}^{\infty} n(x, \tau)dx = N.\tag{III.13}$$

Then the approximate solution for  $P(x, \tau)$  in Eq.(III.12) at time  $\tau$  is given by

$$P(x, \tau) \approx \frac{n(x, \tau)}{N}.\tag{III.14}$$

Notice  $n(x, \tau)$  and  $P(x, \tau)$  will have the same shape in Fig. 11, and that in this simulation every Brownian particle has the same weight.

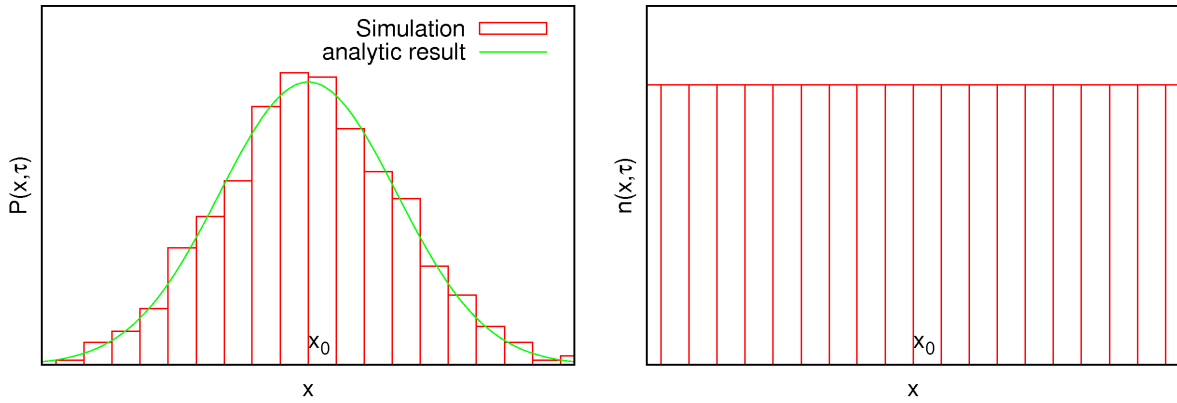


Figure 12: Schematic probability and histogram of simulations for a weighted ensemble simulation.

In the weighted ensemble approach, separate weights are assigned to all the independent simulations. By properly accounting for trajectory weights, the weighted ensemble approach obeys the Fokker-Planck equation, even when trajectories are distributed uniformly in space.

As shown schematically in Fig. 12, after running  $N$  brute-force simulations for time  $\tau$  using the weighted ensemble approach, the distribution of  $P(x, \tau)$  will be the same Gaussian function, but  $n(x, \tau)$  is kept as a constant in the whole space. This is because the Brownian particles around  $x = x_0$  carry larger weights than those far away from the middle.

To keep simulations approximately uniformly distributed everywhere, the basic idea is to observe unbiased trajectories along a “progress coordinate” divided into bins - to replicate (split) those trajectories which move to empty bins. The progress coordinate is so named because it *need not correspond to a reaction coordinate*, which is a strength of the Weighted Ensemble method. (In an important development we have found that pre-defined progress coordinate is unnecessary, see Chapter VII.)

The following steps are used in the Weighted Ensemble method:

- I. Divide phase space into  $N$  bins or regions according to an arbitrarily chosen progress coordinate. Each bin will be allowed to contain no more than  $M$  trajectories at any time.
  - II. Initially,  $M$  independent trajectories are started from the same configuration. Each carries a weight  $1/M$ .
  - III. Run all the independent simulations for a fixed time  $\tau$ .
  - IV. Check each bin to see if it has become populated.
    - A. If there are fewer than  $M$  trajectories in the bin, split the trajectory (or trajectories) in the bin so that there are  $M$  total. Usually one takes the trajectory in the bin carrying biggest probability (weight)  $p_{max}$ , and copies an identical simulation from it. The weights assigned to the original and this new trajectory become  $p_{max}/2$ .
    - B. If a bin contains more than  $M$  trajectories, combine the lowest-weight simulations. One can take the two trajectories carrying smallest probabilities  $p_{min1}$  and  $p_{min2}$ , remove one of them and let the surviving one have the total weight  $(p_{min1} + p_{min2})$ . To perform this “combination” without introducing statistical bias, the “survival” probabilities of these two trajectories are taken to be  $p_{min1}/(p_{min1} + p_{min2})$  and  $p_{min2}/(p_{min1} + p_{min2})$ . See Ref. [63] for details and explanation.
- This procedure is repeated until there are  $M$  trajectories in the bin.
- V. Go back to step III.

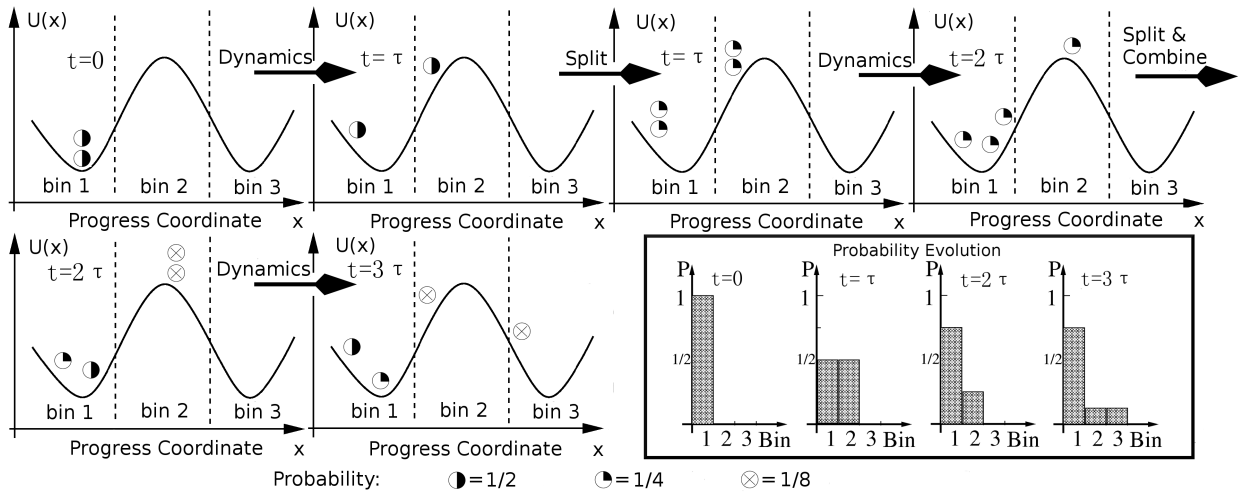


Figure 13: Schematic illustration of the Weighted Ensemble (WE) method, using  $N = 3$  bins and  $M = 2$  simulations per bin following Ref. [80]. After initiating  $M$  trajectories, unbiased dynamics are simulated for a time  $\tau$ , after which the locations (bins) are checked. Trajectories are split or combined to maintain  $M$  trajectories per bin, while preserving the correct probabilities in each bin. Dynamics are again initiated and the process repeated. The lower right box shows the corresponding evolution of the probability histogram.

In Fig. 13 we show a schematic example of the Weighted Ensemble method for a double-well potential in one dimension. The progress coordinate ( $x$  in this case) is divided into  $N = 3$  bins, and each bin will allow  $M = 2$  simulations. After  $3\tau$ , one trajectory carrying probability  $P = 1/8$  has arrived at the third bin.

### b. Estimating the rate in weighted ensemble simulation from short trajectories

The Weighted Ensemble method embodies a strategy of replicating success (“enrichment”), which has been introduced early in the construction of polymer configurations [86]; see also [87]. This strategy makes it possible to sample rare events faster. According to the discussion in Sec. II.E.1, the waiting time of the rare events satisfies the exponential distribution

$$P(t_w) = \gamma \exp(-\gamma t_w), \quad (\text{III.15})$$

where  $\gamma$  is the escape rate, as shown schematically in Fig. 14. Then for the brute-force simulations, the average waiting time for every rare event  $\langle t_w \rangle$  equals  $1/\gamma$ . But in the weighted ensemble approach, the maximum time for one trajectory,  $n\tau$ , can be much smaller than  $\langle t_w \rangle$ , but the method still can produce a “good” rare events ensemble. This means that by replicating success and splitting weights, the weighted ensemble has the ability to sample the rare events with short waiting time, which is shown in Fig. 14 by the shadow area. It should be noticed that, first, the rare events ensemble is not biased because every trajectory segment follows the prescribed dynamics (with or without history dependence). Second, in this short timescale, the value of  $\langle t_w \rangle$  can be obtained. According to Eq.(II.129), when time  $t = n\tau$  is much shorter than  $\langle t_w \rangle$ , the current cross the barrier will be constant because

$$J(t) = \gamma \exp(-\gamma t) = \gamma \exp\left(-\frac{t}{\langle t_w \rangle}\right) \approx \gamma = \frac{1}{\langle t_w \rangle}. \quad (\text{III.16})$$

The probability  $J(t)\tau$  at time  $t$  is the sum of the probabilities of trajectories arriving in the final state between  $(t - \tau)$  and  $t$ , which can be obtained in the weighted ensemble simulation. Then  $\langle t_w \rangle$  can be estimated.

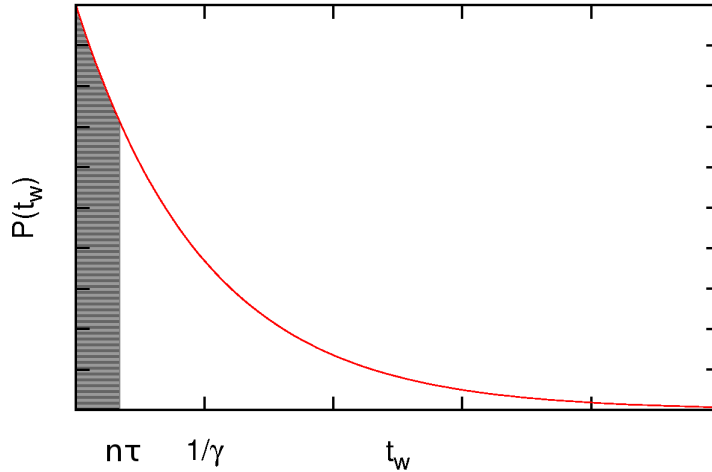


Figure 14: The waiting time of the rare events satisfies the exponential distribution.

### c. Strength of the weighted ensemble method

In this thesis, the weighted ensemble method is chosen to investigate conformational transitions for several reasons. First, among path sampling algorithms, it is particularly elegant and straightforward to implement. Second, the weighted ensemble method appears to be particularly well-suited for sampling multiple, structurally distinct pathways in a statistically correct way. Third, it yields both a path ensemble and the reaction rate from a single simulation. Finally, multiple paths can be found without the need for a pre-specified progress coordinate. Some of these issues will receive additional discussion in Sec.V.D.

## 3. Dynamic importance sampling

Building on work by Ottinger, [62] an independent path-sampling approach, dynamic importance sampling (DIMS) was developed by Zuckerman and Woolf [31, 88]. The dynamic importance sampling method is based on the idea of importance sampling, as the name suggests. One generates a biased path ensemble by using any available knowledge about it, then one reweights the ensemble to get the correct statistical result. It avoids the waiting time for rare events, but depends on the quality of the path-generating method.

### a. Reweighting paths

First, let's review importance sampling. One wants to estimate an average property  $\langle f \rangle$  of a path ensemble, consisting of successful transition paths,

$$\langle f \rangle = \int f(\zeta)P(\zeta)d\zeta, \quad (\text{III.17})$$

where  $\zeta = \zeta(\{\vec{x}_0, \vec{x}_1, \dots, \vec{x}_N\})$  denotes a successful path and  $P(\zeta)$  is its probability. As we mentioned before, one can in principle run a long brute-force simulation to get the answer. In fact, a brute-force simulation samples the paths correctly according their probabilities  $P$ , which means the chance of a path  $\zeta$  appearing during the simulation is proportional to its  $P(\zeta)$ . Then from Eq.(III.17), after one gets  $n$  paths  $\{\zeta_1, \zeta_2, \dots, \zeta_n\}$  from a brute-force simulation, the estimate of  $\langle f \rangle$  is simply

$$\langle f \rangle = \frac{\sum_{i=1}^n f(\zeta_i)}{n}. \quad (\text{III.18})$$

Brute force simulation works, but the average time for generating a successful path and ultimately an ensemble is too long.

Suppose one can generate a path ensemble really quickly, but the chance of a path  $\zeta$  appearing in this ensemble is not proportional to  $P(\zeta)$ , but to  $D(\zeta)$ . Can one still get the correct estimate of  $\langle f \rangle$ ? We will understand how to do it by changing Eq.(III.17) into

$$\langle f \rangle = \int f(\zeta)P(\zeta)d\zeta = \int f(\zeta) \left( \frac{P(\zeta)}{D(\zeta)} \right) D(\zeta)d\zeta. \quad (\text{III.19})$$

Eq.(III.19) tells us that one will still get the right result if one assigns a weight  $w(\zeta) = P(\zeta)/D(\zeta)$  to every path generated. Now  $\langle f \rangle$  is calculated by using

$$\langle f \rangle = \frac{\sum_{i=1}^n w_i f(\zeta_i)}{\sum_{i=1}^n w_i}. \quad (\text{III.20})$$

### b. An example of the dynamic importance sampling

Following Zuckerman and Woolf [31], we discuss applying the method to study a two-dimensional Brownian motion, as shown in Fig. 15. To get a path  $\zeta$  from state A to state B, one can do a simulation by using a Langevin-like discrete equation

$$\vec{x}_{j+1} = \vec{x}_j + \Delta\vec{x}_j^b + \Delta\vec{x}_R, \quad (\text{III.21})$$

where the two components of the white noise  $\Delta\vec{x}_R$  are chosen from a Gaussian distribution of zero mean and variance

$$\sigma^2 = 2 \left( \frac{k_B T}{\gamma} \right) \Delta t = 2D\Delta t. \quad (\text{III.22})$$

In contrast to a brute force simulation Eq.(III.2), we will use some bias force instead of the real force to drive our particle to state B, which causes displacement  $\Delta\vec{x}_j^b$  in Eq.(III.21). There are many ways to define a bias force; here we just use the one in Zuckerman and Woolf's paper [31]. Their choice of the bias displacement for the step  $j$  is

$$\Delta\vec{x}_j^b = \frac{\vec{x}_f - \vec{x}_j}{N - j}, \quad (\text{III.23})$$

where  $\vec{x}_f$  is one target point we choose in state B, and  $N$  is the intended total number of steps of each trajectory. Then the dynamic importance sampling method will sample the paths shorter than  $N$  steps. Other choices, independent of  $N$ , are possible.

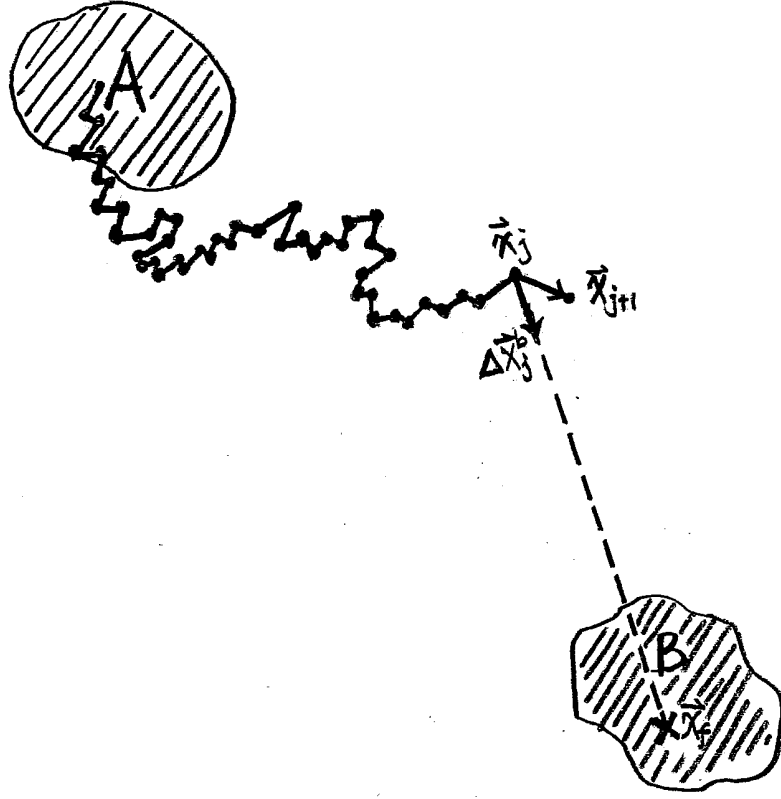


Figure 15: Generate new path with a bias force in dynamic importance sampling method [31].

Generalizing from the one-dimensional problem, the probability for one successful path is

$$P(\zeta) \propto \exp[-U^*(\vec{x}_0)] \times [\prod_{i=0}^{N-1} p(\vec{x}_i, \vec{x}_{i+1}; U^*)]. \quad (\text{III.24})$$

The single-step transition probability in two dimensions is the product of two one-dimensional Gaussian densities, namely

$$p(\vec{x}_i, \vec{x}_{i+1}; U^*) = \frac{1}{\sqrt{2\pi\sigma}} \exp \left\{ -\frac{\left[ x_{i+1} - x_i - \frac{1}{2} \left( -\frac{dU^*}{dx_i} \right) (2D\Delta t) \right]^2}{2\sigma^2} \right\} \\ \times \frac{1}{\sqrt{2\pi\sigma}} \exp \left\{ -\frac{\left[ y_{i+1} - y_i - \frac{1}{2} \left( -\frac{dU^*}{dy_i} \right) (2D\Delta t) \right]^2}{2\sigma^2} \right\}, \quad (\text{III.25})$$

where  $x$  and  $y$  are two components of vector  $\vec{x}$  and  $\frac{dU^*}{dx_i} \equiv \frac{dU^*(x,y)}{dx} \Big|_{x_i,y_i}$ ,  $\frac{dU^*}{dy_i} \equiv \frac{dU^*(x,y)}{dy} \Big|_{x_i,y_i}$ .

Let's assume that when we generate one new path, the start point  $\vec{x}_0$  is also chosen according to the equilibrium distribution, and this path arrives in state B in  $M$  steps, where  $M < N$ . Then the generating probability for this path is

$$D(\zeta) \propto \exp[-U^*(\vec{x}_0)] \prod_{i=0}^{M-1} g(\vec{x}_i, \vec{x}_{i+1}; \vec{x}_f; N) \prod_{j=M}^{N-1} p(\vec{x}_j, \vec{x}_{j+1}; U^*), \quad (\text{III.26})$$

where

$$\begin{aligned} g(\vec{x}_i, \vec{x}_{i+1}; \vec{x}_f; N) &= \frac{1}{\sqrt{2\pi}\sigma} \exp \left\{ -\frac{[x_{i+1} - x_i - (x_f - x_i)/(N - i)]^2}{2\sigma^2} \right\} \\ &\times \frac{1}{\sqrt{2\pi}\sigma} \exp \left\{ -\frac{[y_{i+1} - y_i - (y_f - y_i)/(N - i)]^2}{2\sigma^2} \right\}. \end{aligned} \quad (\text{III.27})$$

Finally the weight of a path generated by this method is

$$w(\zeta) = \frac{P(\zeta)}{D(\zeta)}. \quad (\text{III.28})$$

As shown in Ref[31], this procedure works well, for example, for a single particle moving on the two-dimensional surface. Inspired by this idea, a new generating procedure is applied in Sec.IV.B for a transition path sampling approach in one-dimensional space.

Dynamic importance sampling is mathematically straightforward and simple to apply. In principle, it is applicable for large biomolecular systems. The biggest challenge is finding the path generating methods for different problems. To improve its efficiency, new path generating methods will have to be developed. More details and applications can be found in Zuckerman, Jang and Woolf's papers [31, 67, 72, 88, 89].

### c. Discussion of optimal path-generating function

At first sight, the importance sampling approach discussed above is really impressive because it seems that any arbitrary generating method will lead to the right answer. But after error analysis as we sketch here, we conclude that a good choice is to make the generating density  $D(\zeta)$  proportional to the absolute value of  $F(\zeta) \equiv f(\zeta)P(\zeta)$ . A bad choice of  $D(\zeta)$  will give an poor statistical result. Following *Numerical Recipes in C* [90], let's try to find the optimal choice of  $D(\zeta)$ . For the function which is estimated

$$\langle f \rangle = \int f(\zeta)P(\zeta)d\zeta = \int \frac{F}{D}Dd\zeta \approx \left\langle \frac{F}{D} \right\rangle_D \pm \sqrt{\frac{\langle F^2/D^2 \rangle_D - \langle F/D \rangle_D^2}{N}}, \quad (\text{III.29})$$

where the angle brackets denote the mean value over  $N$  sampling points (or paths here) with distribution  $D$ . The last term of Eq.(III.29) is the error

$$\begin{aligned} \text{Error} &= \left\langle \frac{F^2}{D^2} \right\rangle_D - \left\langle \frac{F}{D} \right\rangle_D^2 \\ &\approx \int \frac{F^2}{D^2}Dd\zeta - \left[ \int \frac{F}{D}Dd\zeta \right]^2 \\ &= \int \frac{F^2}{D}d\zeta - \left[ \int Fd\zeta \right]^2. \end{aligned} \quad (\text{III.30})$$

The reason for the approximation in Eq.(III.30) is that the angle brackets are also Monte Carlo sampled estimators of the respective integrals. When  $F/D > 0$ , it is obvious that the best choice is  $D = F$  so that the error will vanish, but  $F/D$  can possibly be negative. We can find the general optimal  $D(\zeta)$  by extremizing

$$\frac{\delta}{\delta D} \left( \int \frac{F^2}{D}d\zeta - \left[ \int Fd\zeta \right]^2 + \lambda \int Dd\zeta \right) = 0, \quad (\text{III.31})$$

where  $\lambda$  is a Lagrange multiplier employed to ensure  $\int Dd\zeta = 1$ . Eq.(III.31) implies that

$$D = \frac{|F|}{\sqrt{\lambda}} = \frac{|F|}{\int |F|d\zeta}, \quad (\text{III.32})$$

minimizes the error. Usually  $F(\zeta) = f(\zeta)P(\zeta)$  is unknown from a sampling perspective, so the challenge in using dynamic importance sampling is to generate a good path ensemble.

The previous three path sampling approaches are the major simulation methods I used in my research. However there are additional path sampling and path generating methods. To provide additional background I will briefly summarize a few of them.

#### 4. Langevin dynamics in path space

In Eastman, Grønbech-Jensen and Doniach's paper [91], the authors presented an interesting path sampling method, which performs a random walk in path space by following a pseudo Langevin equation.

First, let's consider a multiple dimensional over-damped Langevin equation

$$\frac{d\vec{x}}{dt} = \frac{\vec{F}}{\gamma} + \vec{R}(t), \quad (\text{III.33})$$

where  $\gamma$  is the friction coefficient,  $\vec{F} = -\nabla U$  and  $U$  is the potential energy of the system, and  $\vec{R}$  represents a Gaussian white noise vector. In the limit of sufficiently small time step, Eq.(III.33) will produce a canonical probability distribution [8].

For a path  $\zeta = \zeta(\{\vec{x}_0, \vec{x}_1, \dots, \vec{x}_N\})$ , we have already shown its probability is

$$\begin{aligned} P_{path}(\zeta) &\propto \exp[-U^*(\vec{x}_0)] \times [\prod_{i=0}^{N-1} p(\vec{x}_i, \vec{x}_{i+1}; U^*)] \\ &\propto \exp[-U^*(\vec{x}_0)] \\ &\quad \times \left( \prod_{i=0}^{N-1} \frac{1}{\sqrt{2\pi\sigma}} \exp \left\{ -\frac{[\vec{x}_{i+1} - \vec{x}_i - \frac{1}{2}(-\nabla U^*)(2D\Delta t)]^2}{2\sigma^2} \right\} \right) \\ &\propto \exp \left( -U^*(\vec{x}_0) - \sum_{i=0}^{N-1} \frac{[\vec{x}_{i+1} - \vec{x}_i - \frac{1}{2}(-\nabla U^*)(2D\Delta t)]^2}{2\sigma^2} \right) \\ &\propto \exp \left( -\frac{S(\zeta)}{k_B T} \right), \end{aligned} \quad (\text{III.34})$$

where

$$S(\zeta) = \left\{ U^*(\vec{x}_0) + \sum_{i=0}^{N-1} \frac{[\vec{x}_{i+1} - \vec{x}_i - \frac{1}{2}(-\nabla U^*)(2D\Delta t)]^2}{2\sigma^2} \right\} k_B T. \quad (\text{III.35})$$

Suppose there is an initial trajectory  $\zeta$ ; then one performs the random walking in path space according to a pseudo-dynamical Langevin-like equation

$$\frac{d\vec{X}}{dt'} = -\frac{\nabla S}{\gamma'} + \vec{R}'(t'), \quad (\text{III.36})$$

where  $\gamma'$ ,  $t'$  and  $\vec{R}'$  are the pseudo friction coefficient, time and Gaussian white noise respectively. The vector  $\vec{X} = \{\vec{x}_0, \vec{x}_1, \dots, \vec{x}_N\}$  represents all the coordinates that define a whole path  $\zeta$ . So we can formally rewrite Eq.(III.36) as

$$\frac{d\zeta}{dt'} = -\frac{1}{\gamma'} \frac{dS}{d\zeta} + \vec{R}'(t'). \quad (\text{III.37})$$

Compared with Eq.(III.33), we know a simulation following Eq.(III.37) will give the right canonical probability distribution according to pseudo potential  $S$ .

This path sampling method has some connection with the transition path sampling method mentioned in Sec.III.C.1. Once the weight of a path is accessible, the path space can be explored by Monte Carlo simulation like transition path sampling; it can also be explored by Langevin dynamics. In addition to the three advanced path sampling approaches we mentioned early this chapter (see Sec. III.C.1, Sec. III.C.2 and Sec. III.C.3), this is another method that can also yield a correct path ensemble. Eastman, Grønbech-Jensen and Doniach have applied this approach to do reaction path annealing for protein folding, and to search for more realistic trajectories [91]. Beyond these applications, this method has found little application.

## 5. Transition interface sampling

A method for reaction rate calculations that should be mentioned here is named “transition interface sampling” (TIS), given by van Erp, Moroni and Bolhuis [92]. Indeed, it is a method measuring the probability flux with the help of transition path sampling. To apply the transition interface sampling method, one first chooses a reaction coordinate, and introduces a series of “interfaces” along it. In fact, these interfaces are the same as the borders of bins in the weighted ensemble approaches in Sec. III.C.2. As we show the example in Fig. 16, there are two well defined stable states  $A$  and  $B$ , and the “interfaces” are labeled  $\lambda_1, \lambda_2, \dots, \lambda_i, \dots, \lambda_{n-1}$ .  $\lambda_0$  and  $\lambda_n$  are the boundaries of states  $A$  and  $B$ , respectively.

The authors of the original paper [92] point out that the reaction rate is given by

$$k_{AB} = k_{A\Omega_1} \prod_{i=1}^{n-1} P_{i,i+1}. \quad (\text{III.38})$$

Here  $\lambda_1$  labels a closed surface in configuration space enclosing state  $A$  shown in Fig. 16. If we treat the outside space of  $\lambda_1$  as a state called  $\Omega_1$ ,  $k_{A\Omega_1}$  is the reaction rate between  $A$  and  $\Omega_1$ . According to the definition,  $k_{A\Omega_1}$  is the effective positive flux through interface  $\lambda_1$  from state  $A$ . Because the interface  $\lambda_1$  is very close to state  $A$ , this reaction rate  $k_{A\Omega_1}$  can be measured easily by brute force simulation.  $P_{i,i+1}$  in Eq.(III.38) is the probability that the system arrives at the interface  $\lambda_{i+1}$  before it goes back to state  $A$  once it leaves interface  $\lambda_i$ . So the right side of Eq.(III.38) is the total effective flux at the boundary of state  $B$ . Note that all the flux calculated in Eq.(III.38) crosses state  $A$  at the same time but arrives in state  $B$  distributed over time. Actually it gives the value of the reaction rate if  $A$  and  $B$  are the only two stable states, because for the whole system

$$\frac{dProb_B}{dt} \approx -\frac{dProb_A}{dt}, \quad (\text{III.39})$$

where  $Prob_A$  and  $Prob_B$  are the total probabilities in states  $A$  and  $B$ , respectively.

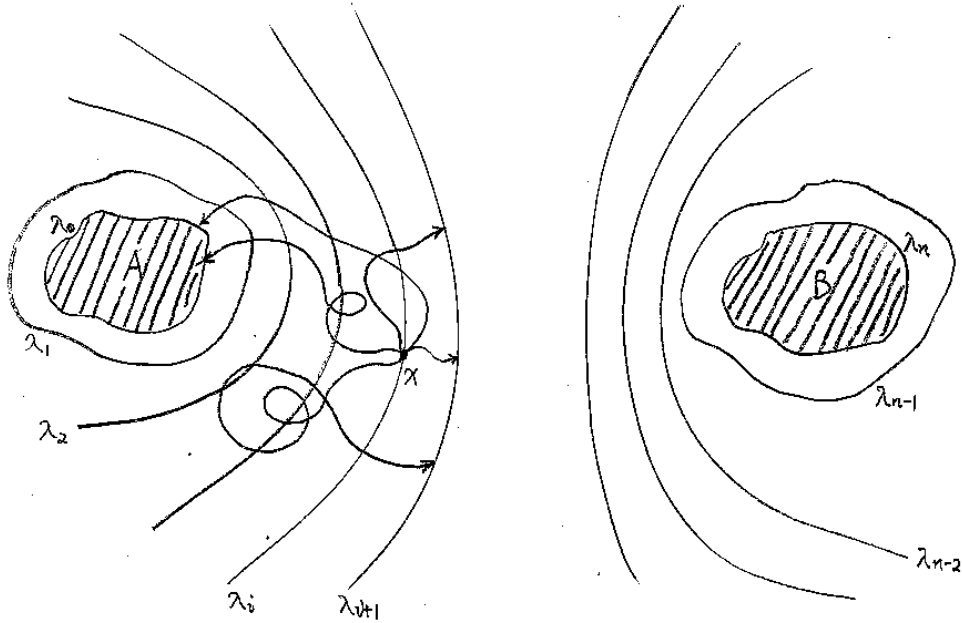


Figure 16: Schematic diagram of sampling for  $p(x_0)$  with given  $x_0$  in transition interface sampling.

The difficult part is the calculation of  $P_{i,i+1}$ , with  $\lambda_i$  as a continuous closed surface. We write this probability as

$$P_{i,i+1} = \int_{\lambda_i} \Pi_{\lambda_{i+1}}(x) \rho(x) dx, \quad (\text{III.40})$$

where  $x$  is one point in surface  $\lambda_i$ ,  $\Pi_{\lambda_{i+1}}(x)$  is the probability that the system arrives at interface  $\lambda_{i+1}$  before it goes back to state  $A$  once it leaves point  $x$ . If we treat  $\lambda_0$  and  $\lambda_{i+1}$  as two absorbing walls,  $\Pi_{\lambda_{i+1}}(x)$  is one of the splitting probabilities defined in Sec. II.E.2, and  $\rho(x)$  is the distribution for the start point  $x$  as shown below. In Fig. 16, we show a schematic diagram of sampling of  $\Pi_{\lambda_{i+1}}(x)$  with given  $x$ .  $\Pi_{\lambda_{i+1}}(x)$  is easy to get by brute force simulation again because  $\lambda_i$  and  $\lambda_{i+1}$  are close to each other and the relaxation to state  $A$  is very fast. But what is  $\rho(x)$ ? It is determined by the current at  $\lambda_i$ ,

$$\rho(x) = \frac{J(x)}{\int_{\lambda_i} J(x) dx}, \quad (\text{III.41})$$

where  $J(x)$  is current reaching point  $x$ . Then  $\rho(x)$  will be decided by the total probability of all the paths, which are between interfaces  $\lambda_0$  and  $\lambda_i$ , and start at start  $A$  and end at  $x$ . The choice of  $x$  on surface  $\lambda_i$  is done by the transition path sampling method, discussed in Sec. III.C.1.

Let's briefly review the steps of transition interface sampling:

- find the reaction coordinate and define the “interface”
- obtain the flux  $k_{A\Omega_1}$  by using brute force simulation
- generate the first path connecting state  $A$  and  $\lambda_1$ ,  $x$  is the position where this path ends in interface  $\lambda_1$
- get  $\Pi_{\lambda_2}(x)$  by running lots of brute simulations starting from  $x$ , which will end either in state  $A$  or  $\lambda_2$
- generate a new path connecting state  $A$  and  $\lambda_1$  from the old path, accept it with a probability  $\min[1, W^N/W^O]$ , where  $W^N$  and  $W^O$  are the weights of the new and old paths. If the new path is accepted, one will sample  $\Pi_{\lambda_{i+1}}(x)$  at new  $x$ , which is the position where this new path ends in  $\lambda_1$ . Otherwise one just uses the value  $\Pi_{\lambda_{i+1}}(x)$  giving by the old path one more time. Change  $x$  on this surface by transition path sampling and repeat until one reaches a converged value of  $P_{1,2}$ .

- move to the next interface and finally arrive at the border of state  $B$
- the reaction rate is given by  $k_{AB} = k_{A\Omega_1} \prod_{i=1}^{n-1} P_{i,i+1}$ .

For more detail and discussion please refer to Refs. [92–94].

Transition interface sampling method is a relatively new method and has not been applied widely. It is a better way to calculate reactions rate than the one given by the original transition path sampling method paper [75]. But its efficiency and accuracy may depend on the choice of the reaction coordinate and the set of “interfaces”. Because it is based on the transition path sampling, the failure of transition path sampling (for example, paths occur in multiple channels) will produce the wrong results.

## 6. Others

Almost simultaneously to the introduction of transition interface sampling, another method, called “milestoning” was developed by Faradjian and Elber [60, 95]. The milestoning method is similar to transition interface sampling in that it also divides space into volumes along a reaction coordinate, and glues all the information together to get the reaction rate. Allen and his coworkers introduced the “forward flux sampling” method later [96], which differs from the transition interface sampling method in the way of sampling  $\rho(x)$  in Eq.(III.41).

## D. PATH FINDING TECHNIQUES

We note that a number of *ad hoc* path generating approaches have been developed for biological systems [71, 97–104], but these do not lead to properly distributed path ensembles or timescales. Many earlier efforts have also been directed to determining single, optimal paths [101, 105–111].

### 1. Targeted molecular dynamics

Targeted molecular dynamics (TMD) is a tool for finding one transition path connecting given initial and targeted final conformations [98, 112]. It was first introduced by Schlitter,

Engels, Krüger, Jacoby and Wollmer in 1993 [98], and has become a quite popular approach for path finding. However the targeted molecular dynamics does not generate the true path ensemble, and should be distinguished from the previous path sampling methods.

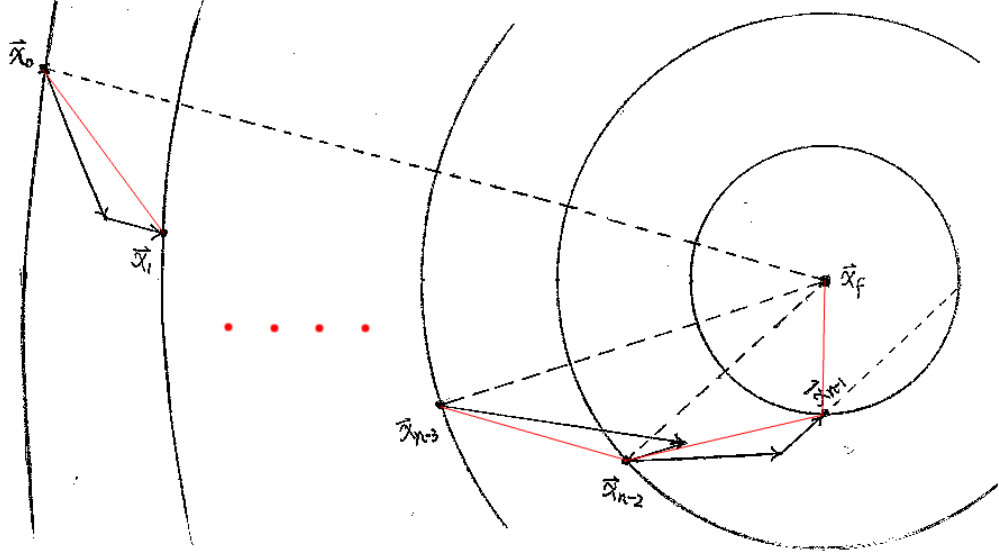


Figure 17: Schematic representation of two-dimensional targeted molecular dynamics. The red lines show the path from  $\vec{x}_0$  to  $\vec{x}_f$ . Between two points  $\vec{x}_i$  and  $\vec{x}_{i+1}$ , the first arrow is the displacement caused by the regular molecular dynamics  $\Delta\vec{x}_{i+1}^0$  and the second arrow is the additional displacement  $\Delta\vec{x}_{i+1}^a$ .

To apply the technique, one must first define a distance between two conformations. Following Schlitter, we use vector  $\vec{x} = x_1, x_2, \dots, x_j, \dots, x_{3N}$  to represent one molecular conformation. The distance between any conformation  $\vec{x}_i$  and the targeted final one  $\vec{x}_f$  is

$$\rho(\vec{x}_i) = |\vec{x}_i - \vec{x}_f| = \sqrt{\left[ \sum_j (x_{ij} - x_{fj})^2 \right]}. \quad (\text{III.42})$$

Then one decides on a total simulation time  $t_s$ . Targeted molecular dynamics will find a path with total number of steps  $n = t_s/\Delta t$ , where  $\Delta t$  is the time step. To complete this job,

an additional displacement in the conformational space will correct the regular molecular dynamics so that for each time step  $\Delta t$ , the average change of conformational distance is

$$\Delta\rho = \frac{\rho_0}{n} = \frac{|\vec{x}_0 - \vec{x}_f|}{n}, \quad (\text{III.43})$$

where  $\rho_0$  is the distance between initial and final conformations.

There are an infinite number of ways to adjust or bias the molecular simulation to satisfy Eq.(III.43). In the original paper [98], the additional displacement for the  $(i + 1)$ th step is chosen as

$$\Delta\vec{x}_{i+1}^a = k(\vec{x}_f - \vec{x}_i), \quad (\text{III.44})$$

where  $k$  is a parameter which will be calculated. For the  $(i + 1)$ th step simulation, the change in the conformational space is

$$\Delta\vec{x}_{i+1} = \vec{x}_{i+1} - \vec{x}_i = \Delta\vec{x}_{i+1}^0 + \Delta\vec{x}_{i+1}^a, \quad (\text{III.45})$$

where  $\Delta\vec{x}_{i+1}^0$  is the value given by the natural molecular simulation. Then the constraint Eq.(III.43) gives the equation for  $k$

$$(\vec{x}_{i+1} - \vec{x}_f)^2 - \rho_{i+1}^2 = 0, \quad (\text{III.46})$$

where

$$\rho_i = \rho_0 \frac{[n - i]}{n}. \quad (\text{III.47})$$

After substituting  $x_{i+1}$  by using Eq.(III.44) and (III.45), Eq.(III.46) becomes

$$(\vec{x}_f - \vec{x}_i)^2 k^2 + 2(\vec{x}_f - \vec{x}_i) \cdot (\vec{x}_i + \Delta\vec{x}_{i+1}^0 - \vec{x}_f)k + (\vec{x}_i + \Delta\vec{x}_{i+1}^0 - \vec{x}_f)^2 - \rho_{i+1}^2 = 0. \quad (\text{III.48})$$

This quadratic equation yields two values of  $k$ , which correspond to two points on the multiple dimensional sphere (or on the circle in two-dimensional space) whose radius is  $\rho_{i+1}$  and center is at  $\vec{x}_f$ . The lower absolute value will be taken. It is possible the solutions are imaginary, but we will not discuss that situation here. One will repeat doing this until the trajectory reaches the final targeted conformation. In Fig. 17, we show a schematic representation of two-dimensional targeted molecular dynamics.

Targeted molecular dynamics has been applied to finding the path of large protein conformational change, for example, GroEL [113], which is a protein “chaperone” that can assist the folding or unfolding of other proteins. This path generating approach is still under development by several groups [101]. The paths generated by targeted molecular dynamics carry no information of their weights. Then the relative importance of these paths is unknown. But for a big protein like GroEL, finding one path of conformational change is already very exciting. Targeted molecular dynamics has also been coded in CHARMM.

## 2. Steered molecular dynamics simulation

Steered molecular dynamics (SMD) was developed to reveal the microscopic processes underlying atomic force microscope (AFM) observations of ligand binding [114]. The basic idea is to apply an external harmonic force, with force constant close to those of AFM cantilevers, to the protein or ligand in the simulation [114–116]. The steered molecular dynamics simulation will not give the true path ensemble either. A schematic illustration is shown in the left panel of Fig. 18.

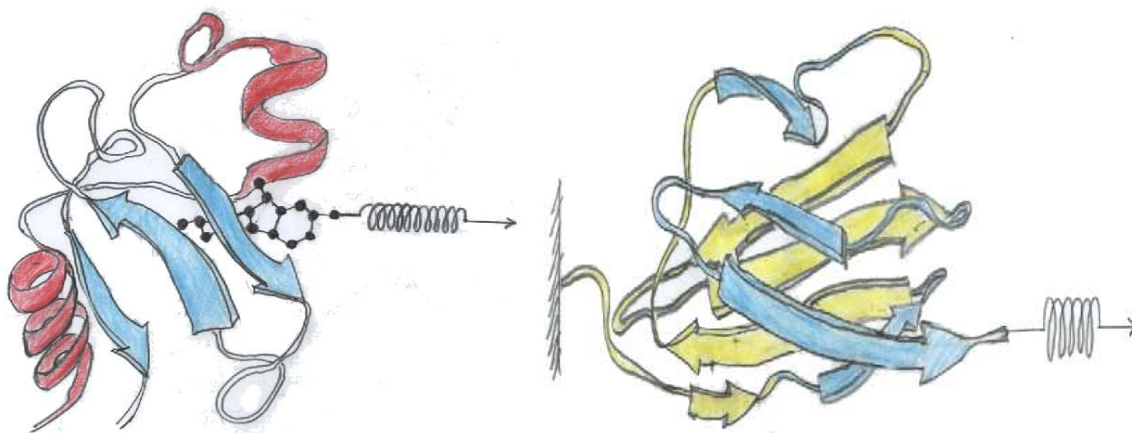


Figure 18: Schematic diagram of steered molecular dynamics simulation. The left panel shows the study of the rupture force of ligand binding. The right panel shows one Ig domain of titin, which will unfold when it is stretched. There are multiple tandem Ig domains in one titin protein [117].

Steered molecular dynamics simulation was used to study the transition between states because the external force can help the molecular system overcome the barrier and shorten the waiting time for a rare event [118]. The most successful example is the simulation for the modular protein titin done by Schulten and coworkers [117, 119]. Titin is a giant muscle protein, which is responsible for the passive elasticity of muscle. Some domains of titin will unfold one by one when it is pulled, just like a molecular spring. So steered molecular dynamics is an ideal method to study its unfolding pathway. In the right panel of Fig. 18, we show one tandem Ig domain of titin, whose extension increases the titin length by  $\sim 300\text{\AA}$ [117].

Like the targeted molecular dynamics, steered molecular dynamics will not give the weight of paths. Since the structure of the macromolecule changes under a steering force, these paths may not be close to the natural path only driven by thermal noise.

With the help of Jarzynski's equality [120, 121], steered molecular dynamics simulation can be used to calculate the potential of mean force [122], an interesting application, which, however, is beyond the scope of this thesis.

## IV. DURATION OF TRANSITION-EVENTS

### A. INTRODUCTION

In this chapter, we will study the distribution,  $\rho_b(t)$ , of the durations of transition-events over a barrier in a one-dimensional system. The results of this chapter have been reported in the Journal of Chemical Physics [123].

Basic aspects of the problem we address can be understood by examining Figs. 19 and 20, where we show a trajectory for a Brownian particle moving in a one-dimensional double-well potential. There are two timescales of primary interest [2]. One is the waiting time, or first passage time (FPT), which is the time the particle stays in one potential minimum before it goes to the other minimum. Theoretical analysis of the first passage time is largely a textbook subject now [7, 8]; see also [124–126] and Sec.II.E.1.

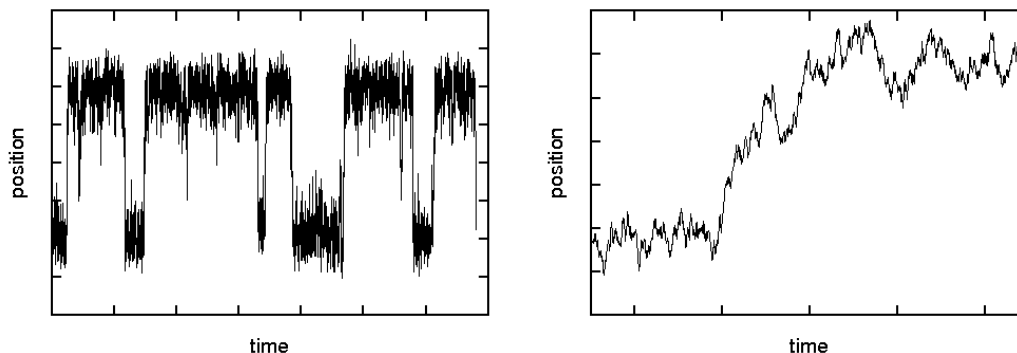


Figure 19: Trajectory for a Brownian particle moving in a double well potential. The left graph is a long trajectory with several transition-events. The right graph focuses on a single transition-event cut from the same long trajectory.

The other timescale — the focus of the present study — is that for just climbing over the barrier separating the two minima, *excluding the waiting time*. We refer to this as the “transition-event duration” or  $t_b$ , where the subscript connotes “barrier”; it has also been termed the “translocation time” in the context of membrane and pore traversal [127]. In the right-hand graph of Fig. 19, one transition-event extracted from the full time series on the left is shown at higher temporal resolution. The duration may be defined in a simple way, based on start and end points (or surfaces, more generally) as shown in Fig. 20: it is the interval between the last time the trajectory passes the start point and the first time it reaches the end point.

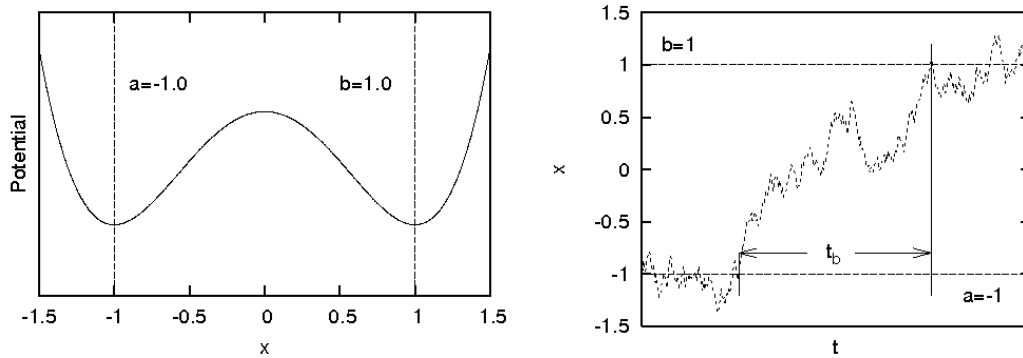


Figure 20: The definition of the transition-event duration,  $t_b$ . In the left graph, two boundaries are defined as the start point  $a$  and end point  $b$  of the transition. In the right graph,  $t_b$  is the duration between the last time the particle passes  $a$  and the first time it passes  $b$ . Note that our analysis does not require placement of the boundaries at the minima of the potential.

Several factors underscore the importance of the transition-event duration and its distribution. First, in molecular systems, the event duration directly reflects details of the reaction or isomerization mechanism, in that it is a characteristic of the reaction pathway. By contrast, the FPT convolves equilibrium fluctuations and transition dynamics. Second, in that a statistical mechanical description indicates that activated molecular processes generally may occur according to an *ensemble* of pathways and “speeds,” the distribution of the scalar event duration can be seen as the simplest quantitative measure of the heterogeneity

expected in transition-events. The need for an ensemble picture has been evident at least since saddle-point avoidance was discussed more than 20 years ago [105]. Not surprisingly, the statistics of event durations are of current biological interest in transport through ion channels [127–129], and polymer translocation through a pore [130–134]. Looking toward the future, the degree of heterogeneity in trajectories describing protein activity is a largely unaddressed general issue with potentially significant biochemical implications [53]. Recently developed nanosecond and femtosecond-scale experimental techniques [135, 136] one day may prove capable of directly probing transition-events.

The third factor highlighting the importance of the event-duration distribution is the considerable current interest in path sampling computations. These include quite a few methods explicitly incorporating the ensemble picture [59–61, 63, 64, 67, 76, 88, 91, 92, 94, 137]. Some of these approaches could benefit from a detailed description of the duration distribution [59, 61, 64, 67, 76, 88, 91, 137] although in principle, others do not require pre-determined knowledge regarding event durations [60, 63, 92, 94]. Aside from ensemble-based methods, other approaches seek optimal (single) paths [105–111].

Why study a one-dimensional description of transition-events, as is done in the present report? Our investigation was motivated by an earlier simulation study suggesting a close similarity between the distribution of transition-event durations in butane and a family of one-dimensional systems [72]: were there general lessons to be learned from an analytically tractable model? Analytical results, even for the simplest of one-dimensional systems, can provide a valuable theoretical reference point for future comparisons to molecular studies. Indeed, as will be seen, our analysis indicates which features of the distribution are expected to be general (system independent) and which will depend on details of a potentially complex energy landscape. Finally, we note that pore and channel systems can be considered effectively one-dimensional [127–134].

Transition-event durations have received previous theoretical attention. The earliest treatments were based on optimization of the Onsager-Machlup action [138]; see [139–148]. The *distribution* of transition paths is implicit in the “pre-history” description invoked by Dykman and colleagues [149–151]. Some explicit attention has been focused on the event-duration distribution [72, 127, 129, 131, 134, 152, 153]. Notably, the distribution was

studied in a phenomenological way by Zuckerman and Woolf [72], and Hummer provided an analytic formula for the mean transition-event duration for an arbitrary one-dimensional potential [152]; see also [131, 134]. Indirectly, Redner’s study of the first passage time in an interval supplies important precedents for our work [154], as does Gardiner’s book [7]. Two groups have recently discussed the time-reversal symmetry of the  $\rho_b$  distribution, albeit without attempting the detailed probe of the distribution itself [127, 129], which we pursue here. Other efforts directed at polymer translocation [130, 132, 133] investigated a related but distinct problem, critically differing in boundary conditions; see Sec. IV.C.

In this work, we attempt a rather complete description of the distribution of event durations for a class of one-dimensional systems. We first review the derivation of the probability distribution of the transition-event durations,  $\rho_b(t)$ , from the Fokker-Planck Equation (FPE) with particular boundary conditions. We then obtain novel results. A recursive formula for all the moments of  $\rho_b(t)$  is found, which permits accurate numerical approximations of  $\rho_b$  for an arbitrary potential. The short-time behavior of  $\rho_b$  is studied by path integral techniques, yielding universal behavior along with a potential-dependent correction. In turn, this leads to an estimate of an important characteristic time. For a bistable potential with a high barrier (i.e. a “double-well”), the long time behavior of  $\rho_b(t \rightarrow \infty)$  is described. The generality of the results — or their specificity to one-dimensional models — is discussed throughout and summarized in the Concluding Discussion.

## B. SIMULATION

All of our key analytic results to be discussed below have been confirmed via numerical simulation. Here our transition path sampling simulation approaches are briefly described.

The basic idea of transition path sampling has been introduced in Sec.III.C.1. To proceed, we must establish the equilibrium and generating probabilities in Eq.(III.5). The “equilibrium” probability  $P_{path}$  of the  $N$ -step path from  $a$  to  $x_N$  is the product of the equilibrium probability for the initial point and all subsequent single-step transition probabilities consistent with Eqs.(III.2) and (III.3). We further restrict our ensemble to “successful” paths

containing transition-events by formally introducing a projection operator  $\theta$ . Thus we have

$$P_{path}(\{a, x_1, \dots, x_N\}) \propto \exp[-U^*(a)] \times [\prod_{i=0}^{N-1} p(x_i, x_{i+1}; U^*)] \times \theta(\{x_i\}). \quad (\text{IV.1})$$

The single-step transition probability corresponding to Eqs.(III.2) and (III.3) is a Gaussian density, namely

$$p(x_i, x_{i+1}; U^*) = \frac{1}{\sqrt{2\pi}\sigma} \exp \left\{ -\frac{\left[ x_{i+1} - x_i - \frac{1}{2} \left( -\frac{dU^*}{dx_i} \right) (2D\Delta t) \right]^2}{2\sigma^2} \right\}. \quad (\text{IV.2})$$

where  $\frac{dU^*}{dx_i} \equiv \frac{dU^*(x)}{dx} \Big|_{x_i}$ . If the particle returns to the left boundary  $a$  before arriving at the right boundary  $b$ ,  $\theta = 0$ ; otherwise  $\theta = 1$ .

We employ a novel path generating procedure designed to focus simulation effort on the distribution  $\rho_b(t)$  of interest and, as necessary, on the rarest trial events. Our path generation strategy is closely related to a non-Metropolis re-weighting procedure previously considered by Zuckerman and Woolf [31]. Specifically, a trial path is built up “from scratch”, but based on the average behavior of the previous path. From the previous path, which starts from  $a$  and arrives at  $b$  after  $M_{old}$  ( $M_{old} < N$ ) steps without being re-absorbed at  $a$ , we can calculate the average velocity over total “time”  $2M_{old}D\Delta t$  as

$$\bar{v}(M_{old}) = \frac{b - a}{2M_{old}D\Delta t}. \quad (\text{IV.3})$$

This will be the “target speed” of the new trial path. This is extremely useful when studying the fastest events, whose transition-event durations are much shorter than  $\langle t \rangle_b$ .

To generate a new path, we linearly bias the particle from  $a$  to  $b$  using

$$x_{j+1} = x_j + (\bar{v}(M_{old}))(2D\Delta t) + \Delta x_R, \quad (\text{IV.4})$$

where  $\Delta x_R$  has been defined in Section III.B following Eq(III.2). Eq.(IV.4) may be compared to the unbiased form (III.2). The linear bias in (IV.4) is motivated by the quasi-ballistic quality of the fastest transition-events deriving from Eq.(II.108) in the limit  $E \gg DV_{max}$ , where  $V_{max}$  is the maximum of  $V(x)$  defined by Eq.(II.58). Thus, on the new path, the particle moves with a constant drift (bias) velocity, as if the force were constant, affected by ordinary noise. Note that for the new trajectory generated by Eq.(IV.4), the new value,

$M_{new}$ , can be larger or smaller than  $M_{old}$ . Once it arrives at  $b$ , we remove the bias and allow the particle to move for the remainder of  $N$  steps as governed by unbiased Brownian motion Eq.(III.2). As noted above, all the paths formally must contain the same number of steps for probabilities to be compared in our Metropolis procedure using Eq.(III.5); see, however, Ref. [94].

The generating probability (*gen*) for our procedure is the conditional probability with which we choose the new path, given the old one (with its average speed), namely,

$$gen(old \rightarrow new) = \prod_{i=0}^{M_{new}-1} \bar{g}(x_i, x_{i+1}; \bar{v}(M_{old})) \prod_{j=M_{new}}^{N-1} p(x_j, x_{j+1}; U^*), \quad (IV.5)$$

where

$$\bar{g}(x_i, x_{i+1}, \bar{v}(M_{old})) = \frac{1}{\sqrt{2\pi\sigma}} \exp \left\{ -\frac{[x_{i+1} - x_i - (\bar{v}(M_{old}))(2D\Delta t)]^2}{2\sigma^2} \right\}. \quad (IV.6)$$

This generating method is tailored to the potentials and boundary conditions we study in this paper, so that the Brownian particle will not be trapped in any position between the two absorbing walls.

By substituting Eqs.(IV.1),(IV.2),(IV.5) and (IV.6) into Eq.(III.5) we arrive at the acceptance criterion for our generating procedure, namely

$$R = \frac{\prod_{i=0}^{M_{new}-1} p(x_i, x_{i+1}, U^*) \theta_{new} \prod_{i=0}^{M_{old}-1} \bar{g}(y_i, y_{i+1}, \bar{v}(M_{new}))}{\prod_{i=0}^{M_{new}-1} \bar{g}(x_i, x_{i+1}, \bar{v}(M_{old})) \theta_{old} \prod_{i=0}^{M_{old}-1} p(y_i, y_{i+1}, U^*)}, \quad (IV.7)$$

given an old transition path  $(a, y_1, y_2, \dots, y_{M_{old}}, y_{M_{old}+1}, \dots, y_N)$  and a trial transition path  $(a, x_1, x_2, \dots, x_{M_{new}}, x_{M_{new}+1}, \dots, x_N)$ .

To ensure the correct behavior of our procedure and code, path-sampling results were carefully checked against direct simulation, using Eq.(III.2), in a number of cases. In the following sections of the paper, all the simulation results employ the path-sampling method just described.

We also checked that our path-sampling simulations greatly exceeded the correlation time resulting from our use of the ‘‘old’’ average velocity in Eq.(IV.3). This resulted in negligible statistical uncertainty, as can be gauged from the smoothness of the data in all path-sampling figures.

## C. TRANSITION-EVENTS

### 1. Distribution of transition-event duration

The distribution of transition-event durations,  $\rho_b(t)$ , for a Brownian particle confined to one dimension can be found by solving the Fokker-Planck equation using suitable boundary conditions, as we now describe [131, 134].

During the entire transition process the particle must move between  $a$  and  $b$ , which means that only trajectories that stay completely within the interval are considered, i.e.  $a \leq x(t) \leq b$  during the entire event. To eliminate the extraneous trajectories, absorbing walls must be put at the start and end points, [131, 134], so that

$$\begin{aligned} P(a, t) &= 0 \\ P(b, t) &= 0. \end{aligned} \tag{IV.8}$$

As recently stressed by Berezhkovskii [127], et al., the dual absorbing boundary conditions distinguish the event duration as a “conditional first passage time”, rather than the usual unconditional time associated with the Kramers’ problem [2, 127]. This contrasts with several previous studies of polymer translocation [130, 132, 133].

One releases particles very close to the left absorbing wall at  $t = 0$ , so that the initial condition is

$$P(x, 0) = \delta[x - (a + \epsilon)], \tag{IV.9}$$

with  $\epsilon \rightarrow 0+$ . Then the current at the right absorbing wall will determine the distribution,  $\rho_b$ , of durations according to

$$\rho_b(t) \propto \lim_{\epsilon \rightarrow 0+} J(b, t), \tag{IV.10}$$

with the currents given in Eq.(II.46). Following Gardiner’s work [7], let  $\pi_b(a + \epsilon|t)$  equal the probability that a particle, released at  $a + \epsilon$ , is absorbed at the right absorbing wall during  $0 < \tau < t$ . It is easy to see that

$$\pi_b(a + \epsilon|t) = \int_0^t J(b, \tau) d\tau. \tag{IV.11}$$

If we define

$$\Pi_b(a + \epsilon) \equiv \pi_b(a + \epsilon | \infty) = \int_0^\infty J(b, \tau) d\tau, \quad (\text{IV.12})$$

this “splitting probability” can be used to normalize  $\rho_b(t)$  in Eq.(IV.10) according to

$$\rho_b(t) = \lim_{\epsilon \rightarrow 0^+} \frac{J(b, t)}{\int_0^\infty J(b, \tau) d\tau} = \lim_{\epsilon \rightarrow 0^+} \frac{J(b, t)}{\Pi_b(a + \epsilon)}. \quad (\text{IV.13})$$

We note that the splitting probabilities are time-independent and follow directly from the potential  $U^*$  according to [7, 152]:

$$\begin{aligned} \Pi_a(x) &= \frac{\int_x^b \exp[U^*(x')] dx'}{\int_a^b \exp[U^*(x')] dx'} \\ \Pi_b(x) &= \frac{\int_a^x \exp[U^*(x')] dx'}{\int_a^b \exp[U^*(x')] dx'} = 1 - \Pi_a(x). \end{aligned} \quad (\text{IV.14})$$

Hence, to find the distribution of the transition-event durations,  $\rho_b(t)$ , one must solve the Fokker-Planck equation (II.44) with the initial condition (IV.9) and absorbing boundary conditions (IV.8). The current,  $J(b, t)$ , can be found from Eq.(II.46), which can then be combined with the splitting probabilities to find the normalized distribution of transition-event durations,  $\rho_b(t)$ .

## 2. Examples: free diffusion and linear potential

The solution of the Fokker-Planck equation can be formally expressed, in standard fashion, in terms of the eigenvalues and eigenfunctions of a time independent equation [8], as we mentioned in Sec.II.C.2.e. The solution can be written in the form

$$P(x, t) = \sum_n A_n p_n(x) e^{-\lambda_n t}, \quad (\text{IV.15})$$

where the eigenvalues  $\{\lambda_n\}$  are non-negative and, based on Eq.(II.44), the eigenfunctions satisfy

$$D \left\{ \frac{d}{dx} \left[ \frac{dU^*(x)}{dx} \right] + \frac{d^2}{dx^2} \right\} p_n(x) = -\lambda_n p_n(x). \quad (\text{IV.16})$$

Eq.(IV.16) with boundary conditions (IV.8) determine the functions  $\{p_n(x)\}$ , while the constants  $\{A_n\}$  are found from the initial condition (IV.9). The distribution  $\rho_b(t)$  follows from Eqs.(IV.13) and (IV.14). As examples, we determine  $\rho_b(t)$  for a few special potentials  $U^*(x)$ .

This will reveal some interesting features. We note that the linear potential, of which free diffusion is a special case, previously was studied by Lubensky and Nelson [131], although without numerical simulations.

*Free Diffusion.* Even in the absence of a true barrier, the event duration is still well defined by the formalism above, and this simple case acts as a useful reference. We therefore first consider free diffusion, with  $U^*(x) = 0$  and  $a = 0, b = L$ .

The solution of Eq.(IV.16) can easily be found, and the result can be formally expressed as

$$\rho_b^{(0)}(t) = 2D \sum_{j=1}^{\infty} (-1)^{j+1} \left(\frac{j\pi}{L}\right)^2 \exp\left(-\frac{j^2\pi^2}{L^2}Dt\right). \quad (\text{IV.17})$$

Notice that at long times the decay is exponential and dominated by the lowest eigenvalue.

The right-hand side of Eq.(IV.17) is well behaved for long time, but is not useful for  $t \rightarrow 0$ . We can re-cast the result in a format useful at short times by using the Poisson sum formula [155],

$$\sum_{n=-\infty}^{\infty} f(n) = \sum_{j=-\infty}^{\infty} \int_{-\infty}^{\infty} f(x) \exp(-2i\pi jx) dx, \quad (\text{IV.18})$$

for function  $f$ . We then find an alternative representation

$$\rho_b^{(0)}(t) = \frac{2L}{\sqrt{\pi Dt^3}} \sum_{j=0}^{\infty} \left[ \frac{(2j+1)^2 L^2 - 2Dt}{4Dt} \right] \exp\left[-\frac{(2j+1)^2 L^2}{4Dt}\right], \quad (\text{IV.19})$$

which can be used to extract the behavior as  $t \rightarrow 0$ , namely

$$\rho_b^{(0)}(t) \sim t^{-5/2} \exp\left[\frac{-L^2}{4Dt}\right], \quad t \rightarrow 0. \quad (\text{IV.20})$$

We note that Eq.(IV.19) can also be derived using an image method [154].

*Linear Potential.* The solution for the linear potential,  $U^*(x) = kx$ , which corresponds to a constant drift velocity, can also be formally written in terms of an eigenfunction expansion [131],

$$\rho_b(t) = 2D \sum_{j=1}^{\infty} (-1)^{j+1} \left(\frac{j\pi}{L}\right)^2 \left[ \frac{\sinh(kL/2)}{kL/2} \right] \exp\left\{-\frac{[(kL/2)^2 + j^2\pi^2]}{L^2}Dt\right\}. \quad (\text{IV.21})$$

Comparing with Eq.(IV.17), the result can be written

$$\rho_b(t) = \rho_b^{(0)}(t) \left[ \frac{\sinh(kL/2)}{kL/2} \right] \exp\left[-\frac{(kL/2)^2}{L^2}Dt\right]. \quad (\text{IV.22})$$

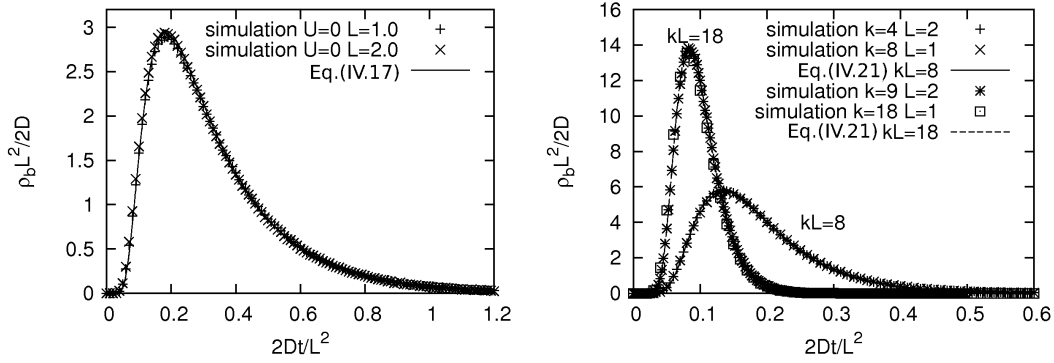


Figure 21: Scaled event duration distribution for free diffusion and the linear potential. The left graph is for free diffusion with different widths  $L$ , where data points are from path-sampling simulations and the solid line represents numerical evaluation of Eq.(IV.17). The right graph is for the linear potential  $U^* = kx$  with different widths  $L$  and different slopes  $k$ ; the points are data from path-sampling simulations and the lines are numerical evaluations of Eq.(IV.21).

In the left graph of Fig. 21 we show path-sampling simulation results following Section IV.B for  $\rho_b$  for free diffusion with  $U^* = 0$ ,  $L = 1.0$  and  $U^* = 0$ ,  $L = 2.0$ . They are compared with the numerical evaluations of Eq.(IV.17). The path-sampling simulations and numerical results from the eigenfunction expansions match very well. We changed the units of the vertical and horizontal axes, so that all the curves of  $\rho_b^{(0)}$  will not depend on the width  $L$ , and the generic behavior is highlighted.

In the right graph of Fig. 21 we show path-sampling simulation results for a series of parameterizations of linear potential:  $U^* = 4.0x$ ,  $L = 2.0$ ,  $U^* = 8.0x$ ,  $L = 1.0$ ,  $U^* = 9.0x$ ,  $L = 2.0$ , and  $U^* = 18.0x$ ,  $L = 1.0$ , which are compared to numerical evaluation of Eq.(IV.21). The simulation and numerical results again match very well. We again scaled the axes to emphasize that the shape of  $\rho_b$  only depends on the value of  $kL$ , which is essentially the potential energy difference between the start and end points. These exercises add confidence to the path-sampling methods used here.

### 3. Approximate solution for inverted parabolic potential

As a first investigation of a more realistic potential, we employ a crude representation of absorbing boundary conditions. In Fig. 22, inverted parabolic potentials are shown, one with open boundary conditions and the other with two absorbing walls ( $U^* \rightarrow -\infty$ ; see, e.g., [8]). When the “barrier” is high i.e., when  $U^*(0) \gg U^*(a = -1) = U^*(b = 1)$ , a particle exiting the region  $a < x < b$ , has a small likelihood of returning with open boundary conditions, because of the rapidly increasing “downhill” forces external to the region. Thus, as long as there is a sufficiently high barrier, one might conclude the solution for open boundary conditions will be a good approximation for an inverted parabolic potential with two absorbing walls. We now investigate this approximation.

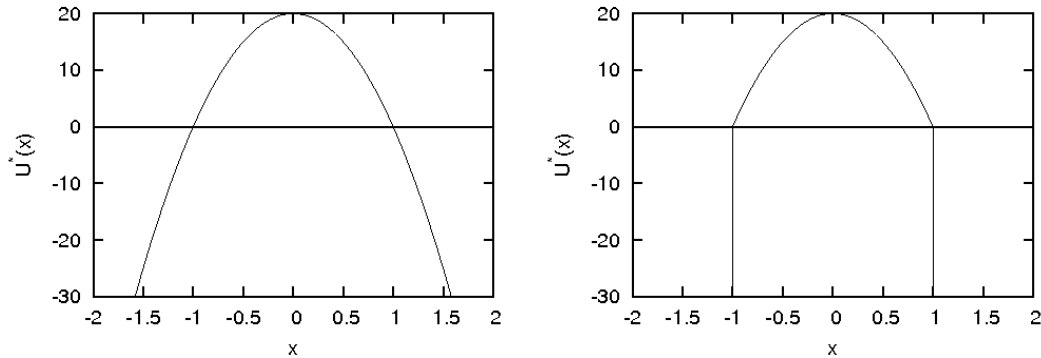


Figure 22: Inverted parabolic potential with different boundary conditions. The left graph is the inverted parabolic potential  $U^* = 20(1 - x^2)$ , with open boundary conditions, while the right graph is the same potential with two absorbing walls at  $x = -1$  and  $x = 1$ .

With open boundary conditions, the exact solution of the Fokker-Planck equation for an inverted parabolic potential,  $U^* = -\frac{1}{2}\alpha x^2$ , is well known [8]:

$$P(x, t) = \sqrt{\frac{\alpha}{2\pi[1 - \exp(-2\alpha Dt)]}} \exp\left\{-\frac{\alpha[x \exp(-\alpha Dt) - a]^2}{2[1 - \exp(-2\alpha Dt)]}\right\} \exp(-\alpha Dt), \quad (\text{IV.23})$$

which satisfies the initial condition

$$P(x, 0) = \delta(x - a). \quad (\text{IV.24})$$

For the same potential with absorbing walls at  $-W$  and  $W$ , we approximate the current from Eqs.(IV.23) and (II.46) with  $a = -W$  and  $b = W$ ,

$$J(W, t) = \left( \frac{D\alpha W}{4} \sqrt{\frac{\alpha}{\pi}} \right) \frac{\exp[-(\alpha W^2/2) \coth(\alpha Dt/2)]}{\sinh(\alpha Dt/2) \sqrt{\sinh(\alpha Dt)}}. \quad (\text{IV.25})$$

For normalization we will need

$$N = \int_0^\infty J(W, t') dt', \quad (\text{IV.26})$$

which is the total probability passing to the right of  $x = W$ . Under the influence of this inverted parabolic potential, this probability will not pile up but will flow toward  $x \rightarrow \infty$ .

Thus

$$N = \Pi_\infty(-W) = \frac{\int_{-\infty}^{-W} \exp(-\frac{1}{2}\alpha x^2) dx}{\int_{-\infty}^{\infty} \exp(-\frac{1}{2}\alpha x^2) dx} = \frac{\text{erfc}(W\sqrt{\alpha/2})}{2}, \quad (\text{IV.27})$$

from which one obtains the approximation

$$\rho_b(t) \simeq \left\{ \frac{D\alpha W}{2[1 - \text{erf}(W\sqrt{\alpha/2})]} \right\} \left( \sqrt{\frac{\alpha}{\pi}} \right) \frac{\exp[-(\alpha W^2/2) \coth(\alpha Dt/2)]}{\sinh(\alpha Dt/2) \sqrt{\sinh(\alpha Dt)}}, \quad (\text{IV.28})$$

where  $\text{erf}(x) = 1 - \text{erfc}(x) = \frac{2}{\sqrt{\pi}} \int_0^x \exp(-z^2) dz$  [156]. In Fig. 23 we compare the results from direct simulation and from Eq.(IV.28) for inverted parabolic potentials with different heights. In the simulations the two absorbing walls are placed at  $a = -1.0$  and  $b = 1.0$ ; then the height of the barrier is given by  $\alpha/2$ .

As expected, this approximation improves with increasing barrier height.

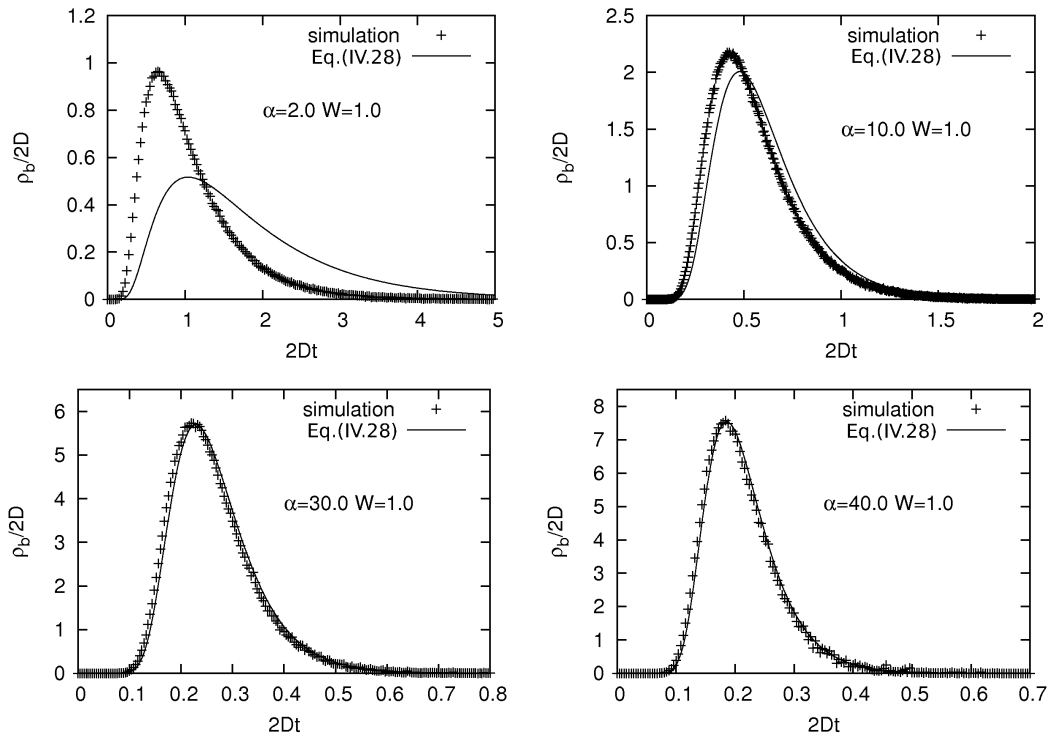


Figure 23: The event-duration distribution  $\rho_b$  for inverted parabolic potentials with different dimensionless barrier heights  $\frac{\alpha}{2}$ . The absorbing walls are at  $-W$  and  $W$ , with  $W = 1$ . The data are from path-sampling simulations (points) and numerical evaluations (lines) use the approximate formula, Eq.(IV.28). This approximation improves with increasing barrier height.

#### 4. Moments of the distribution of transition-event durations

##### a. Recursive formula

In studying a distribution, it is natural to investigate its moments. Gardiner [7] provides an expression for the first moment of  $\rho_b(t)$  (i.e., the mean time), which is also given by Hummer [152] and Chern et al. [134]. Here we derive a recursive formula for all *moments* of  $\rho_b(t)$ , as suggested by Gardiner [7].

Following Gardiner, we define  $g_b(x, t)$  as the total probability that the particle is absorbed

at  $b$  after time  $t$ , given that it is released at position  $x$  at  $t = 0$ . Thus

$$g_b(x, t) \equiv \int_t^\infty J(b, \tau) d\tau, \quad (\text{IV.29})$$

and we have the initial condition

$$P(x', 0) = \delta(x' - x). \quad (\text{IV.30})$$

The limiting cases for  $g_b(x, t)$  are

$$\begin{aligned} g_b(x, t = 0) &= \Pi_b(x) \\ g_b(x, t = \infty) &= 0, \end{aligned} \quad (\text{IV.31})$$

where  $\Pi_b(x)$  is defined in Eq.(IV.14) .

The  $n$ th moment,  $T_n$ , of the exit time distribution for particles released at arbitrary  $a < x < b$  can be calculated from  $g_b(x, t)$  according to

$$T_n(b, x) = - \int_0^\infty t^n \frac{\partial}{\partial t} \left[ \frac{g_b(x, t)}{g_b(x, 0)} \right] dt = \frac{n}{\Pi_b(x)} \int_0^\infty t^{n-1} g_b(x, t) dt, \quad (\text{IV.32})$$

so that  $T_n(b, a)$  is the  $n$ th moment of  $\rho_b$ . Gardiner [7] shows that  $g_b(x, t)$  satisfies the backward Fokker-Planck equation

$$\left( -D \frac{dU^*}{dx} \right) \frac{\partial g_b(x, t)}{\partial x} + D \frac{\partial^2 g_b(x, t)}{\partial x^2} = \frac{\partial g_b(x, t)}{\partial t}. \quad (\text{IV.33})$$

Multiplying by  $nt^{n-1}$  on both sides and integrating with respect to  $t$  yields

$$\left( -D \frac{dU^*}{dx} \right) \left[ n \int_0^\infty t^{n-1} \frac{\partial g_b(x, t)}{\partial x} dt \right] + D \left[ n \int_0^\infty t^{n-1} \frac{\partial^2 g_b(x, t)}{\partial x^2} dt \right] = n \int_0^\infty t^{n-1} \frac{\partial g_b(x, t)}{\partial t} dt. \quad (\text{IV.34})$$

Now the right side can be integrated by parts to find

$$n \int_0^\infty t^{n-1} \frac{\partial g_b(x, t)}{\partial t} dt = -n \Pi_b(x) T_{n-1}(b, x), \quad (\text{IV.35})$$

and with Eq.(IV.32),

$$\left( -D \frac{dU^*}{dx} \right) \frac{dy(x)}{dx} + D \frac{d^2 y(x)}{dx^2} = -n \Pi_b(x) T_{n-1}(b, x), \quad (\text{IV.36})$$

where

$$y(x) \equiv \Pi_b(x)T_n(b, x). \quad (\text{IV.37})$$

The boundary conditions on  $y(x)$  are

$$y(b) = y(a) = 0. \quad (\text{IV.38})$$

One way to solve equations like (IV.36) uses Green's functions [157]. The function that satisfies the homogeneous equation corresponding to Eq.(IV.36) with boundary condition (IV.38) at  $a$  is, in fact,  $\Pi_a(x)$ ; correspondingly at  $b$ , it is  $\Pi_b(x)$ . Using these solutions, one obtains a recursive formula for all the moments

$$\begin{aligned} T_n(b, x) = & \frac{n}{D} \left\{ \int_a^b \exp[U^*(x')] dx' \right\} \left\{ \frac{\Pi_a(x)}{\Pi_b(x)} \int_a^x \exp[-U^*(x')] \Pi_b^2(x') T_{n-1}(b, x') dx' \right. \\ & \left. + \int_x^b \exp[-U^*(x')] \Pi_a(x') \Pi_b(x') T_{n-1}(b, x') dx' \right\}. \end{aligned} \quad (\text{IV.39})$$

Our main interest is in the moments of  $\rho_b$ , namely,

$$T_n(b, a) = \frac{n}{D} \left\{ \int_a^b \exp[U^*(x)] dx \right\} \left\{ \int_a^b \exp[-U^*(x)] \Pi_a(x) \Pi_b(x) T_{n-1}(b, x) dx \right\} \quad (\text{IV.40})$$

Given the moments according to Eq.(IV.40), the distribution of transition-event durations,  $\rho_b(t)$ , can be reconstructed numerically, at least for a fixed range of  $t$ .

## b. Lowest eigenvalue

From Eqs.(II.46) and (IV.15) one knows that  $\rho_b(t)$  can be written in the series

$$\rho_b(t) = \sum_{n=1}^{\infty} C_n e^{-\lambda_n t}, \quad (\text{IV.41})$$

where the eigenvalues defined by Eq.(IV.16) satisfy  $0 < \lambda_1 < \lambda_2 < \lambda_3 < \dots$ . The eigenvalues, in particular  $\lambda_1$ , can be found via direct numerical solution of Eq.(IV.16). Here we show an alternative based on integrations involving the potential. The first eigenvalue  $\lambda_1$  can be expressed in terms of the high-order moments because of asymptotically exponential behavior. When  $n \gg 1$ ,

$$\begin{aligned} T_n(b, a) &= \int_0^{\infty} t^n \rho_b(t) dt \\ &= \Gamma(n+1) \frac{C_1}{\lambda_1^{n+1}} \left[ 1 + \frac{C_2}{C_1} \left( \frac{\lambda_1}{\lambda_2} \right)^{n+1} + \frac{C_3}{C_1} \left( \frac{\lambda_1}{\lambda_3} \right)^{n+1} + \dots \right], \end{aligned} \quad (\text{IV.42})$$

where  $\Gamma(n)$  is the Gamma function. The lowest eigenvalue can then be estimated from a ratio of high moments; for example,

$$\lambda_1 = \lim_{n \rightarrow \infty} \left[ \frac{T_n(b, a)}{T_{n+1}(b, a)} (n+1) \right], \quad (\text{IV.43})$$

and from Eq.(IV.42), the constant can be determined according to

$$C_1 = \lim_{n \rightarrow \infty} \frac{T_n(b, a) \lambda_1^{n+1}}{\Gamma(n+1)}. \quad (\text{IV.44})$$

Recalling that the moments can be constructed via successive integration, Eq.(IV.43) provides a way to estimate the first eigenvalue in Eq.(IV.41). In Section IV.C.6 Eq.(IV.43) will be used together with simulations to check an approximate analytic result for the leading eigenvalue in a representative case.

### c. First moment

For  $n = 1$ , using  $T_0(b, a) = 1$ , Eq.(IV.40) yields the first moment of the distribution of transition-event durations [152], see also [134],

$$T_1(b, a) = \frac{1}{D} \left\{ \int_a^b \exp[U^*(x)] dx \right\} \left\{ \int_a^b \exp[-U^*(x)] \Pi_a(x) \Pi_b(x) dx \right\}. \quad (\text{IV.45})$$

We can immediately evaluate  $T_1$  for the simple potentials. For free diffusion with  $U^* = 0$  and  $a = 0, b = L$ ,

$$\frac{2DT_1^0}{L^2} = \frac{1}{3}. \quad (\text{IV.46})$$

With  $U^* = kx, a = 0, b = L$ ,

$$\frac{2DT_1}{L^2} = \frac{2}{(kL)^2} \left[ kL \coth\left(\frac{kL}{2}\right) - 2 \right]. \quad (\text{IV.47})$$

For an inverted parabolic potential  $U^* = H(1 - \frac{x^2}{W^2})$ , where the curvature  $\alpha = \frac{2H}{W^2}$ , and  $a = -W, b = W$ , we can find an approximation of  $T_1$ . When  $H \gg 1$ , by using the method of steepest descents,

$$\int_{-W}^W \exp[U^*(x)] dx \approx \exp(H) \sqrt{\frac{2\pi}{\alpha}}, \quad (\text{IV.48})$$

and

$$\Pi_a(x) \Pi_b(x) \approx \frac{1 - \left[ \operatorname{erf}\left(\frac{x\sqrt{\alpha}}{\sqrt{2}}\right) \right]^2}{4}. \quad (\text{IV.49})$$

Then

$$\begin{aligned} 2DT_1 &\approx \sqrt{\frac{2\pi}{\alpha}} \int_0^W \exp\left(\frac{Hx^2}{W^2}\right) \left\{ 1 - \left[ \operatorname{erf}\left(\frac{\sqrt{H}x}{W}\right) \right]^2 \right\} dx \\ &= \frac{\sqrt{\pi}W^2}{H} \int_0^{\sqrt{H}} \exp(y^2) \{1 - [\operatorname{erf}(y)]^2\} dy \\ &= \frac{\sqrt{\pi}W^2}{H} \left\{ \int_0^1 \exp(y^2) \{1 - [\operatorname{erf}(y)]^2\} dy + \int_1^{\sqrt{H}} \exp(y^2) \{1 - [\operatorname{erf}(y)]^2\} dy \right\} \\ &\approx \frac{W^2}{H} [1.27 + \log(H)] = \frac{2}{\alpha} [1.27 + \log(H)]. \end{aligned} \quad (\text{IV.50})$$

Eq.(IV.50) provides a good approximation for  $T_1$  for the inverted parabolic potential with high barrier. It also gives a rough estimate of  $T_1$  for a “single-bump” barrier with height  $H$  and width  $2W$ .

Naively, one might guess  $T_1$  should simply be proportional to the effective frequency for the barrier top, namely, the inverse curvature  $\alpha^{-1}$ . However, this intuition falls short in two respects. First, the logarithmic term in Eq.(IV.50) is dominant for large barriers, for this simplest purely parabolic potential. Further, in extensive numerical work, for a double-well potential, we have seen unambiguously that the mean event duration is sensitive to details of the potential far from the barrier top (data not shown). This sensitivity can be traced to the dependence of the optimal “speed”, Eq.(II.108), on details of the potential. To give an extreme example, if there were a second barrier and minimum in the potential, then  $T_1$  would have to include the Kramers’ time for the second barrier.

#### d. Reconstruction of $\rho_b$ from moments

Reconstructing a function approximately from a finite number of moments has been studied, e.g., by maximum entropy method [158–160], continued fraction approach [161, 162], and Talenti method [163, 164] and perhaps other techniques. Here we follow Hon and Wei’s work [164] to reconstruct the density  $\rho_b(t)$  in a similar way.

First one builds up an orthonormal set of basis functions  $\psi_j(t)$ , which are polynomials,

$$\psi_j(t) = \sum_{n=0}^j c_{jn} t^n, \quad (\text{IV.51})$$

by using the standard Gram-Schmidt orthonormalization technique [157]. The polynomials satisfy

$$\int_0^\infty \psi_{j'}(t) \psi_j(t) w(t) dt = \delta_{jj'}, \quad (\text{IV.52})$$

with respect to a weight function  $w(t)$ , which is tailored to our problem with the choice

$$w(t) = \exp(-\lambda_1 t) \exp\left(-\frac{L^2}{4Dt}\right) (1 + t^{-\frac{5}{2}}), \quad (\text{IV.53})$$

where  $L = b - a$ . For this weight factor, when  $t \rightarrow \infty$ ,  $w(t) \sim \exp(-\lambda_1 t)$ , and when  $t \rightarrow 0$ ,  $w(t) \sim \exp\left(-\frac{L^2}{4Dt}\right) t^{-\frac{5}{2}}$ . These forms represent the long-time and short-time behaviors

for  $\rho_b(t)$  as we will show in Section IV.C.6 and IV.C.5 below. Thus we built in all the information we know about  $\rho_b(t)$  in this weight factor. Notice that  $\lambda_1$  can be found by following the scheme in Section IV.C.4.b, or via other numerical methods.

Following the usual Gram-Schmidt procedure, one builds up

$$\rho_m(t) = w(t) \sum_{j=0}^m a_j \psi_j(t), \quad (\text{IV.54})$$

which will be an approximation for  $\rho_b(t)$  of “order”  $m$ . If we incorporate moments of  $\rho_b$  by setting coefficients according to

$$\begin{aligned} a_0 &= \frac{T_0}{\int_0^\infty \psi_0(t) w(t) dt} = \frac{1}{c_{00} \int_0^\infty w(t) dt} \\ a_j &= \frac{T_j - \sum_{i=0}^{j-1} a_i \int_0^\infty t^j \psi_i(t) w(t) dt}{\int_0^\infty t^j \psi_j(t) w(t) dt}, \end{aligned} \quad (\text{IV.55})$$

then  $\rho_m(t)$  will reproduce the first  $m$  moments  $T_n$  ( $0 \leq n \leq m$ ), i.e.,

$$T_n \equiv \int_0^\infty t^n \rho_b(t) dt \approx \int_0^\infty t^n \rho_m(t) dt. \quad (\text{IV.56})$$

By using the first five moments, we reconstruct the distribution of transition-event durations for several different double-well potentials. These potentials are parameterized in the form

$$U^* = H \left[ 1 - \left( \frac{x}{W} \right)^2 \right]^2, \quad (\text{IV.57})$$

where  $H$  is the height of the barrier in units of  $k_B T$  and  $W$  is the half-width of the barrier. Two of the results are shown in Fig. 24. They match well with the simulations except for the long time tail as seen in the semi-log plot. However, the event probability in that region is quite small.

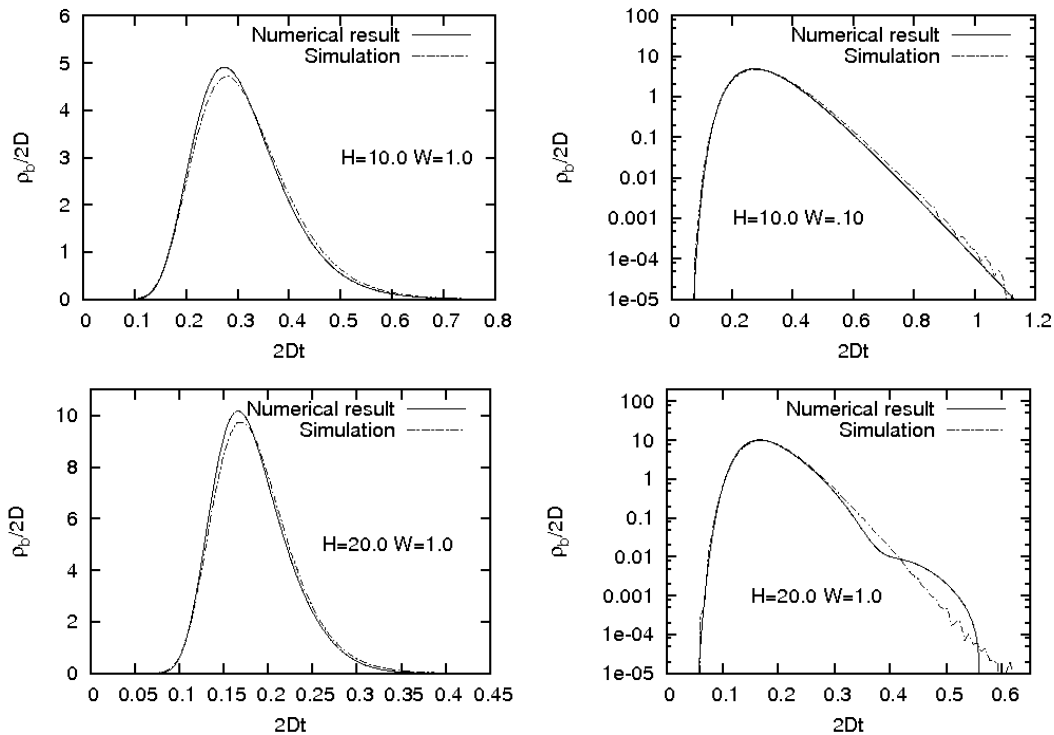


Figure 24: Reconstruction of  $\rho_b$  for double-well potentials of the form (IV.57) based on moments and a Gram-Schmidt procedure. The two absorbing walls are at  $-W$  and  $W$ , where  $W = 1$ . The data are from path-sampling simulations (dot-dash lines) and numerical results are based on the approximation in Section IV.C.4.a and IV.C.4.d, using the first five moments (solid lines). They match well except the long time tail as emphasized in the semi-log plot.

### e. Implications of moment calculations for molecular and high-dimensional systems

What lessons are contained in the preceding results for higher dimensional systems? The main point can be deduced from the first moment, which is given by Eq.(IV.45): In particular, the moments generally depend not only on details of the potential, but also on the definitions of the state boundaries (i.e.,  $a$  and  $b$  in our one-dimensional case). Nonetheless, qualitatively the first moment can be construed to set the overall (system-dependent) scale

for the distribution. Of greater interest are general features of the shape and functional form of the distribution, as was noted in an earlier empirical study of butane [72]. We will discuss those general aspects below.

## 5. Short time behavior

Beyond the moments, it is of interest to study the asymptotic behavior of the event-duration distribution, in both short and long time limits. We first analyze the  $t \rightarrow 0$  behavior<sup>1</sup>, using exact methods.

### a. Short time behavior for the green function with open boundary conditions

From the perspective of the path integral, introduced in Section II.D, if  $(t - t_0)$  is short, the velocity on the optimal trajectory  $\frac{dx_c}{dt}$  will be large. This implies a large “energy”  $E$  in Eq.(II.116). We therefore assume  $2E \gg 4DV$  and obtain the corresponding Green function for short time  $t$  with open boundary conditions,

$$G(x, t|a, t_0) \approx \exp\left(\frac{1}{2k_B T} \int_a^x F dx'\right) \frac{1}{\sqrt{4\pi D(t - t_0)}} \exp\left[-\frac{(x - a)^2}{4D(t - t_0)}\right] \times \exp[-\bar{V}(t - t_0)], \quad (\text{IV.58})$$

where  $\bar{V}$  is the average effective potential between  $a$  and  $x$ ,

$$\bar{V} = \frac{1}{x - a} \int_a^x V_s(x') dx'. \quad (\text{IV.59})$$

We have used the quadratic approximation, which is expected to be reasonable if the diffusion coefficient  $D$  is small [12]. Also, because we are further restricting our analysis to short-time behavior, the important paths will be close to the optimal one, which should improve the approximation.

---

<sup>1</sup>Of course time  $t$  can not go strictly to zero, since all the analysis is based on over-damped Brownian dynamics. Here time  $t$  is still much longer than the timescale  $\tau$  mentioned in Sec.II.A.1.

If we define  $G_0$  as the Green function for free diffusion with open boundary conditions [7],

$$G_0(x, t|a, t_0) = \frac{1}{\sqrt{4\pi D(t-t_0)}} \exp\left[-\frac{(x-a)^2}{4D(t-t_0)}\right], \quad (\text{IV.60})$$

Eq.(IV.58) can be expressed as

$$G(x, t|a, t_0) \approx G_0(x, t|a, t_0) \exp\left(\frac{1}{2k_B T} \int_a^x F dx'\right) \exp[-\bar{V}(t-t_0)], \quad (\text{IV.61})$$

which will be useful when we discuss the early time behavior with alternative boundary conditions below in Section IV.C.5.b.

### b. Short time behavior for the current with absorbing boundary conditions

In this subsection we need to retrace the path integral method in order to study transition-event durations, as required, with two absorbing walls.

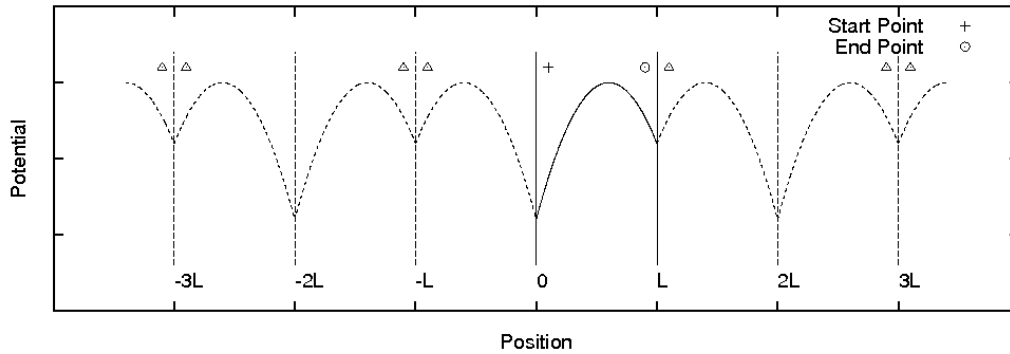


Figure 25: Calculating the path integral between the start point '+' and the end point 'o' with absorbing walls at  $x = 0$  and  $x = L$ . The solid curve represents an arbitrary potential between the two absorbing walls. Eq.(IV.62) indicates that one must calculate the path integrals between the start point '+' and all "end points", including the real one 'o' and image end points 'Δ', in the periodically repeated potential (dash line) with open boundary conditions.

As shown in Fig. 25, we wish to calculate the path integral from the start point '+' at  $x = (a+) = (0+)$  to the end point 'o' at  $x = (b-) = (L-)$  during the time interval

$(t - t_0)$ . There are two absorbing walls at positions  $x = 0$  and  $x = L$ , with some arbitrary potential between them. Note that we are making no assumptions about the symmetry of the potential in the interval  $[0, L]$ . If the position of the start point is  $\epsilon_1$  and the end point is  $x$ , then the Green function  $G^{abs}$  with absorbing boundary conditions can be expressed as a sum over Green functions  $G$  for open boundary conditions [21]

$$G^{abs}(x, t|\epsilon_1, t_0) = \sum_{j=-\infty}^{\infty} G(2jL + x, t|\epsilon_1, t_0) - \sum_{j=-\infty}^{\infty} G(2jL - x, t|\epsilon_1, t_0). \quad (\text{IV.62})$$

The construction is shown schematically in Fig. 25.

As shown above, to determine the distribution of event durations, we first calculate the current at  $x$ , then take the limits  $\epsilon_1 \rightarrow 0$  and  $x \rightarrow L$ ,

$$J^{abs}(L, t|0, t_0) = -2D \sum_{j=-\infty}^{\infty} \left. \frac{\partial G(x, t|0, t_0)}{\partial x} \right|_{x=(2j+1)L}. \quad (\text{IV.63})$$

From Eq.(IV.61), when  $(t - t_0)$  is small

$$\left. \frac{\partial G(x, t|0, t_0)}{\partial x} \right|_{x=(2j+1)L} \approx \left. \frac{\partial G_0(x, t|0+, t_0)}{\partial x} \right|_{x=(2j+1)L} \times \exp \left[ \frac{1}{2k_B T} \int_0^{(2j+1)L} F dx' \right] \times \exp[-\bar{V}_j(t - t_0)], \quad (\text{IV.64})$$

where the symmetry of the periodically continued potential has been used; see Fig. 25.

The periodicity implies further simplifications, including

$$\bar{V}_j = \frac{1}{(2j+1)L} \int_0^{(2j+1)L} V_s(x') dx' = \frac{1}{L} \int_0^L V_s(x') dx' = \bar{V}_0. \quad (\text{IV.65})$$

If we define the free diffusion current with absorbing boundary conditions as

$$J_0^{abs}(L, t|0, t_0) = -2D \sum_{j=-\infty}^{\infty} \left. \frac{\partial G_0(x, t|0, t)}{\partial x} \right|_{x=(2j+1)L}, \quad (\text{IV.66})$$

Eq.(IV.63) can be written

$$J^{abs}(L, t|0, t_0) \approx J_0^{abs}(L, t|0, t_0) \exp \left( \frac{1}{2k_B T} \int_0^L F dx' \right) \exp[-\bar{V}_0(t - t_0)], \quad (\text{IV.67})$$

or since the start and end points were arbitrary, we revert to our previous notation,

$$J^{abs}(b, t|a, t_0) \approx J_0^{abs}(b, t|a, t_0) \exp\left(\frac{1}{2k_B T} \int_a^b F dx'\right) \exp[-\bar{V}(t - t_0)] \quad (\text{IV.68})$$

where  $\bar{V}_0$  becomes

$$\bar{V} = \frac{1}{b - a} \int_a^b V_s(x') dx'. \quad (\text{IV.69})$$

We can now estimate the short time behavior of the normalized current.

### c. Short time behavior for the distribution of the transition-event durations

Combining Eq.(IV.13) and (IV.68), we find that the short-time behavior for the distribution of transition-event durations is given by

$$\rho_b(t \rightarrow 0) \approx \rho_b^{(0)}(t) \exp\left(\frac{1}{2k_B T} \int_a^b F dx'\right) \exp(-\bar{V}t) \left[ \lim_{\epsilon \rightarrow 0^+} \frac{\Pi_b^0(a + \epsilon)}{\Pi_b(a + \epsilon)} \right], \quad (\text{IV.70})$$

where  $\Pi_b^0(x)$  is the splitting probability for free diffusion and  $\rho_b^{(0)}$  is the distribution given in Eq.(IV.19) for free-diffusion with absorbing boundary conditions. From Eq.(IV.14)

$$\lim_{\epsilon \rightarrow 0^+} \frac{\Pi_b^0(a + \epsilon)}{\Pi_b(a + \epsilon)} = \frac{\int_a^b \exp[U^*(x')] dx'}{\exp[U^*(a)](b - a)}. \quad (\text{IV.71})$$

Combining Eq.(IV.70) and (IV.71), and using  $F(x) = k_B T \left(-\frac{dU^*}{dx}\right)$ , the normalized distribution becomes

$$\rho_b(t \rightarrow 0) \approx \rho_b^{(0)}(t) \left\{ \frac{\int_a^b \exp[U^*(x')] dx'}{\exp[U^*(a)](b - a)} \right\} \exp\left[\frac{U^*(b) - U^*(a)}{2}\right] \exp(-\bar{V}t), \quad (\text{IV.72})$$

revealing corrections to the free diffusion result due to the potential. Combining this result with Eq.(IV.20) one can find the short time behavior corrected by the potential. Note, as  $t \rightarrow 0$  the behavior is dominated by  $\rho_b^{(0)}$ .

In Fig. 26 we compare the results from a path-sampling simulation as described in Sec. IV.B and our final result Eq.(IV.72) for two double-well potentials of the form (IV.57) of varying barrier height. Absorbing walls are placed at  $x = \pm W$ , with  $W = 1$ . The simulations and the analytic results of Eq.(IV.72) are in good agreement at sufficiently early times, although at the earliest times the simulations reveal degraded statistics.

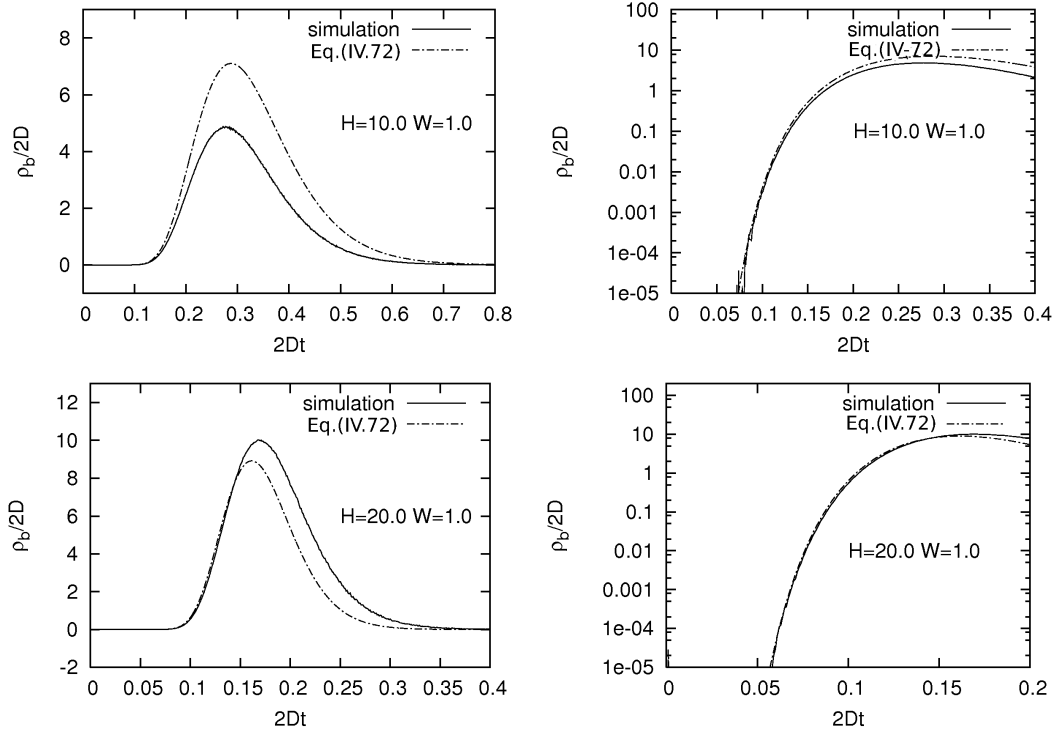


Figure 26: Short time behavior of  $\rho_b$  for double-well potentials of the form (IV.57). Data from path-sampling simulations (solid lines) are compared to the approximation (IV.72) for  $\rho_b(t \rightarrow 0)$  (dashed lines). The approximation and the simulations agree closely on the extent of the transient regime.

More importantly, Eq(IV.72) provides a means for estimating the characteristic time  $t^*$  at which the effect of the underlying potential  $U$  becomes comparable to that resulting from free diffusion embodied in  $\rho_b^{(0)}$ . In particular, by equating arguments of the exponentials in Eq.(IV.20) and in  $\exp(-\bar{V}t)$  from Eq.(IV.72), one finds  $(b-a)^2/2Dt^* \sim \bar{V}t^*$ . For a double-well potential of the form (IV.57), this implies  $2Dt^* \simeq 3.6W^2/H$ , which for  $W = 1$  and  $H = 10, 20$  (as in Fig. 26) yields  $2Dt^* \simeq 0.36, 0.18$ , respectively. Comparison of these values with Fig. 26 indicates that  $t^*$  captures the overall “scale” of the distribution remarkably well. This echoes the agreement seen in Fig. 26 between the simulation and the approximation Eq.(IV.72) for the onset of the physically important regime of  $\rho_b$  following the transient period. Qualitatively,  $t^*$  arises from the geometric mean of a free-diffusion time and a time

characteristic of the potential. Accordingly,  $t^* \sim W^2/DH$  is expected for simple barriers of the form  $U^* \sim Hf(x/W)$ .

#### d. Implications for the short-time behavior of complex systems

Based on the preceding results, some interesting mathematical and physical observations can be made, even for systems with more degrees of freedom. First, the asymptotic behavior of (IV.72) is *universal* in that it does not depend on potential function (see Eq.(IV.20)). It depends on the arbitrary boundaries, furthermore, in a trivial way. A first physical reading of Eq. (IV.72) suggests that when the system is forced to traverse a ‘barrier’ (broadly defined — it could be a series of barriers) fast enough, the trajectories will behave diffusively, as if there were no barrier.

While extremely rapid crossings are clearly unphysical, they are built in to the Fokker-Planck description arising from Langevin dynamics with white noise. Appropriately, however, such processes make a negligible contribution. Intuitively — for instance, from a consideration of the discrete description embodied in Eqs. (IV.1) and (IV.2) — there is a competition between the tendency toward the tight “stretching” of short trajectories (and hence, uniformity of speed) as opposed to conformity to the underlying potential (implying non-uniformity). At very short times, uniformity wins. However, the cost is high: such tightly stretched trajectories, which do not “feel” the potential, are damped via an essential singularity  $\sim \exp(-1/t)$ . Their probability is near-zero in comparison to slower trajectories. This point is consistent with previous simulation results reported by one of the authors [72], in which duration distributions for butane and toy models clearly were *not* described by ‘weaker’ mathematical forms.

In fact, our short-time path-integral analysis estimates, in  $t^*$ , the onset of the physically important trajectories. In other words, our asymptotic calculation is able to capture a physically relevant timescale.

The competition between tight stretching and non-uniformity should be expected in stochastic descriptions of molecular systems, as well. In other words, the transient region of near-zero probability at short times should be a general feature of distributions of transition-

event durations. The Fokker-Planck formalism thus supplies the mathematical underpinnings for the transient region, which is one of the characteristic features of the shape of the duration distribution. Not surprisingly, this suppression was also found in deterministic/Newtonian transition trajectories in a recent study [153], in addition to having been seen in the complex permeation processes studied by Hummer [128].

## 6. Long time behavior for double-well potential

From Eqs.(II.46) and (IV.15) we know that the long time behavior of  $\rho_b(t)$  will be determined primarily by the first eigenvalue  $\lambda_1$ . Here we use a perturbative approach to obtain an approximation for  $\lambda_1$  for a double-well potential with high barrier. We confirm, by direct numerical calculation, the validity of using perturbation theory. We also perform path-sampling simulations to check the accuracy of our final approximation.

By a variable transformation, the one-dimensional Fokker-Planck equation can be transformed to a Schrödinger-like equation [8], which has been discussed in Sec.II.C.2.d.

We will consider double-well potentials as in Eq.(IV.57) having high barriers,  $H \gg 1$ , and fixed half width,  $W$ . The absorbing walls are placed at the two minima,  $x = \pm W$ . The Schrödinger potential corresponding to (IV.57) is

$$V_s(x) = D \left[ \frac{2H}{W^2} + \left( \frac{4H^2}{W^4} - \frac{6H}{W^4} \right) x^2 - \frac{8H^2}{W^6} x^4 + \frac{4H^2}{W^8} x^6 \right]. \quad (\text{IV.73})$$

In Fig. 27 we plot  $U^*(x)$  and  $V_s(x)$  for a double-well with sufficiently high barrier. For the potential in the Schrödinger picture,  $V_s = +\infty$  outside the central interval to ensure the wave functions  $\phi_n(x)$  vanish at the ends of the interval, thus satisfying the absorbing boundary conditions.

We use perturbation theory to describe the lowest stationary state, which must exist because of the boundary conditions. For sufficiently high barriers, we expect that, the lowest eigenstate will be localized at the central minimum, suggesting the use of a perturbation process based on a simple harmonic oscillator. Using a numerical procedure for bound-state solutions of the time-independent Schrödinger equation [30], we confirmed this localization

for high barriers. We also note that for high barriers, the oscillator's Gaussian wave function nearly vanishes at the boundaries, in approximate satisfaction of the proper boundary conditions.

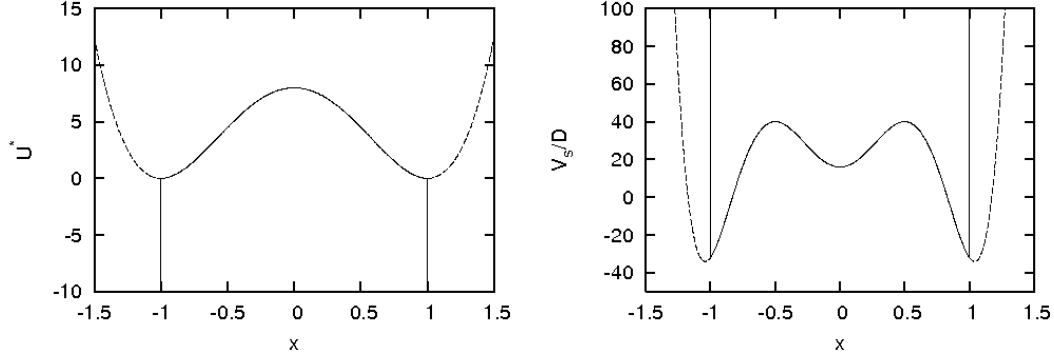


Figure 27: A high-barrier double-well potential  $U^*$  (left) and its Schrödinger analogue  $V_s$  (right) from Eqs.(IV.57) and (IV.73), for  $H = 8$  and  $W = 1$ . The two absorbing walls are put at the two minima. If the barrier height of the potential  $U^*$  is not sufficiently large, the minimum of  $V_s$  at  $x = 0$  will disappear.

Our perturbation calculation is therefore based on separating off the dominant harmonic component of  $V_s$ , noting  $H \gg 1$ , using

$$V_s(x) = V_0(x) + V_1(x), \quad (\text{IV.74})$$

where

$$V_0(x) = D \left( \frac{2H}{W^2} + \frac{4H^2}{W^4} x^2 \right), \quad (\text{IV.75})$$

$$V_1(x) = D \left( -\frac{6H}{W^4} x^2 - \frac{8H^2}{W^6} x^4 + \frac{4H^2}{W^8} x^6 \right). \quad (\text{IV.76})$$

From textbook results for a linear harmonic oscillator, the first eigenvalue and wave function are

$$\lambda_1^{(0)} = D \left( \frac{4H}{W^2} \right), \quad (\text{IV.77})$$

$$\psi_1^{(0)}(x) = \frac{\sqrt{\gamma}}{\pi^{1/4}} \exp \left( -\frac{1}{2} \gamma^2 x^2 \right), \quad (\text{IV.78})$$

where

$$\gamma = \left(\frac{2H}{W^2}\right)^{1/2}. \quad (\text{IV.79})$$

The first order perturbative correction is

$$\lambda_1^{(1)} = \int \psi_1^{(0)*} V_1(x) \psi_1^{(0)} dx = D \left[ -\frac{3}{W^2} + \mathcal{O}\left(\frac{1}{HW^2}\right) \right], \quad (\text{IV.80})$$

which is down by a factor of  $H$  from the zero order result. The second order correction is down by another factor of  $H$ :

$$\lambda_1^{(2)} = \sum'_m \left\{ \frac{|V_{m1}|^2}{\lambda_1^{(0)} - \lambda_m^{(0)}} \right\} \sim D \left[ \mathcal{O}\left(\frac{1}{HW^2}\right) \right]. \quad (\text{IV.81})$$

The net result for the lowest eigenvalue is thus

$$\lambda_1 = D \left[ \frac{4H}{W^2} - \frac{3}{W^2} + \mathcal{O}\left(\frac{1}{HW^2}\right) \right] \quad (\text{IV.82})$$

$$= D \left[ \alpha - \frac{3}{W^2} + \mathcal{O}\left(\frac{1}{HW^2}\right) \right], \quad (\text{IV.83})$$

where  $\alpha = 4H/W^2$  gives the curvature at the top of the barrier.

Eq.(IV.83) shows that the long time behavior is simply linear in the barrier-top curvature  $\alpha$ , for large values of  $\alpha$  and fixed  $W$ . This is also the case for the inverted parabolic potential, as can be determined from Eq.(IV.28), or by performing the same calculation as we did for the double-well in this section. In fact, when  $D\alpha t \gg 1$ , Eq.(IV.28) becomes

$$\rho_b(t) \simeq \left[ \frac{D\alpha W}{1 - \text{erf}(W\sqrt{\alpha/2})} \right] \left( \sqrt{\frac{2\alpha}{\pi}} \right) \exp\left(-\frac{\alpha W^2}{2}\right) \exp(-D\alpha t). \quad (\text{IV.84})$$

We therefore expect similar linearity with  $\alpha$  in the higher barrier limit for any system that can be approximated by an inverted parabola and a high order correction.

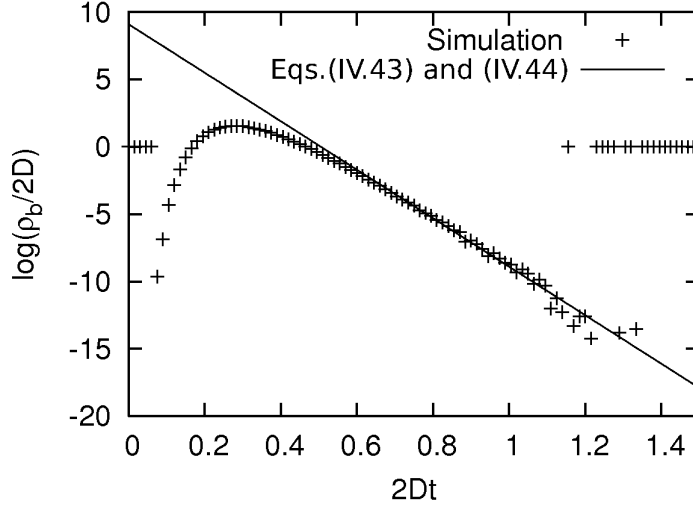


Figure 28: Comparison of two numerical approaches for computing the long time behavior of the event-duration distribution. A path-sampling simulation is compared to pure exponential behavior based on the lowest eigenvalue  $\lambda_1$  determined from Eqs.(IV.43) and (IV.44) with  $H = 10$  and  $W = 1$ . Similar results are obtained for other high barrier cases.

We performed numerical checks of the approximation (IV.83). We determined the lowest eigenvalue  $\lambda_1$  numerically using high moments and Eq.(IV.43). We also used path-sampling simulations as a consistency check. Fig. 28 compares the numerical evaluation of  $\lambda_1$  via Eqs.(IV.43) and (IV.44) with a path-sampling simulation data for a particular double-well potential.

In Fig. 29, we compare Eq.(IV.83) with numerical calculations of  $\lambda_1$  for double-well potentials and inverted parabolae with fixed  $W$  and a range of effective curvatures ( $\alpha = 10 - 100$ ) and plot  $\lambda_1/D\alpha$  as a function of dimensionless curvature  $\alpha W^2$ . As Eq.(IV.83) predicts,  $\lambda_1/D\alpha$  approaches unity for large curvature. This simple dependence contrasts with that for the first moment  $T_1$ , in Eq.(IV.50).

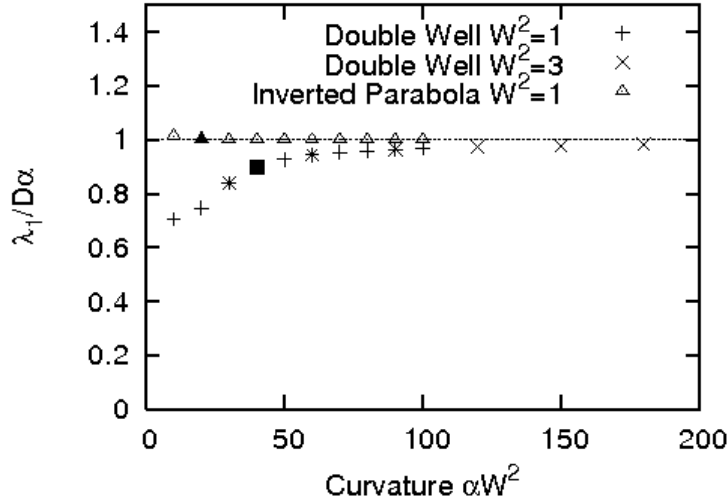


Figure 29: Long time behavior of  $\rho_b$  for double-well potentials and the inverted parabola. Exact numerical results for the lowest eigenvalue  $\lambda_1/D\alpha$  are plotted as a function of the dimensionless curvature  $\alpha W^2$  at the barrier peaks. The values of  $\lambda_1/D\alpha$ , which dominate the long-time behavior, approach 1 for large curvatures, as predicted by Eq.(IV.83). Note that barrier heights are proportional to  $\alpha$  for the models considered. Two double-well potentials with fixed  $W^2 = 1$  and  $W^2 = 3$ , and one inverted parabola system with fixed  $W^2 = 1$  are considered. Filled symbols indicate the  $\alpha$  values where the barrier height  $H$  is 10 (in units of  $k_B T$ ).

## 7. Implications for long-time behavior in complex systems

Unlike the asymptotic short-time behavior, the lowest eigenvalue of Eqs. (IV.15) and (IV.16) clearly depends on the form of the potential. While that dependence is simple for the smooth potential studied here, one cannot expect the simplicity to be a general rule for more complicated systems. In a rough molecular landscape, characterized by many barriers of varying heights [106], the long-time behavior will reflect a convolution of “micro-barrier-crossings.”

Perhaps the most important and general statement regarding the long-time behavior is the simplest: the eigenfunction decomposition of Eqs. (IV.15) and (IV.16) indicates that the

slowest trajectories will follow an exponential distribution. While this is not surprising, we emphasize that the event duration is *not* generated from a Poisson process — unlike typical treatments of the Kramers waiting-time. Nevertheless, the exponential long-time behavior should be a general characteristic of the distribution of durations, even in high dimensional systems.

#### D. CONCLUDING DISCUSSION

Langevin dynamics with white noise is widely used to study a variety of transitions or activated processes. We have applied a combination of analytic and numerical techniques to study the distribution,  $\rho_b(t)$ , of the durations of transition-events over a barrier in a one-dimensional system undergoing over-damped Langevin dynamics. The typical event duration is much shorter than the well-studied first passage time (FPT) [127]; see Figs. 19 and 20. The event duration is the simplest non-trivial measure of the detailed dynamics of an activated process, and we believe it is critical for future quantitative study of dynamics of many chemical and biological systems [72].

The distribution  $\rho_b(t)$  can be derived from the Fokker-Planck equation with special boundary conditions and was subjected to detailed analysis. A number of results are obtained, including: (i) the analytic form of the asymptotic short-time behavior ( $t \rightarrow 0$ ), which is universal and independent of the potential function; (ii) the first non-universal correction to the short-time behavior, which leads to an estimate of a key physical timescale; (iii) following Gardiner [7], a recursive formulation for calculating, exactly, all moments of  $\rho_b$  based solely on the potential function — along with approximations for the distribution based on a small number of moments; (iv) a high-barrier approximation to the long-time ( $t \rightarrow \infty$ ) behavior of  $\rho_b(t)$ ; and (v) a rough but simple analytic estimate of the average event duration  $\langle t \rangle_b$ , which generally is sensitive to details of the potential. All of the analytic results are confirmed by transition-path-sampling simulations.

Despite the simplicity of the models studied, a number of conclusions can be drawn concerning the characteristic shape of the distribution of event durations expected even

in *molecular* systems. First, the universal  $\exp(-1/t)$  short-time behavior suggests that transient regions (of near-zero probability) will be a general feature of the distribution for white-noise Langevin dynamics. The transient regime of the distribution is consistent with the intuitive notion that there is, effectively, an absolute minimum time required for physically reasonable trajectories. Second, the long-time behavior is expected to be exponential, since we anticipate the generality of the eigenfunction decomposition. Finally, even the one-dimensional models indicate that average event duration will be system-dependent, so this clearly will be the case for more complicated systems. These observations can be summarized in a very rough, but perhaps useful description of the shape of the distribution of event durations: once the system-dependent average behavior has been scaled out [72], the distribution is characterized by a nearly zero transient regime, a rapid rise to a peak of typical events, and an exponential tail of slower transitions.

A number of interesting questions remain open. First, how can the detailed relationship between  $\rho_b$  and first passage-time distribution be quantified, if at all? The distribution of first-passage times, after all, cannot be a simple exponential if the event durations are finite. Second, can the rough sketch we have suggested for  $\rho_b$  in complex systems be refined? A particular interest is in conformational transitions in proteins, which have only recently become amenable to study [53, 165, 166]. Furthermore, it is relevant to consider how non-white noise, implicit in a reduced description of molecular systems [72], affects event durations.

## V. WE SIMULATION FOR CAM

### A. INTRODUCTION

In this chapter, we will employ the “weighted ensemble” path sampling method to generate an unbiased ensemble of paths for a conformational transition in a 210-dimensional model of the protein calmodulin, and also find the reaction rate. The results of this chapter have been reported in the Proceedings of the National Academy of Sciences [85].

It has long been appreciated that conformational changes in proteins are critical to biological function. As we mentioned in Sec.III.C, because the traditional molecular simulations are inadequate to the task of studying large conformational transitions in macromolecules, three basic approaches to the problem of long-time macromolecular dynamics have been explored by a number of investigators. Of those, path sampling is of interest here.

Despite these important studies mentioned in Sec.III.C, a critical question remains: Do the path sampling methods work? That is, do they yield unbiased results which would be obtained with sufficient resources via brute-force simulation? While the question has been answered in the affirmative for some toy models [31, 63, 72, 75] molecular systems include major difficulties not present in simpler cases. The present study appears to be unique among path-sampling investigations of proteins because we *verify* the results by comparison with brute-force simulations.

We study conformational transitions in a “double-native” G $\bar{o}$  model introduced in Ref. [53] and since adapted to other contexts [165–167]. It is a united-residue model of calmodulin’s N-terminal domain constructed to be stable in two highly distinct experimentally determined conformations [53], one corresponding to the calcium-bound state (*Holo*) and the other being calcium-free (*Apo*). These structures are depicted in Fig. 30. Despite its simplicity, the

72-residue model possesses  $72 \times 3 - 6 = 210$  degrees of freedom and incorporates the basic conformational complexity of a protein. Calmodulin itself is an ideal system for our study: It is a key signalling protein involved in many cellular processes (e.g., Ref. [5]), it is small, and it exhibits a particularly large structural rearrangement, see Sec. I.B.2

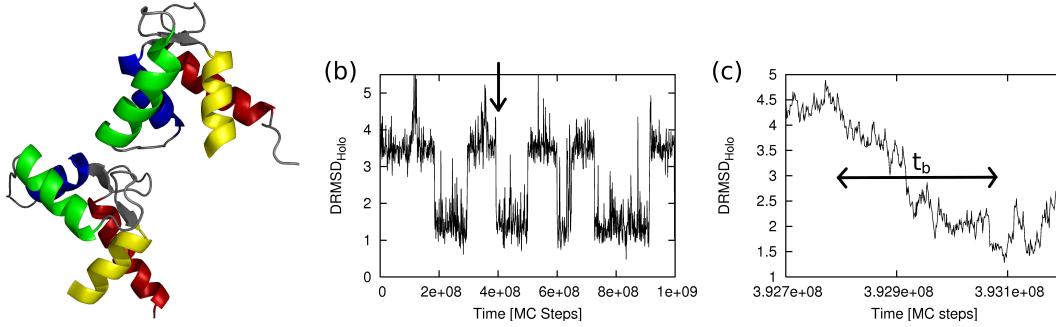


Figure 30: The N-terminal domain of calmodulin undergoes a large-scale structural change when it binds calcium. (a) The calcium-free Apo structure (1CFD) and the calcium-bound Holo structure (1CLL) are shown. (b) A sample trajectory from the simulation of the “double-native”  $G\bar{o}$  model of calmodulin exhibits several transition-events, one of which is detailed in (c). The approximate duration of the event  $t_b$  is indicated by the arrow.

We employ the “weighted ensemble” (WE) approach [63], see Sec. III.C.2, to generate an unbiased ensemble of paths for the calmodulin transition and, simultaneously, the reaction rate. Previously, WE sampling has been applied to study diffusion effects in binding [63, 80] and the folding of a simple protein model [83]. The WE method was chosen to investigate conformational transitions for three reasons. First, among path sampling algorithms, it is particularly elegant and straightforward to implement. Second, the WE method appears to be particularly well-suited for sampling multiple, structurally distinct pathways in a statistically correct way. (A comparative study in this regard is planned for future work.) Third, it yields both a path ensemble and the reaction rate from a single simulation. The WE method embodies a strategy of replicating success (“enrichment”), which had earlier been introduced in the construction of polymer configurations [86]; see also [87]. As illustrated in Fig. 13 in Sec. III.C.2, the strategy has three essential steps and maintains a rigorous statistical weighting throughout: (i) the initiation of multiple trajectories; (ii) replication of trajectories which

advance along a progress coordinate; and (iii) occasional pruning of low-weight trajectories. The pruning ensures manageable computational cost. Issues surrounding the selection of a progress coordinate — which need not be a reaction coordinate in the traditional sense — are discussed in detail below.

Our data show that WE path-sampling of calmodulin transitions provides excellent *quantitative agreement* with brute-force results, which include substantial pathway heterogeneity. Because the WE simulations consume a fraction of the brute-force simulation time, they appear to be a promising choice for the study of more realistic protein models.

## B. METHODS

### 1. Path sampling using the weighted ensemble (WE) approach.

The weighted ensemble path sampling approach has been explained carefully in sec. III.C.2. For our calmodulin simulations, the progress coordinate was chosen to be the negative of the “distance RMSD” (DRMSD) [168] to the Holo state.

Like the standard RMSD, the distance-RMSD (DRMSD) quantifies molecular distance measurement. Letting  $d_{ij}$  and  $d'_{ij}$  be the distances between residue  $i$  and  $j$  in two structures of the same molecule, which has  $N$  residues, then

$$\text{DRMSD} \equiv \sqrt{\frac{2}{N \times (N - 1)} \sum_{i < j} (d_{ij} - d'_{ij})^2}. \quad (\text{V.1})$$

(Sometimes the constant factor  $\sqrt{2}$  is removed in the definition.) DRMSD does not require alignment of two structures. For our united-residue model of calmodulin, it is faster to compute than RMSD and provides qualitatively similar information.

The simulation starts from the Apo state and progresses toward Holo. Fig. 31 shows the evolution of the probability in one weighted ensemble simulation of calmodulin.

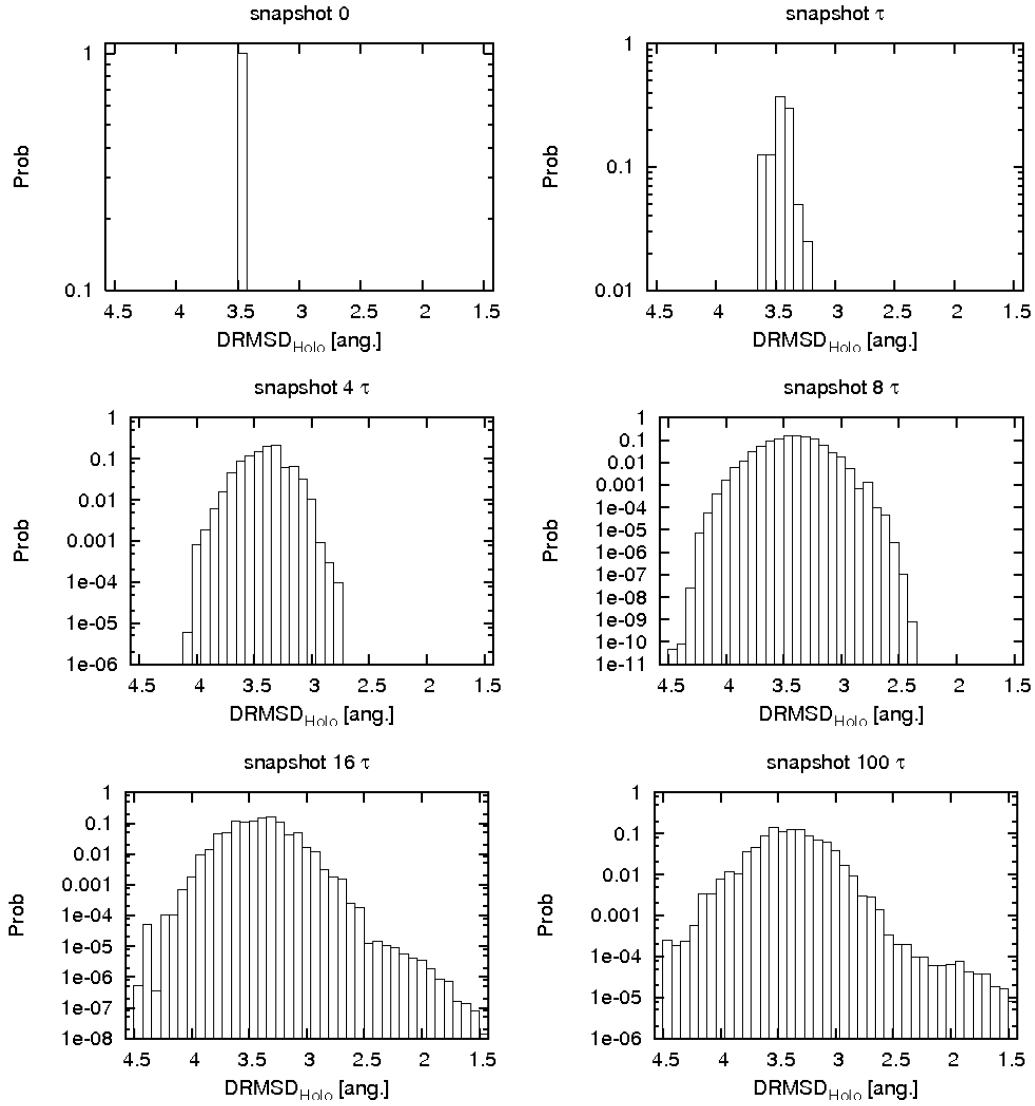


Figure 31: The time evolution of the probability distribution, which is shown at times 0,  $\tau$  (72000 MC steps),  $4\tau$ ,  $8\tau$ ,  $16\tau$  and  $100\tau$  based on Weighted Ensemble (WE) simulation of calmodulin. The simulations all start from the Apo state, located in the bins near  $\text{DRMSD}_{\text{Holo}} = 3.5\text{\AA}$ . After  $16\tau$ , some trajectories have climbed over the free energy barrier and arrived at the Holo state ( $\text{DRMSD}_{\text{Holo}} < 1.5\text{\AA}$ ). Notice the varying semi-log scale.

## 2. Bistable Gō model of united-residue calmodulin (N-terminal domain).

One of the authors previously designed a united-residue potential and associated software to enable brute-force generation of an ensemble of unbiased large-scale conformational transitions. Full details are given in Ref. [53]. As in the previous study, only the N-terminal domain (residues 4 - 75)<sup>1</sup> of calmodulin was studied [169]. Although a Gō model will not capture realistic biochemistry or detailed kinetics, it serves as an ideal system for testing algorithms. Further, the degree of activation can be tuned by lowering the temperature as we have done.

The united-residue “double-Gō” model [53] consists of alpha-carbon interaction centers with pairwise contact interactions as described below.

For a molecule with  $N$  residues, the total potential is the sum of  $N(N - 1)/2$  two-body potentials,

$$u^{\text{tot}} = \sum_{i=1}^N \sum_{j>i}^N u_{i,j}, \quad (\text{V.2})$$

where  $i$  and  $j$  label residues. The two-body potential is given by

$$u_{i,j} = \begin{cases} u_{i,j}^{\text{bond}} & \text{if } j = i + 1 \\ u_{i,j}^{\text{non-bond}} & \text{if } j > i + 1 \end{cases} \quad (\text{V.3})$$

When the  $i$ th and  $j$ th residues are sequential ( $j = i + 1$ ),  $u_{i,j}^{\text{bond}}$  accounts for the chain connectivity. A infinite well potential is constructed with reference to interresidue distance in the Apo (calcium-free) structure  $r_{i,i+1}^{\text{Apo}}$ , as shown in Fig. 32.

When the  $i$ th and  $j$ th residues are *not* sequential, their interaction potential  $u_{i,j}^{\text{non-bond}}$  is further classified into “non-native”, “single-native” and “double-native” depending on the distances found in the two native structures (1CFD and 1CLL). First we define a cut-off distance  $R_{\text{cut}}$ ; standard square-well (contact) interactions occur only below it, vanishing for  $r_{i,j} > R_{\text{cut}}$ .

(i) If  $r_{i,j}^{\text{Apo}} > R_{\text{cut}}$  and  $r_{i,j}^{\text{Holo}} > R_{\text{cut}}$ , the  $i$ th and  $j$ th residues are considered *non-native*.

The interaction potential is taken to consist of a forbidden region defined by a hard-core

---

<sup>1</sup>The first three residues in the Holo structure (1CLL) of calmodulin are not included in its protein data bank file.

radius found in the Apo (calcium-free) structure and a shoulder for the remaining part for  $r_{i,j} < R_{\text{cut}}$ . See panel (a) of Fig. 33.

(ii) If  $\min(r_{i,j}^{\text{Apo}}, r_{i,j}^{\text{Holo}}) < R_{\text{cut}}$  and  $\max(r_{i,j}^{\text{Apo}}, r_{i,j}^{\text{Holo}}) > R_{\text{cut}}$ , the pair is termed *single-native* - i.e, the pair of residues is sufficiently close in one of the two native structure. Their interaction is described by a square-well pair potential. The single well is centered near  $\min(r_{i,j}^{\text{Apo}}, r_{i,j}^{\text{Holo}})$ . See Fig. 33(b).

(iii) If  $r_{i,j}^{\text{Apo}} < R_{\text{cut}}$  and  $r_{i,j}^{\text{Holo}} < R_{\text{cut}}$ , the pair is considered *double-native*. Their interaction is described by two square wells centered near  $r_{i,j}^{\text{Apo}}$  and  $r_{i,j}^{\text{Holo}}$  respectively with a barrier between them. See panel (c) of Fig. 33.

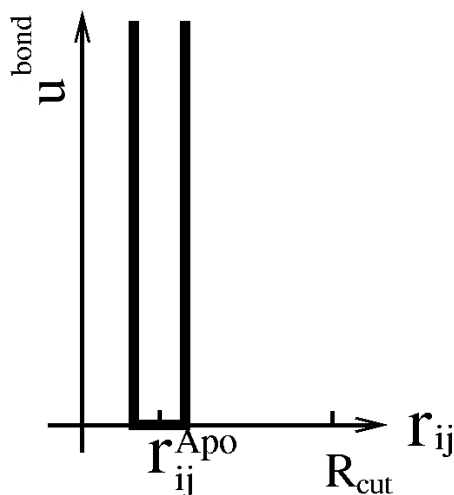


Figure 32: The potential of bonded interaction.

In summary, the double-native  $G\bar{o}$  potential stabilizes two native structures and creates a barrier between them. This is accomplished by the pairwise potentials shown in Fig. 33. The key double-well interactions occur between residues exhibiting two distinct distances in the two reference structures, as in Fig. 33(c). The potential guarantees that the two native structures (1CFD and 1CLL) have low total energies and that the transition between the two is possible. The potential is, of course, constructed using empirical information, and can be used with care in specific applications.

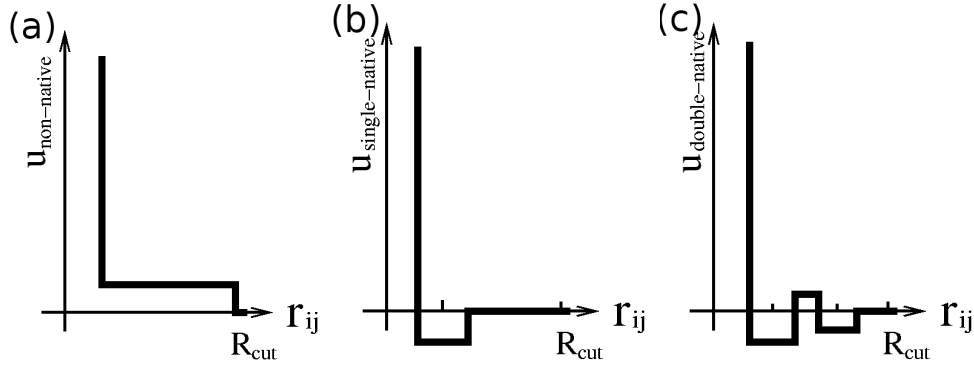


Figure 33: The non-native, single-native and double-native potentials.

See Ref. [53] for full details and for the parameters used in the simulation.

We employed “dynamical Monte Carlo” for the calmodulin model, i.e. Metropolis Monte Carlo employing only small, physically reasonable trial moves. This is a natural choice for any square-well potential; but further, when small trial steps are used, one can expect dynamical Monte Carlo to provide dynamics similar to over-damped Langevin dynamics [170, 171]. The reason is that, considering an energy landscape consisting of many barrier-separated basins, small-step dynamical Monte Carlo should cross barriers according to the standard Arrhenius factor without any unphysical, large jumps. In our simulations, the only trial move attempted was a single-particle translation of one grid-spacing ( $0.13\text{\AA}$ ) to a randomly chosen grid point among the 26 closest in the surrounding  $3 \times 3 \times 3$  cube.

Although neither the model nor the dynamics is fully accurate, the key point is that both our WE and brute-force simulations were performed with the identical computer code, ensuring a fair comparison in a tractable system.

### 3. Error analysis by block averaging.

The transition paths generated by the WE method are correlated, ruling out the use of simple statistical analyses. We therefore employed a standard statistical block-averaging approach based on [172], which is a reliable algorithm for calculating the statistical errors embodied in time-correlated data. In brief, one divides the sequence of data into  $n$  blocks and calculates

the standard deviation among the block averages,  $\sigma_n$ , for the quantity of interest. The length of blocks is continually increased until the quantity  $SE = \sigma_n/\sqrt{n}$  reaches a plateau, which indicates the blocks have become significantly longer than any correlation times and yields the effective standard error (i.e., scale of statistical uncertainty) of the estimate. All statistical uncertainties and error bars in figures are given as  $\pm 2SE$ .

## C. RESULTS

To validate the Weighted Ensemble (WE) method, we first considered the temperature  $k_B T/\epsilon = 0.5$  as in the previous study [53]. As a reference for comparison, brute-force simulations were run on several CPUs, yielding 373 independent transition-events from the Apo to Holo structure of our model of calmodulin. The total cost of these simulations is equivalent to  $\sim 18$  months of single-processor CPU time (Xeon, 3.2 GHz).

WE simulation, by contrast, required considerably less computer time, although identical code was used for running the embedded dynamical Monte Carlo. The WE simulation was run on a single CPU (Xeon, 3.2 GHz) for 4 weeks, yielding 33,576 correlated transitions. We made the simple choice of using the DRMSD distance [168] to the Holo state ( $\text{DRMSD}_{\text{Holo}}$ ) as the progress coordinate and cut this one-dimensional space into 40 bins, with  $M = 40$  simulations allowed in each bin. After every  $\tau = 72000$  Monte Carlo steps, the embedded brute-force simulations are paused, then combined and split without introducing bias, as described in Materials and Methods. See also Fig. 13.

### 1. Distribution of event durations

We first studied the distribution of transition-event durations  $\rho_b(t)$  [72, 123]. The duration of a transition-event is a short timescale characteristic of the reaction pathway itself (by contrast to the more common first-passage time). It is defined as the time elapsed from the last exit from the initial/reactant state until the first entry to final/product state. See Fig. 30. The distribution of these durations is the simplest quantitative measure of the

heterogeneity expected in the ensemble of transition-events. For conformational change in calmodulin, transition-event durations were calculated based on a reactant state defined such that  $\text{DRMSD}_{\text{Apo}} < 1.5\text{\AA}$  and the the product state by  $\text{DRMSD}_{\text{Holo}} < 1.5\text{\AA}$ .

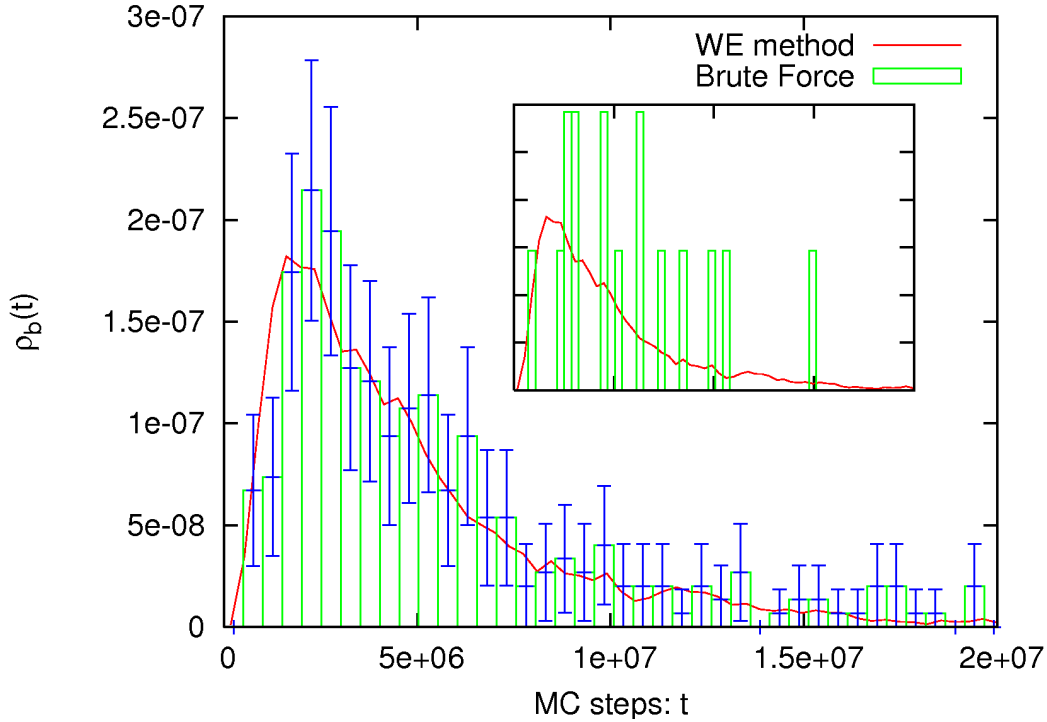


Figure 34: The distribution of transition-event durations  $\rho_b(t)$  from WE and brute-force simulations. In addition the error bars of the result from brute-force simulation are plotted. The event duration is the time interval between the last time a trajectory leaves the reactant state ( $\text{DRMSD}_{\text{Apo}} < 1.5\text{\AA}$ ) and the first time it reaches the product state ( $\text{DRMSD}_{\text{Holo}} < 1.5\text{\AA}$ ); see Fig. 30. The inset shows results from the two methods using equal amounts of CPU time,  $\sim 4$  weeks, which is not sufficient for brute-force simulation to obtain a good statistical distribution.

In Fig. 34 we show the WE simulation result for  $\rho_b(t)$  compared with that from brute-force simulation. They match well. The inset shows results from the two methods using equal quantities of CPU time. It is clear that WE method is more efficient than the brute-force simulation even at the relatively high temperature  $k_B T/\epsilon = 0.5$ .

## 2. The transition rate

For chemical and biological reactions and transitions, the reaction rate  $k$  is one of the most important quantities, and is impossible to obtain by brute-force simulation if the first-passage time is long [2]. Distinguished from other path-sampling methods, WE simulation not only yields the path ensemble, but also the reaction rate simultaneously. In WE simulation, after a transient period reflecting the finite event durations, the average current arriving to the product state (Holo) gives the transition rate. For  $k_B T/\epsilon = 0.5$ , we obtained  $k_{\text{WE}} = (1.9 \pm 0.4) \times 10^{-10}$  / MC step, which is in excellent agreement with the brute-force result,  $k_{\text{BF}} = (2.1 \pm 0.2) \times 10^{-10}$  /MC step.

## 3. Structural cross-sections of the path ensemble

We also compared structural properties of the path ensembles generated by the two methods, following the approach taken in previous work by Zuckerman [53]. Specifically, we examined the distributions of intermediate structures isolated along several “cross sections” of a two-dimensional reaction surface. The two coordinates of this surface — each a distance between residues located at the ends of helices — were chosen to assay heterogeneity in the path ensemble [53]. As shown in Fig 35(a), five cross-sectional “planes” were placed orthogonally to a straight line drawn between the two states. Histograms were made of the position, relative to the center line, at which each trajectory first crossed a given plane.

These cross-sectional histograms were produced by both simulation methods, and again compare favorably. They also demonstrate the *structural* heterogeneity in the path ensemble of this simple model system. Figure 35(b-e) shows the distributions, with the error bars representing approximately a 90% confidence interval. This sensitive structural analysis further underscores the accuracy of the WE method.

## 4. Efficiency

The previous results indicate the accuracy of the WE approach — i.e., that it properly corrects for bias as claimed. Nevertheless, the “bottom line” measure of a path-sampling

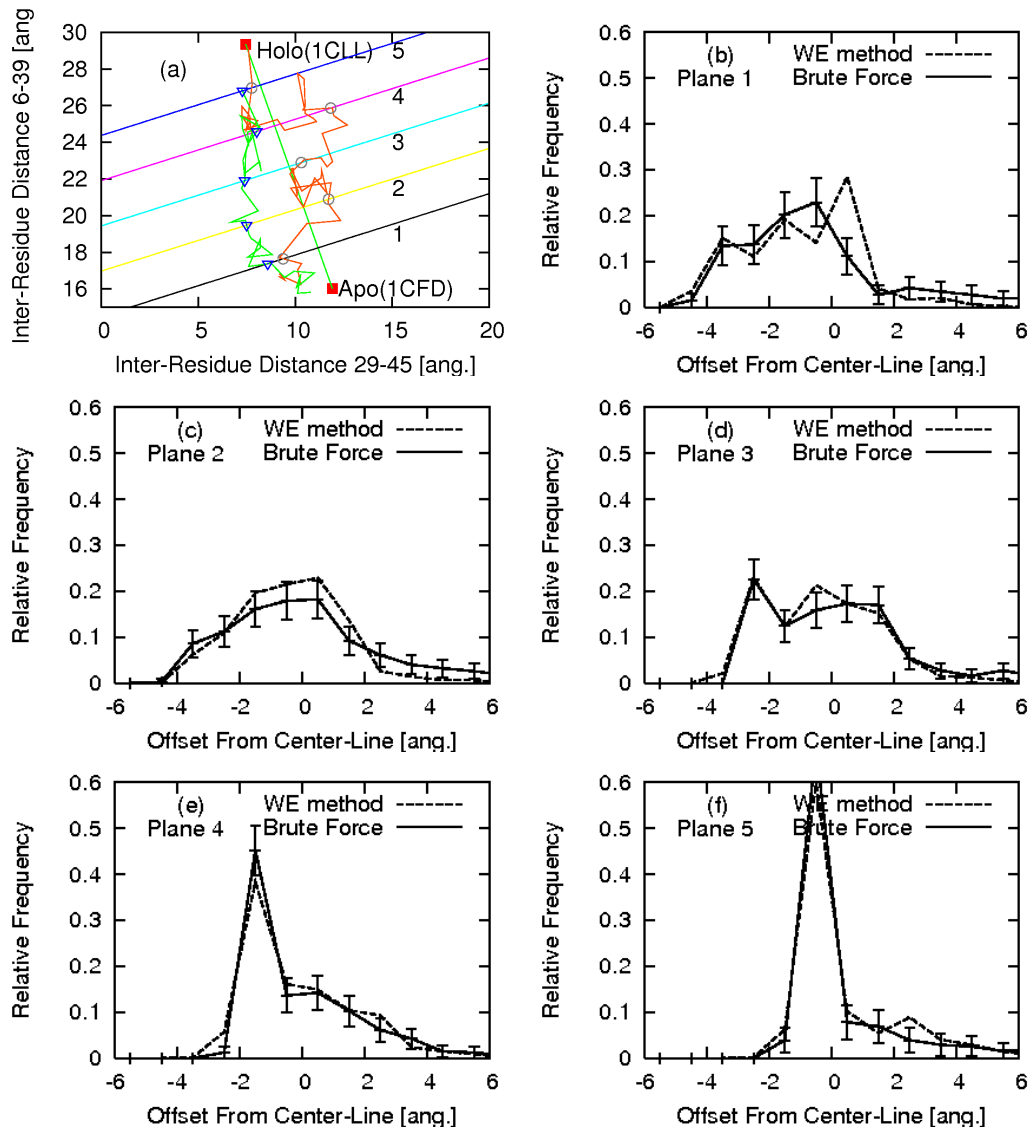


Figure 35: Structural distributions describing the heterogeneity of the path ensemble connecting the Apo and Holo states of calmodulin, based on both WE and brute-force simulations. Panel (a) shows two sample Apo  $\rightarrow$  Holo transitions, with open symbols indicating points at which the five parallel (dashed) “planes” are first crossed. The plots (b) - (e) show the ensemble-based distributions of the first crossing points of the paths on each of the five planes from (a).

approach is its efficiency, and especially its potential for efficiency in more chemically realistic and larger systems. We measured efficiency by calculating the ratio of single-processor CPU times required by WE and brute-force simulations to estimate the reaction rate with a given statistical precision. Similar results are found if the average event duration is used.

By studying a range of lower temperatures to assay the promise of WE simulation in more challenging systems, we found very encouraging results. First, for the temperature studied above ( $k_B T/\epsilon = 0.5$ ), we found a modest efficiency gain of somewhat more than a factor of five — that is, WE simulation requires less than one fifth the CPU expenditure for a given level of statistical precision. However, as the system becomes more difficult to simulate by brute-force simulation at lower values of  $k_B T/\epsilon$ , the WE approach becomes relatively more efficient. Equally importantly, the WE simulations require essentially the same overall amount of CPU time regardless of the temperature. For  $k_B T/\epsilon = 0.45$ , we found an efficiency gain of a factor of  $\sim 15$  and for  $k_B T/\epsilon = 0.4$ , it increased to  $\sim 100$ .

In greater detail, for  $k_B T/\epsilon = 0.45$  three weeks of WE simulation yielded 32,464 correlated transition trajectories, along with the estimate  $k_{\text{WE}} = (6.4 \pm 1.3) \times 10^{-11}$  /MC step. By contrast 30 *months* of brute-force simulation generated 172 trajectories and  $k_{\text{BF}} = (7.4 \pm 1.2) \times 10^{-11}$  /MC step. The distributions of event durations also agree very well. For  $k_B T/\epsilon = 0.4$ , the WE method gives the reaction rate  $k_{\text{WE}} = (8.4 \pm 1.8) \times 10^{-12}$  /(MC step) from three weeks of simulation, whereas brute-force simulation was too slow to yield even a single transition-event in the time we allotted to it. However, based on the reaction rate from WE simulation and the simple statistics of Poisson processes expected for brute-force simulation, the efficiency gain can be estimated as  $\sim 100$ . (We also confirmed that such estimation based on Poisson statistics reproduced the efficiency estimates of the higher temperatures.)

## 5. Use of a two-dimensional progress coordinate

To investigate whether the WE simulations for calmodulin were sensitive to the choice of progress coordinate — and also to explore potentially useful strategies for more complex systems — we investigated a two-dimensional progress coordinate. Specifically, we employed

two-dimensional bins where the first coordinate was the  $\text{DRMSD}_{\text{Holo}}$  distance as described in Materials and Methods, and the second coordinate was  $\text{DRMSD}_{\text{Apo}}$ . Our results were essentially indistinguishable from those based on a one-dimensional coordinate for the  $k_B T/\epsilon = 0.5$  condition we investigated.

Although using  $\text{DRMSD}_{\text{product}}$  as a single coordinate might be expected to be a fairly robust choice for many systems, generally one cannot expect a single dimension to be sufficient since there could be barriers transverse to the chosen coordinate [75] (i.e., free energy saddle points within a single bin). The Discussion, below, further probes this issue.

#### D. DISCUSSION: APPLYING WE TO MORE COMPLEX SYSTEMS

While WE simulation has proven highly successful in the present application of a simplified protein model, strategies for applying the approach robustly in more complex systems are important to consider. But before describing such strategies, it should be recognized that *the WE algorithm is statistically correct for sufficiently long simulations regardless of the choice of progress coordinate*. This can be seen heuristically by noting that, because the WE approach records statistical weights and does not use a biasing force or potential, unnatural transitions will only occur rarely and with very low weight. Each full transition trajectory is simply a concatenation of unbiased segments with proper statistical weights. Eventually, the important transition trajectories will occur and their weights will (correctly) dominate the results. In other words, the choice of coordinate(s) and binning should affect the *efficiency* of the weighted ensemble approach, but not its asymptotic correctness.

There are many possible strategies for using higher-dimensional binning while maintaining the overall number of bins at a practicable level. To be concrete, assume an initial one-dimensional progress coordinate, such as  $\text{DRMSD}_{\text{product}}$ , has already been divided into bins. Additional “sub-bins” can be added which will encourage transitions across possible saddles in the free energy landscape which may be orthogonal to the initial coordinate. For instance, the first bin (only) can be divided into sub-bins based on  $\text{DRMSD}_1$ , the distance from the starting structure in the first bin. Once a trajectory arrives in the second bin, a set

of sub-bins there can be defined based on  $\text{DRMSD}_2$ , the distance from the first configuration recorded in bin 2. By repeating this process, “transverse” sub-bins are always defined locally to maximize the chances for transverse motion with each bin.

Other strategies may also be useful. For instance, one could use just a single (“reactant”) structure and the corresponding  $\text{DRMSD}_{\text{reactant}}$  as an initial coordinate, along with orthogonal sub-bins defined on-the-fly, as above. In other words, one can let the simulation find the product state(s), see also Chapter VI and VII. Further, one can use bins of non-uniform sizes, possibly adjusted on-the-fly, or populate bins with different numbers of particles — and still maintain conformity with the statistical assumptions of the WE method.

The main point is that there is enormous flexibility to construct structurally suitable bins. We believe this flexibility will ultimately lead to robust strategies suitable for a wide range of biomolecular systems.

## E. CONCLUSIONS

We have applied the weighted ensemble (WE) approach of Huber and Kim [63] to the study of a protein conformational transition for the first time, and shown that it is a remarkably straightforward and successful approach. Because we employed a tractable united-residue model for a 72-residue domain of calmodulin [53], we verified the quantitative correctness of the results, by comparison to brute-force simulations. The WE results were also obtained in a fraction of the brute-force simulation time. To our knowledge, no previous path-sampling study of a nontrivial protein model performed such comparisons. Further, efficiency relative to brute-force simulation was found to increase dramatically as the system was made “difficult” by lowering the temperature, with minimal increase in absolute cost.

Although our model exhibits substantial heterogeneity in its transition-path ensemble, it remains an open and fundamental biochemical question as to whether real proteins are more precisely tuned. While proteins need to be robust — insensitive to many mutations — they are also precisely calibrated to their specific function. How is the balance achieved?

It is certainly premature to choose a single method as best for path sampling in biomolec-

ular systems, but the WE approach appears to be quite promising: (i) it estimates the reaction rate simultaneously with generating the transition path ensemble; (ii) it has the ability to sample heterogeneous pathways independently, avoiding trapping; and (iii) it is extremely easy to implement. Additionally, we have described a method which overcomes a potential weakness of the approach: effective, low-dimensional progress coordinates can be defined for any system in a simple, automated way that does not require any previous knowledge of the system beyond two structures of interest (or even just one). Of course, the ultimate proof will be in the future application to more difficult problems, but these initial, verified results in a non-trivial model mark the passing of a critical test. We also note that structurally diverse pathways determined via WE, possibly in simplified models, can be refined using transition path sampling [\[75\]](#).

## VI. TEST SYSTEMS WITH MULTIPLE CHANNELS

### A. INTRODUCTION

Because transitions are driven by thermal fluctuations, we expect to see some degree of variability among events. Transition paths can even go through different “channels”. Every channel is identified by a local minimum in the path space.

The transition path sampling approach (TPS), maybe the most popular path sampling method, described in Chapter III, could have a weakness as a Monte Carlo simulation in path space. It is possible for the Markov chain to be trapped in local minimum. In transition path sampling, because of the close similarity between the trial and old paths, it may be difficult to switch from one channel to another, and thereby sample all available channels. But for a weighted ensemble approach (WE), which describes the approximate solution of the Fokker-Planck equation, multiple channels should not be a problem.

Here we use these two methods to test systems with multiple channels for paths between local minimum positions in the free energy landscape. First we compare the weighted ensemble approach and the transition path sampling method by testing two-dimensional model potentials. Then we apply the weighted ensemble approach for the potential representing an alanine dipeptide molecule.

## B. COMPARISON OF TWO PATH SAMPLING METHODS

### 1. Potentials

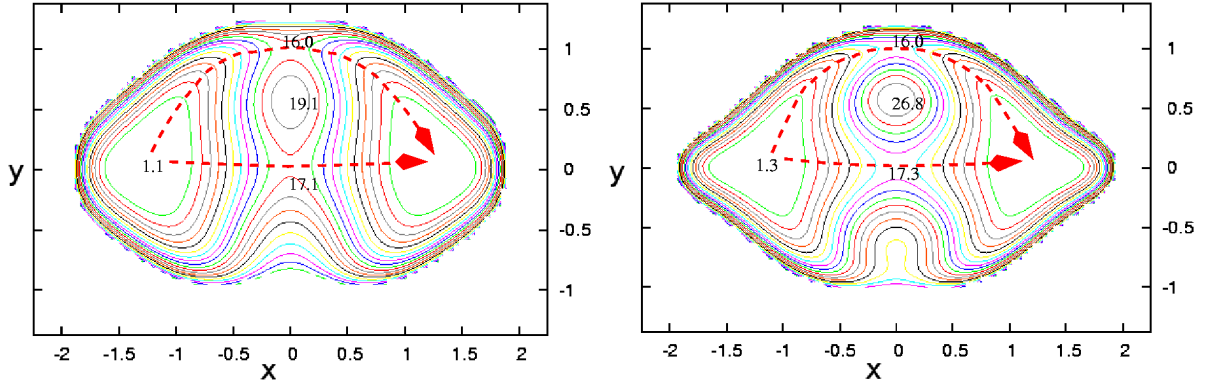


Figure 36: Contours of toy potentials. The left panel is the potential  $U_1^*$  with  $\alpha = 20$ , the right panel is the potential  $U_2^*$  with  $\alpha = 72$ .

We wanted to study low-dimensional but difficult potentials. The low dimensionality will permit full sampling for careful comparison of methods. However, two barrier-separated channels make the system challenging. Inspired by Chen, Nash and Horing’s work [173], we build up two toy potentials  $(k_B T)U_1^*$  and  $(k_B T)U_2^*$ , with

$$\begin{aligned}
 U^*(x, y) = & \alpha(x^2 + y^2 - 1)^2 \\
 & - \exp\{-4[(x - 1)^2 + y^2]\} - \exp\{-4[(x + 1)^2 + y^2]\} \\
 & + \exp[8(x - 1.5)] + \exp[-8(x + 1.5)] \\
 & + \exp[-4(y + 0.25)] + 16 \exp(-2x^2), \tag{VI.1}
 \end{aligned}$$

with  $\alpha = 20$  and  $\alpha = 72$  respectively distinguishing the two potentials.

The contours of these two potentials are shown in Fig. 36. Both potentials have two wells located near  $(\pm 1.2, 0.1)$ . In Fig. 37, the cross sections of these two potentials at  $x = 0$  are plotted. Two saddle points can be found in their cross sections. The barriers between saddle points separate the transition paths (from the left well to the right well) into channels. The

channels for motion along the passes are shown by red arrows in Fig. 36. The significant difference between these two potentials is the height of the barrier between the two saddle points.

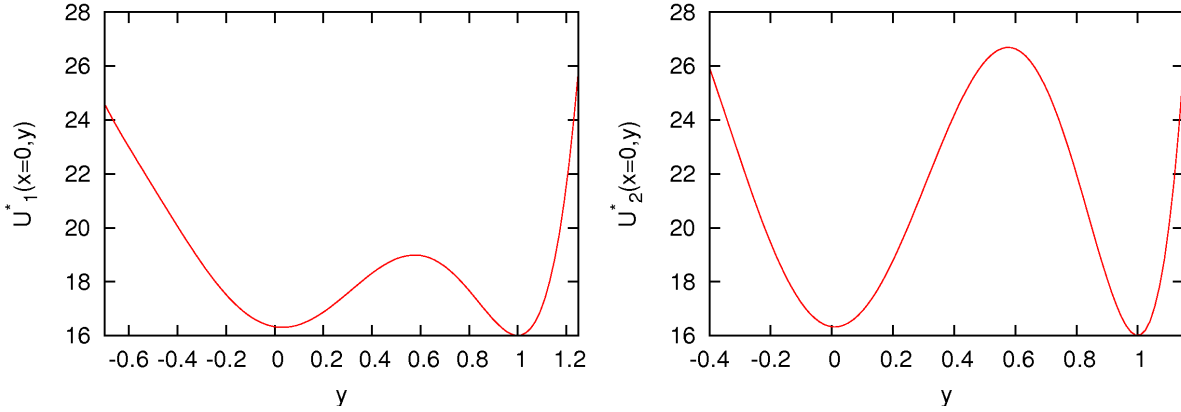


Figure 37: Cross sections at  $x = 0$  of the model potentials given by Eq.(VI.1). The left picture is the cross section of  $U_1^*$ , and the right picture is the cross section of  $U_2^*$ .

For the convenience of comparison, the important extreme points of these two potentials are listed in Table. 1.

	$U_1^*(\alpha = 20)$	$U_2^*(\alpha = 72)$
bottom of wells	$U_1^*(\pm 1.235, 0.162) = 1.085$	$U_2^*(\pm 1.231, 0.089) = 1.293$
saddle point 1	$U_1^*(0.000, 0.101) = 17.15$	$U_2^*(0.000, 0.036) = 17.33$
saddle point 2	$U_1^*(0.000, 1.001) = 16.03$	$U_2^*(0.000, 1.001) = 16.03$
top of the barrier	$U_1^*(0.000, 0.567) = 19.10$	$U_2^*(0.000, 0.575) = 26.80$

Table 1: The extreme points of the model potentials, including the bottom points of wells, saddle points and the top points of the barriers between saddle points.

## 2. Simulation results

### a. Path switching

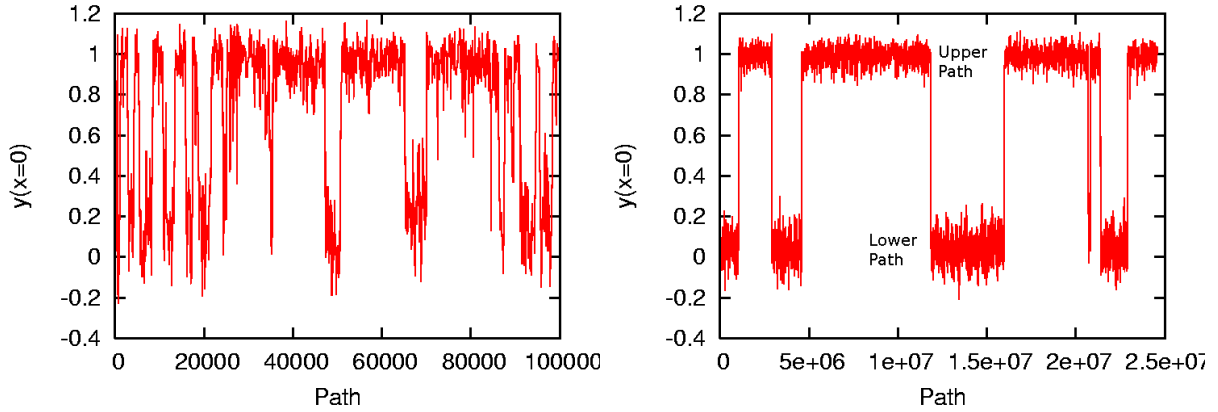


Figure 38: The transition path sampling (TPS) method switches between two types of paths, the left picture shows the path switch for potential  $U_1^*$ , the right picture shows the path switch for potential  $U_2^*$ .

The transition path sampling method is a Monte Carlo simulation in path space. We can monitor sampling effectiveness by studying the “speed” with which path space is sampled. The transition path sampling method switches between two types of paths seen in Fig. 36. To identify them, one can use the  $y$  position at the  $x = 0$  section on every path. Fig. 38 shows this position for each path versus the path index (Monte Carlo time). For potential  $U_1^*$ , the switch happens about every  $1.0e4$  paths, For potential  $U_2^*$ , because of the higher barrier, the switch happens approximately every  $5.0e6$  paths, which is much less frequent. This reveals how, for higher barriers, the sampling can get “trapped”, and for limited number of transition-events, could be biased.

Fig. 39 shows path switches in weighted ensemble simulations. The frequent switches suggest that the Weighted Ensemble method generates different types of paths simultaneously in both potentials. Because the weighted ensemble approach describes the approximate solution of the Fokker-Planck equation, the two channels become populated simultaneously.

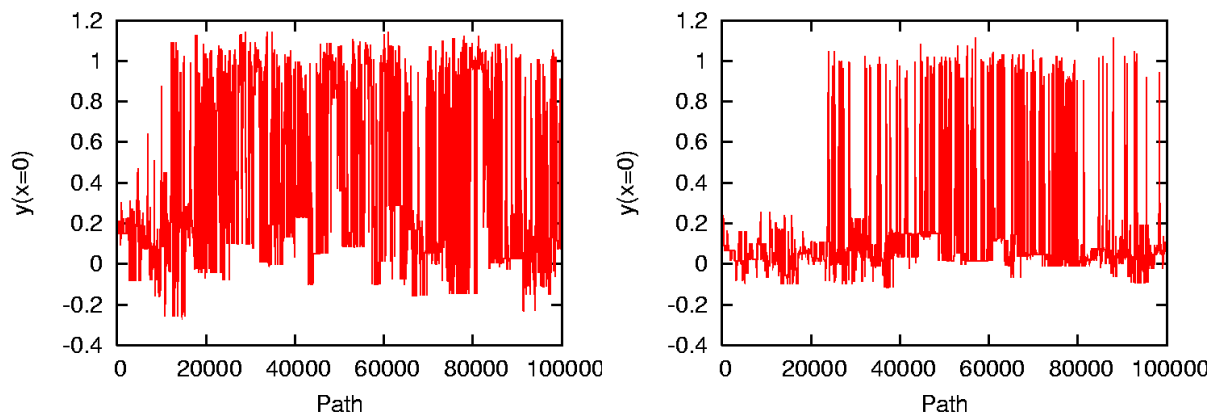


Figure 39: The weighted ensemble method switches between two types of paths, the left panel is for potential  $U_1^*$ , the right panel is for potential  $U_2^*$ .

### b. Distribution of transition-event duration

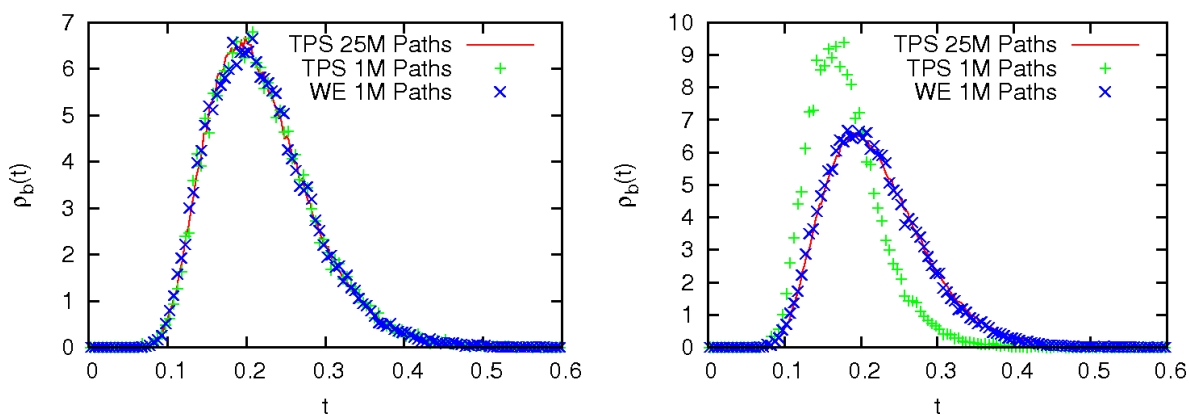


Figure 40: Distribution of transition-event durations. The left panel is for potential  $U_1^*$  (smaller barrier), the right panel is for potential  $U_2^*$  (larger barrier).

Fig. 40 shows the distributions of transition-event durations for these two model potentials, as estimated by both transition path sampling and weighted ensemble methods. Notice for potential  $U_2^*$ , because of the high barrier separating the two types of paths, a “short” transition path sampling simulation yields an incorrect distribution even after  $1.0e6$  paths

have been sampled. In that case, the transition path sampling is trapped by the local minimum in path space; see Fig. 38. But with the same number of paths, the weighted ensemble method gives the correct result.

## C. ALANINE DIPEPTIDE

### 1. Alanine dipeptide

The second system on which we will test the weighted ensemble approach is a small molecule called alanine dipeptide (ace-ala-nme). The molecule is shown in Fig. 41. The alanine dipeptide molecule is made of two peptide planes. In each plane, six atoms (three carbon atoms, one hydrogen, one oxygen atom and one nitrogen atom) are fairly rigid. The principle variables describing the structure of alanine dipeptide are two backbone dihedral angles:  $\Phi$  (C-N-C-C) and  $\Psi$  (N-C-C-N).

Alanine dipeptide is frequently used for testing simulation methods and force fields [174]. It is one of the simplest molecules which contains two full peptide planes. The dipeptide contains many structural features of protein backbones because proteins are polypeptide chains [175]. The carbon atom connecting two peptide planes is called alpha carbon ( $C_\alpha$ ). For proteins twenty different amino acid side chains are available to attach to the alpha carbon, and the alanine side chain in alanine dipeptide is one of them [175]. The methyl group connecting to the alpha carbon is a representative for most side chains (not good, however, for glycine and proline side chains). Furthermore alanine dipeptide is small enough that its free energy surface can be studied thoroughly by different approaches [174, 176–182]. The conformational transitions of alanine dipeptide contains multiple channels and have been studied by several groups recently [89, 102, 183].

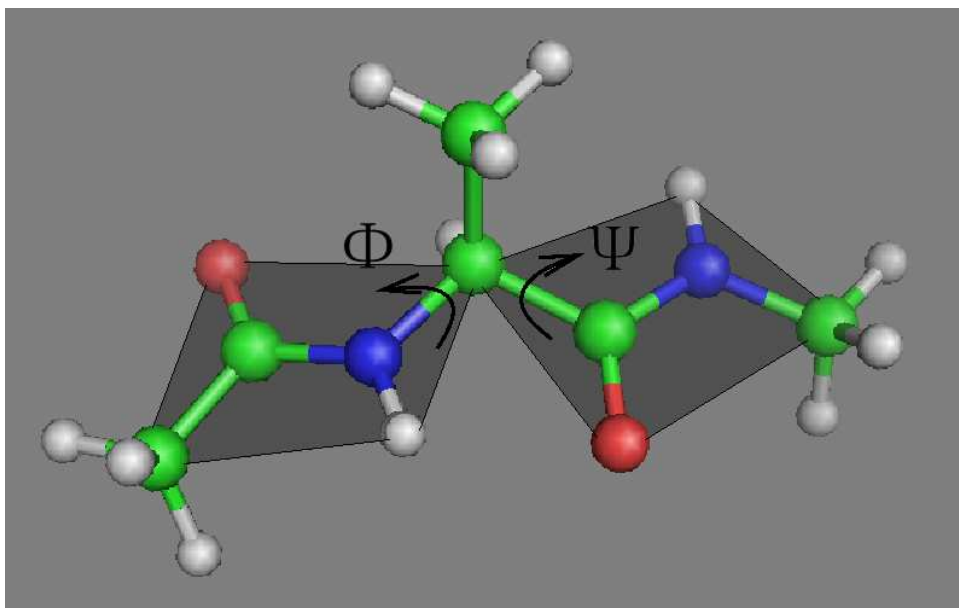


Figure 41: Alanine dipeptide molecule ( $\text{CH}_3\text{CO} - \text{Ala} - \text{NHCH}_3$ ). Different atoms are shown by different colors. White: Hydrogen; Red: Oxygen; Green: Carbon; Blue: Nitrogen. Alanine is one of the 20 proteinogenic amino acid. The side chain comes from alanine is a methyl group.

## 2. Simulation results and discussion

### a. Definition of transition path

First we checked the four energy minimum states of alanine dipeptide which will serve as the initial and final states of path sampling. These energy minimum states have been introduced by Apostolakis et al. [177]. Several brute force simulations were performed by using Langevin dynamics in the CHARMM program <sup>1</sup> [79]. The simulations used the “united atom model” with the CHARMM parameter set 19 and implicit solvent ACE (analytical continuum electrostatics) model [184]. Even for this small molecule, to obtain its free energy surface by brute force simulation on a single CPU will take several weeks. Because our purpose is not exploring its whole free energy surface, we just ran several short brute

<sup>1</sup>CHARMM (Chemistry at HARvard Macromolecular Mechanics) is a widely used molecular simulation program.

force simulations starting from different structures. So our results did not yield an equilibrium picture. But it is already good enough to show the four energy minima in Fig. 42. And by using the CHARMM program, the minima are found at  $(\Psi, \Phi)$ [Energy( $k_B T$ )] values  $\alpha_L(55.1, 46.4)[7.22]$ ,  $C_{7eq}(-77.9, 138.4)[0]$ ,  $\alpha_R(-75.6, -39.9)[1.78]$  and  $C_{7ax}(61.4, -71.4)[4.49]$  in the  $(\Psi, \Phi)$  dihedral plane, as shown in Fig. 42. Our locations and energy values of minima are somehow different with the previous study [102, 177, 181], but it is known that the simulation of alanine dipeptide is very sensitive to environments [88].

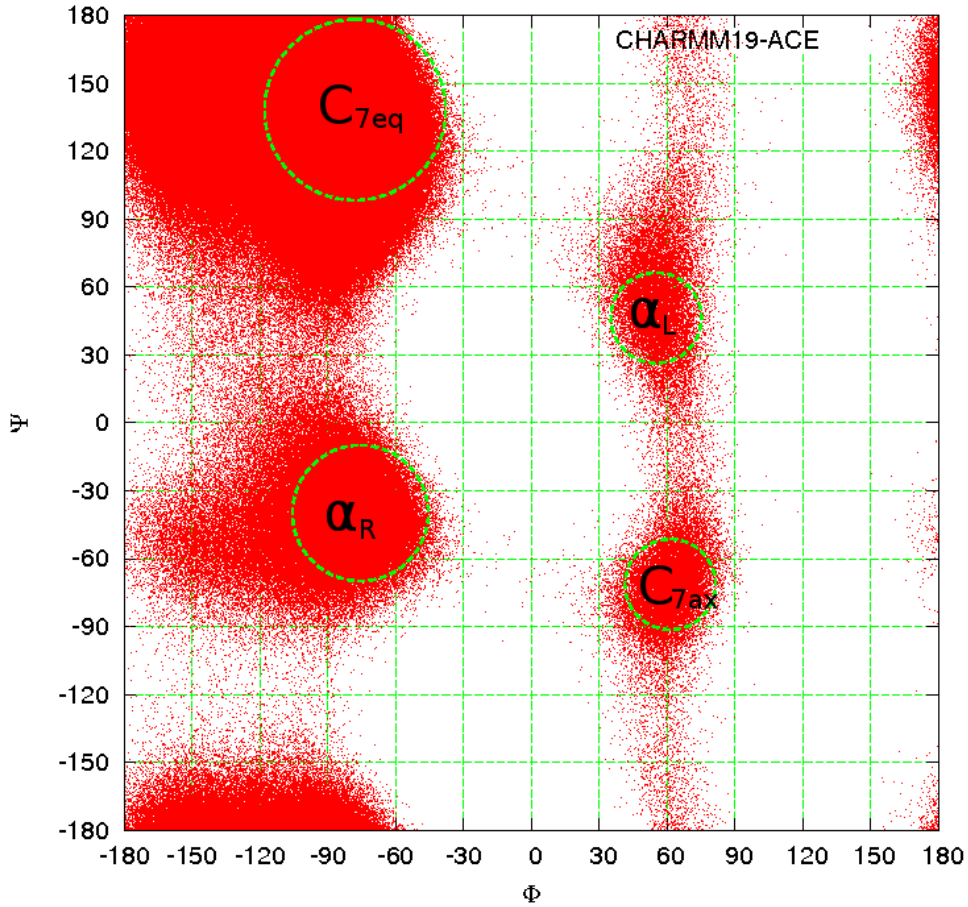


Figure 42: Four energy minima of alanine dipeptide.

Then we applied weighted ensemble approach to find the transition-events between state  $C_{7eq}$  and  $C_{7ax}$ . The initial state  $C_{7eq}$  is defined as the area closed by the circle

$$[\Psi - (-77.9)]^2 + [\Phi - (138.4)]^2 = (40)^2, \quad (\text{VI.2})$$

and the final state  $C_{7ax}$  is the area closed the circle

$$[\Psi - (61.4)]^2 + [\Phi - (-71.4)]^2 = (20)^2, \quad (\text{VI.3})$$

as shown in Fig. 42. According to calculations by other research groups [102, 177], the major barriers between these two states are higher than  $10k_B T$ . It will typically take days to find one transition path by brute force simulation.

### b. Paths in different channels

The weighted ensemble simulation was run on a single CPU (Xeon, 3.2Ghz) for 4 days, and yielded 43439 correlated transition paths. We chose the dihedral angles  $\Psi$  and  $\Phi$  as the progress coordinates and cut the two-dimensional space into a  $12 \times 12$  grid, with 20 simulations allowed in each grid (see Sec.III.C.2). After every  $\tau = 100\text{fs}$ , the embedded CHARMM simulations are paused, and the simulations are combined and split without bias, as discussed in the discussion of Sec.III.C.2. The weighted ensemble program was stopped after  $1000\tau$ .

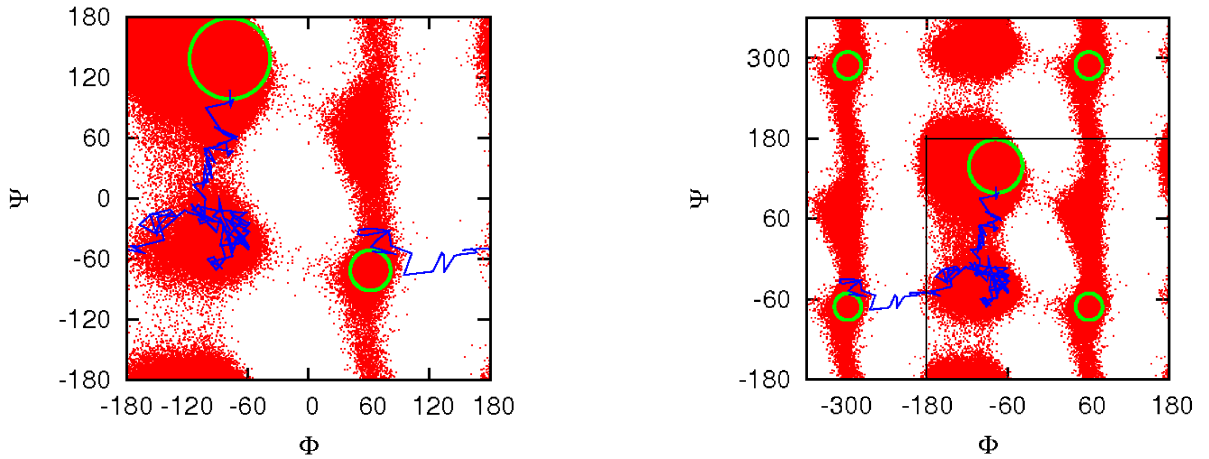


Figure 43: One path is plotted in the regular dihedral plane and an enlarged dihedral plane. In the right panel, the region of the regular dihedral plane is in the lower right square.

The paths will be studied in an enlarged dihedral plane, like the extended-zone scheme in solid state physics [185]. The reason of using an enlarged dihedral plane is that the path will be continuous in it. In the left panel of Fig. 43, a path is shown in the “first zone” of the dihedral plane. Because the dihedral plane is periodic, this path leaves the right border of the dihedral plane and re-enters from the left border. In the right panel of Fig. 43, the four closest final states  $C_{7ax}$  (one in the first zone and three images) around the initial state  $C_{7eq}$  are included. Now the path is continuous and it is clear that it leads to the lower left  $C_{7ax}$  state (image).

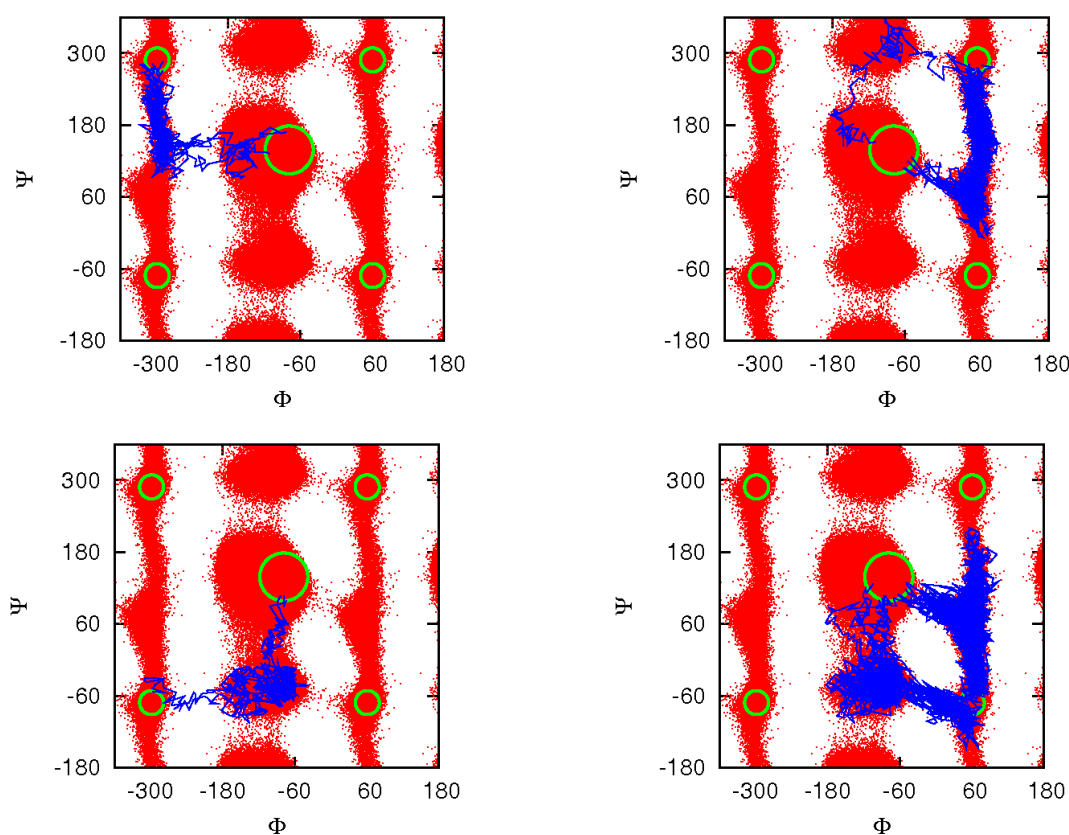


Figure 44: Four types of transition paths between states  $C_{7eq}$  and  $C_{7ax}$ .

The transition paths can be roughly divided into four types according to which  $C_{7ax}$  state they end in this extended dihedral plane. These four types of paths correspond to the combinations of clockwise and anticlockwise rotational directions of dihedral angles  $\Psi$  and  $\Phi$ . Different types of paths pass different barriers; therefore they belong to different channels.

Approximately 100 paths randomly chosen (based on their weights) are plotted in Fig. 44. The distributions of these four types of paths are listed in Table 2.

$C_{7ax}$ position	upper left	upper right	lower left	lower right
Distribution	5.9%	13.8%	0.7%	79.6%

Table 2: The distributions of four types of transition paths between states  $C_{7eq}$  and  $C_{7ax}$ .

There are multiple channels for each of the four types of paths. Among all these paths, 79.6% of them connect states  $C_{7eq}$  and the lower right  $C_{7ax}$ . Most of those go through two channels; 41.9% of all the paths pass state  $\alpha_L$  in the middle and 37.7% pass state  $\alpha_R$ , as shown in Fig. 45.

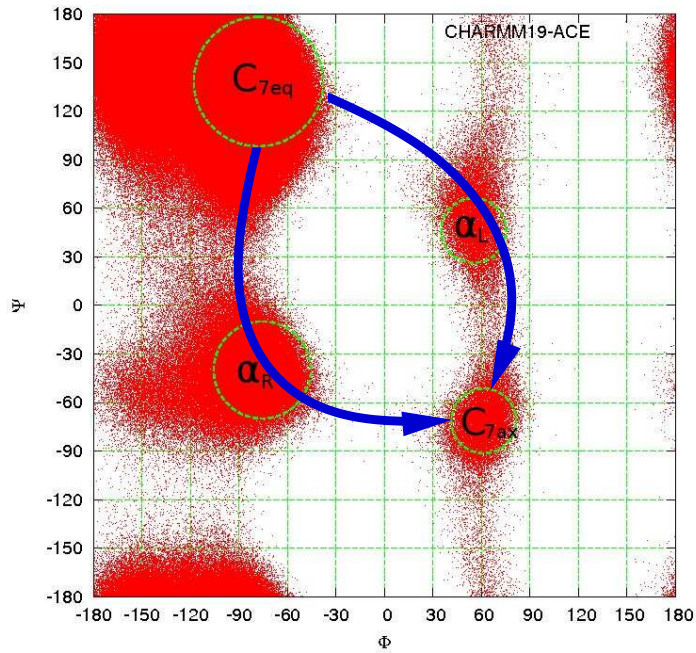


Figure 45: Two channels of transition-events between states  $C_{7eq}$  and lower right  $C_{7ax}$ .

### c. Intermediate stable states in the middle of path

For the weighted ensemble simulations, the total time  $n\tau$  should be long enough so that all

the possible paths will be sampled well if intermediate metastable states exist. The transition-events found in alanine dipeptide's conformational change can be divided into several small transition parts and metastable states. The simplest case has one intermediate metastable state in the transition path, if we consider just one of the two channels in Fig. 45. Then the total duration of the whole transition-event is

$$t_b = t_1 + t_2 + t_3, \quad (\text{VI.4})$$

where  $t_1$  is the duration of the transition-event between the initial and intermediate states,  $t_2$  is the time that the simulation spends in the intermediate state before it goes to the final state, and  $t_3$  is the duration of the transition between the intermediate and final states. Because the transition-events are fast events, and  $t_2$  is the waiting time in a metastable state, we expect their averages will satisfy

$$\begin{aligned} \langle t_2 \rangle &\gg \langle t_1 \rangle \\ \langle t_2 \rangle &\gg \langle t_3 \rangle. \end{aligned} \quad (\text{VI.5})$$

If the distributions of these three time intervals are  $\rho_1(t_1)$ ,  $\rho_2(t_2)$  and  $\rho_3(t_3)$ , the distribution of the total duration  $t_b$  can be written as a simple convolution

$$\rho(t_b) = \int_0^{t_b-t_1} dt_3 \int_0^{t_b} dt_1 \rho_1(t_1) \rho_3(t_3) \rho_2(t_b - t_1 - t_3). \quad (\text{VI.6})$$

When  $t_b \gg \langle t_1 \rangle$  and  $t_b \gg \langle t_3 \rangle$ , Eq.(VI.6) can be approximated

$$\begin{aligned} \rho(t_b) &= \int_0^{t_b-t_1} dt_3 \int_0^{t_b} dt_1 \rho_1(t_1) \rho_3(t_3) \rho_2(t_b - t_1 - t_3) \\ &\approx \left( \int_0^{t_b} \rho_3(t_3) dt_3 \right) \left( \int_0^{t_b} \rho_1(t_1) dt_1 \right) \rho_2(t_b) \\ &= \rho_2(t_b). \end{aligned} \quad (\text{VI.7})$$

The scale of averages  $\langle t_2 \rangle$  and  $\langle t_b \rangle$  will be of the same order. Then for the weighted ensemble simulations, the total time  $n\tau$  should be much longer than  $\langle t_2 \rangle$  so that all the possible paths will be sampled well. From our experience, we expect  $n\tau \sim 10\langle t_2 \rangle$  will yield good results. However, if what happens during  $t_2$  is not interesting, (for example, only the transition part of path is of interest,) a simulation with  $n\tau \gg (t_1 + t_3)$  will be sufficient to give transition

path ensembles for the first and third parts, the actual transition-events. The two reaction rates also can be found by the weighted ensemble methods in a timescale much shorter than the average waiting times, as we discussed in Sec.II.E.1 and Sec.III.C.2. A good discussion about consecutive reaction rate can be found in Atkins and Paula’s book [186].

The intermediate stable states in the middle of path will decrease the efficiency of the transition path sampling method, specially when the shooting algorithm, mentioned in Sec.III.C.1, is used to generate new paths. The simulation will stay in the intermediate state for a long time before it finds a trial transition path.

## D. CONCLUSIONS

In this chapter, we first used two-dimensional model potentials to show that the weighted ensemble approach has an advantage in finding multiple channels of paths compared with the transition path sampling method. It is shown that the transition path sampling approach, which is a Monte Carlo simulation in the path space, is possible to be trapped in the local minimum. However the weighted ensemble approach sampled multiple channels of paths successfully.

Then the weighted ensemble method was applied to the alanine dipeptide molecule to find all possible paths between two stable structures. The weighted ensemble approach found multiple channels of paths and gave the probability distributions of different channels in one simulation. Furthermore, it also got the information on reaction rates for these channels. These kinds of results have not been previously obtained by any other path sampling method even for this small molecule. Our simulation exhibits the weighted ensemble method’s distinguishing ability of complete path sampling for systems with multiple channels.

## VII. CONCLUSION AND OUTLOOK

### A. WHAT HAS BEEN ACCOMPLISHED

This thesis describes the study of the distribution of the durations of transition-events in one-dimensional systems, and the applications of the weighted ensemble path sampling approach for a variety of toy and molecular system.

We applied a combination of analytic and numerical techniques to study the distribution,  $\rho_b(t)$ , of the durations of transition-events over a barrier in a one-dimensional system undergoing over-damped Langevin dynamics. A number of results were obtained, including a recursive formulation for calculating all moments of  $\rho_b$  based solely on the potential function, and the properties of the short-time and long-time behavior of  $\rho_b$ . These analytical results of one-dimensional systems can provide a valuable theoretical reference point for future comparisons to molecular studies.

We applied the weighted ensemble (WE) approach of Huber and Kim [63] to the study of a protein conformational transition. We employed a tractable united-residue model for a 72-residue domain of calmodulin [53], which, nevertheless involves over 200 degrees of freedom, and verified the quantitative correctness of the results, by comparison to brute-force simulations. The comparison indicates that the WE approach quantitatively reproduces the brute-force results, as assessed by considering: (i) the reaction rate; (ii) the distribution of event durations; and (iii) structural distributions describing the heterogeneity of the paths. Our results suggest that the WE method can increase efficiency by orders of magnitude in more challenging systems.

We applied the weighted ensemble approach and transition path sampling method to test systems with multiple channels for paths. First we compared these two methods by sampling

paths in two-dimensional model potentials. It was shown that the transition path sampling method is susceptible “trapping” in the local minimum as a Monte Carlo approach in path space. But the weighted ensemble approach sampled multiple channels of paths successfully. Then the weighted ensemble approach was applied for the potential representing an alanine dipeptide molecule. It found multiple channels of paths and gave the probability distributions for different channels in one simulation, which has never been accomplished, to the author’s knowledge, by other path sampling methods.

## B. WHAT WILL BE ACCOMPLISHED

### 1. Distribution of the durations of transition-events

Can the results of the distribution of the durations of transition-events in one-dimensional spaces be generalized to high-dimensional space and applied to large biological systems? Some exciting comparable work has been done by Zwanzig [187]. Under certain conditions, a high-dimensional Fokker-Planck equation is projected into a one-dimensional Smoluchowski equation in Zwanzig’s study on diffusion past an “entropy barrier”. It may be possible to follow his idea and generalize our results beyond one-dimensional space.

### 2. Weighted ensemble approach

We plan to apply the weighted ensemble approach to a more realistic model of a larger protein. For example, the motor protein myosin [3, 6] is one good candidate. Path sampling on a large biological system requires considerably more computational power than what has been used in this thesis. One available solution is parallel computation. If we check the procedure discussed in Sec.III.C.2, it seems that parallel computation is very suitable for the weighted ensemble approach, especially in steps III and IV. If the problem of interest is still beyond our reach even when parallel computation is applied, a coarse grained model for simulation will be considered.

The weighted ensemble approach has the ability to find the stable states of the system by

itself, i.e., they don't have to be known in advance. As we mentioned before, when the dynamics of the system can be treated as over-damped Brownian motion, the WE approach can work as a discrete unbiased picture of forward integration of the Fokker-Planck equation. Then the trajectories in the weighted ensemble approach will arrive at every stable state without knowing them before hand. In fact, the results on alanine dipeptide in Sec. VI.C is an example. Further, compared with the simulation for calmodulin in Chapter V, when we changed the progress coordinate to the DRMSD to the initial state (Apo state), the weighted ensemble approach found the final state (Holo state) without problem (results not shown). These simulation results are extremely encouraging.

Now we are developing an improved weighted ensemble method which does not require choosing a progress coordinate at the outset. One drawback of WE and several other path sampling methods is the requirement of a predetermined reaction coordinate or progress coordinate. Based on the relationship of this approach and the Fokker-Planck equation, we realized that there exists more freedom to define the "bins" in the weighted ensemble method, and the predetermined progress coordinate is not necessary. We already succeeded in demonstrating the new "knowledge-free" approach in low-dimensional space (results not shown). The improved weighted ensemble method in high-dimensional space is under development.

## BIBLIOGRAPHY

- [1] D. Frenkel and B. Smit, *Understanding Molecular Simulation: From Algorithms to Applications*, 2nd ed. (Academic Pr, 2001).
- [2] P. Hnggi, P. Talkner, and M. Borkovec, *Rev. Mod. Phys.* **62**, 251 (1990).
- [3] B. Alberts *et al.*, *Essential Cell Biology*, 2nd ed. (Garland Science/Taylor & Francis Group, 2003).
- [4] J. M. Berg, L. Stryer, and J. L. Tymoczko, *Biochemistry*, 5th ed. (W. H. Freeman, 2002).
- [5] D. Chin and A. R. Means, *Trends Cell Biol.* **10**, 322 (2000).
- [6] C. K. Mathews, K. E. van Holde, and K. G. Ahern, *Biochemistry* (Prentice Hall, 1999).
- [7] C. Gardiner, *Handbook of stochastic methods for physics, chemistry, and the natural sciences*, 2nd ed. (Springer-Verlag, 1994).
- [8] H. Risken, *Fokker-Planck Equation: Methods of Solution and Applications*, 2nd ed. (Springer-Verlag, 1989).
- [9] N. G. van Kampen, *Stochastic Processes in Physics and Chemistry* (North Holland, 1992).
- [10] R. M. Mazo, *Brownian Motion: Flucuations, Dynamics, and Applications* (Oxford University Press, USA, 2002).
- [11] R. Zwanzig, *Nonequilibrium Statistical Mechanics*, 1st ed. (Oxford University Press, USA, 2001).
- [12] F. Wiegul, *Introduction to Path-integral Methods in Physics and Polymer Science*, 1st ed. (World Scientific Publishing Co Pre Ltd, 1986).
- [13] L. S. Schulman, *Techniques and Applications of Path Integration*, 1st ed. (John Wiley & Sons Inc, 1981).
- [14] A. Einstein, *Ann. Phys.* **17**, 549 (1905).

- [15] M. v. Smoluchowski, *Ann. Phys.* **21**, 756780 (1906).
- [16] H. C. Berg, *Random Walks in Biology*, 1st ed. (Princeton Univ Pr, 1993).
- [17] S. E. Shreve, *Stochastic Calculus for Finance I: The Binomial Asset Pricing Model*, 1st ed. (Springer, 2005).
- [18] S. E. Shreve, *Stochastic Calculus for Finance II: Continuous-Time Models*, 1st ed. (Springer, 2004).
- [19] P. Langevin, *C. R. Hebd. Seances Acad Sci.* **146**, 530533 (1908).
- [20] D. Lemons and A. Gythiel, *Am. J. Phys.* **65**, 1079 (1997).
- [21] H. Kleinert, *Path Integrals in Quantum Mechanics, Statistics, and Polymer Physics, and Financial Markets*, 3rd ed. (World Scientific Pub Co Inc, 2004).
- [22] E. H. Lieb and D. C. Mattis, *Mathematical Physics in One Dimension: Exactly Soluble Models of Interacting Particles*, 1st ed. (Academic Pr, 1966).
- [23] E. M. Lifshitz and L. D. Landau, *Course of Theoretical Physics : Mechanics*, 3rd ed. (Butterworth-Heinemann, 1982).
- [24] M. Tenenbaum and H. Pollard, *Ordinary Differential Equations*, 1st ed. (Dover Publications, 1985).
- [25] F. W. Wiegel, *Physica* **37**, 105 (1967).
- [26] M. Bulmer, *Principles of Statistics* (Dover Publications, 1979).
- [27] J. Tweet, S. Williams, and M. Cook, *Dungeons & Dragons Core Rulebook Set*, 1st ed. (Wizards of the Coast, 2003).
- [28] A. Leach, *Molecular Modelling: Principles and Applications*, 2nd ed. (Prentice Hall, 2001).
- [29] T. Schlick, *Molecular Modeling and Simulation*, 1st ed. (Springer, 2002).
- [30] H. Gould and J. Tobochnik, *An Introduction to Computer Simulation Methods: Applications to Physical System*, 2nd ed. (Addison Wesley, 1995).
- [31] D. M. Zuckerman and T. B. Woolf, *J. Chem. Phys.* **111**, 9475 (1999).
- [32] R. Elber, *Curr. Opin. Struct. Biol.* **15**, 151 (2005).
- [33] J. Evenas, S. Forsen, A. Malmendal, and M. Akke, *J. Mol. Biol.* **289**, 603 (1999).
- [34] K. A. Dill *et al.*, *Protein Sci.* **4**, 561 (1995).
- [35] H. S. Chan and K. A. Dill, *Proteins Struct. Funct. Genet.* **30**, 2 (1998).

- [36] J.-E. Shea and C. L. Brooks III, *Annu. Rev. Phys. Chem.* **52**, 499 (2001).
- [37] J. N. Onuchic and P. G. Wolynes, *Curr. Opin. Struct. Biol.* **14**, 70 (2004).
- [38] M. Levitt and A. Warshel, *Nature* **253**, 694 (1975).
- [39] Y. Zhou and M. Karplus, *Proc. Natl. Acad. Sci. USA* **94**, 14429 (1997).
- [40] N. Go and H. Taketomi, *Proc. Natl. Acad. Sci. USA* **75**, 559 (1978).
- [41] A. Kolinski and J. Skolnick, *Lattice Models of Protein Folding, Dynamics and Thermodynamics*, 1st ed. (Chapman & Hall, 1996).
- [42] K. F. Lau and K. A. Dill, *Macromolecules* **22**, 3986 (1989).
- [43] A. Liwo *et al.*, *J. Comput. Chem.* **18**, 849 (1997).
- [44] A. Liwo *et al.*, *J. Comput. Chem.* **18**, 874 (1997).
- [45] A. Liwo *et al.*, *J. Comput. Chem.* **19**, 259 (1998).
- [46] I. Bahar, A. R. Atilgan, and B. Erman, *Fold. Des.* **2**, 173 (1997).
- [47] T. Haliloglu, I. Bahar, and B. Erman, *Phys. Rev. Lett.* **79**, 3090 (1997).
- [48] I. Bahar, B. Erman, R. L. Jernigan, A. R. Atilgan, and D. G. Covell, *J. Mol. Biol.* **285**, 1023 (1999).
- [49] L.-W. Yang *et al.*, *Bioinformatics* **21**, 2978 (2005).
- [50] C. Clementi, P. A. Jennings, and J. N. Onuchic, *Proc. Natl. Acad. Sci. USA* **97**, 5871 (2000).
- [51] P. Gupta, C. K. Hall, and A. C. Voegler, *Protein Sci.* **7**, 2642 (1998).
- [52] A. V. Smith and C. K. Hall, *J. Mol. Biol.* **312**, 187 (2001).
- [53] D. M. Zuckerman, *J. Phys. Chem. B* **108**, 5127 (2004).
- [54] E. Lyman, F. M. Ytreberg, and D. M. Zuckerman, *Phys. Rev. Lett.* **96**, 028105 (2006).
- [55] E. Lyman and D. Zuckerman, *J. Chem. Theory Comput.* **2**, 656 (2006).
- [56] S. B. Ozkan, K. A. Dill, and I. Bahar, *Biopolymers* **68**, 35 (2003).
- [57] N. Singhal and V. S. Pande, *J. Chem. Phys.* **123**, 204909 (2005).
- [58] I. V. Gopich and A. Szabo, *Chem. Phys.* **284**, 91 (2002).
- [59] L. R. Pratt, *J. Chem. Phys.* **85**, 5045 (1986).

- [60] A. K. Faradjian and R. Elber, *J. Chem. Phys.* **120**, 10880 (2004).
- [61] R. Elber, J. Meller, and R. Olender, *J. Phys. Chem. B* **103**, 899 (1999).
- [62] H. C. Ottinger, *Macromolecules* **27**, 3415 (1994).
- [63] G. A. Huber and S. Kim, *Biophys. J.* **70**, 97 (1996).
- [64] P. G. Bolhuis, D. Chandler, C. Dellago, and P. L. Geissler, *Annu. Rev. Phys. Chem.* **53**, 291 (2002).
- [65] P. G. Bolhuis, *Proc. Natl. Acad. Sci. USA* **100**, 12129 (2003).
- [66] R. Radhakrishnan, T. Schlick, and C. R. Cantor, *Proc. Natl. Acad. Sci. USA* **101**, 5970 (2004).
- [67] D. M. Zuckerman and T. B. Woolf, *Phys. Rev. E* **63**, 016702 (2000).
- [68] R. J. Allen, D. Frenkel, and P. R. ten Wolde, *J. Chem. Phys.* **124**, 024102 (2006).
- [69] W. Ren, E. Vanden-Eijnden, P. Maragakis, and W. E., *J. Chem. Phys.* **123**, 134109 (2005).
- [70] A. Mossa and C. Clementi, *Phys. Rev. E* **75**, 046707 (2007).
- [71] R. Crehuet and M. Field, *J. Phys. Chem. B* **111**, 5708 (2007).
- [72] D. M. Zuckerman and T. B. Woolf, *J. Chem. Phys.* **116**, 2586 (2002).
- [73] E. L. Pollock and D. M. Ceperley, *Phys. Rev. B* **30**, 2555 (1984).
- [74] D. M. Ceperley and E. L. Pollock, *Phys. Rev. Lett.* **56**, 351 (1986).
- [75] C. Dellago, P. G. Bolhuis, F. S. Csajka, and D. Chandler, *J. Chem. Phys.* **108**, 1964 (1998).
- [76] C. Dellago, P. G. Bolhuis, and D. Chandler, *J. Chem. Phys.* **108**, 9236 (1998).
- [77] M. F. Zimmer, *Phys. Rev. Lett.* **75**, 1431 (1995).
- [78] M. Paniconi and M. F. Zimmer, *Phys. Rev. E* **59**, 1563 (1999).
- [79] B. R. Brooks *et al.*, *J. Comput. Chem.* **4**, 187 (1983).
- [80] A. Rojnuckarin, D. R. Livesay, and S. Subramaniam, *Biophys. J.* **79**, 686 (2000).
- [81] E. W. Fisher, A. Rojnuckarin, and S. Kim, *J. Mol. Struct.: THEOCHEM* **529**, 183 (2000).
- [82] E. W. Fisher, A. Rojnuckarin, and S. Kim, *Struct. Chem.* **13**, 193 (2002).

- [83] A. Rojnuckarin, S. Kim, and S. Subramaniam, Proc. Natl. Acad. Sci. USA **95**, 4288 (1998).
- [84] G. A. Huber and J. A. McCammon, Phys. Rev. E **55**, 4822 (1997).
- [85] B. W. Zhang, D. Jasnow, and D. M. Zuckerman, Proc. Natl. Acad. Sci. USA **104**, 18043 (2007).
- [86] F. T. Wall and J. J. Erpenbeck, J. Chem. Phys. **30**, 634 (1959).
- [87] P. Grassberger, Phys. Rev. E **56**, 3682 (1997).
- [88] T. B. Woolf, Chem. Phys. Lett. **289**, 433 (1998).
- [89] H. Jang and T. B. Woolf, J. Comput. Chem. **27**, 1136 (2006).
- [90] W. H. Press, B. P. Flannery, S. A. Teukolsky, and W. T. Vetterling, *Numerical Recipes in C: The Art of Scientific Computing* (Cambridge University Press, 1992).
- [91] P. Eastman, N. Gronbech-Jensen, and S. Doniach, J. Chem. Phys. **114**, 3823 (2001).
- [92] T. S. van Erp, D. Moroni, and P. G. Bolhuis, J. Chem. Phys. **118**, 7762 (2003).
- [93] D. Moroni, P. G. Bolhuis, and T. S. van Erp, J. Chem. Phys. **120**, 4055 (2004).
- [94] T. S. van Erp and P. G. Bolhuis, J. Comput. Phys. **205**, 157 (2005).
- [95] A. M. A. West, R. Elber, and D. Shalloway, J. Chem. Phys. **126**, 145104 (2007).
- [96] R. J. Allen, P. B. Warren, and P. R. ten Wolde, Phys. Rev. Lett. **94**, 018104 (2005).
- [97] S. C. Harvey and H. A. Gabb, Biopolymers **33**, 1167 (1993).
- [98] J. Schlitter, M. Engels, P. Krüger, E. Jacoby, and A. Wollmer, Mol. Simul. **10**, 291 (1993).
- [99] B. Isralewitz, M. Gao, and K. Schulten, Curr. Opin. Struct. Biol. **11**, 224 (2001).
- [100] N. M. Amato and G. Song, J. Comput. Biol. **9**, 149 (2002).
- [101] A. van der Vaart and M. Karplus, J. Chem. Phys. **122**, 114903 (2005).
- [102] A. van der Vaart and M. Karplus, J. Chem. Phys. **126**, 164106 (2007).
- [103] M.-R. Yun, N. Mousseau, and P. Derreumaux, J. Chem. Phys. **126**, 105101 (2007).
- [104] H. Grubmüller, Phys. Rev. E **52**, 2893 (1995).
- [105] M. Berkowitz, J. D. Morgan, J. A. McCammon, and S. H. Northrup, J. Chem. Phys. **79**, 5563 (1983).

- [106] R. Czerminski and R. Elber, J. Chem. Phys. **92**, 5580 (1990).
- [107] C. Choi and R. Elber, J. Chem. Phys. **94**, 751 (1991).
- [108] S. Fischer and M. Karplus, Chem. Phys. Lett. **194**, 252 (1992).
- [109] S. Huo and J. E. Straub, J. Chem. Phys. **107**, 5000 (1997).
- [110] R. Crehuet and M. J. Field, J Chem Phys **118**, 9563 (2003).
- [111] S. A. Trygubenko and D. J. Wales, J. Chem. Phys. **120**, 2082 (2004).
- [112] J. Schlitter, M. Engels, and P. Krüger, J. Mol. Graph. **12**, 84 (1994).
- [113] J. Ma, P. B. Sigler, Z. Xu, and M. Karplus, J. Mol. Biol. **302**, 303 (2000).
- [114] H. Grubmiller, B. Heymann, and P. Tavan, Science **271**, 997 (1996).
- [115] S. Izrailev, S. Stepaniants, M. Balsera, Y. Oono, and K. Schulten, Biophys. J. **72**, 1568 (1997).
- [116] E. Evans and K. Ritchie, Biophys. J. **72**, 1541 (1997).
- [117] H. Lu, B. Isralewitz, A. Krammer, V. Vogel, and K. Schulten, Biophys. J. **75**, 662 (1998).
- [118] J. H. J. Leech, J.; Prins, IEEE Comput. Sci. Eng. **3**, 38 (Winter 1996).
- [119] P. E. Marszalek *et al.*, Nature **402**, 100 (1999).
- [120] C. Jarzynski, Phys. Rev. Lett. **78**, 2690 (1997).
- [121] C. Jarzynski, Phys. Rev. E **56**, 5018 (1997).
- [122] S. Park and K. Schulten, J. Chem. Phys. **120**, 5946 (2004).
- [123] B. W. Zhang, D. Jasnow, and D. M. Zuckerman, J. Chem. Phys. **126**, 074504 (2007).
- [124] M. E. Fisher and A. B. Kolomeisky, Proc. Natl. Acad. Sci. U. S. A. **96**, 6597 (1999).
- [125] G. Margolin and E. Barkai, Phys. Rev. E **72**, 025101 (2005).
- [126] J. Wedekind, R. Strey, and D. Reguera, J. Chem. Phys. **126**, 134103 (2007).
- [127] A. M. Berezhkovskii, G. Hummer, and S. M. Bezrukov, Phys. Rev. Lett. **97**, 020601 (2006).
- [128] I.-C. Yeh and G. Hummer, Proc. Natl. Acad. Sci. U. S. A. **101**, 12177 (2004).
- [129] J. Alvarez and B. Hajek, Phys. Rev. E **73**, 046126 (2006).

- [130] W. Sung and P. J. Park, Phys. Rev. Lett. **77**, 783 (1996).
- [131] D. K. Lubensky and D. R. Nelson, Biophys. J. **77**, 1824 (1999).
- [132] M. Muthukumar, J. Chem. Phys. **111**, 10371 (1999).
- [133] M. Muthukumar, Phys. Rev. Lett. **86**, 3188 (2001).
- [134] S.-S. Chern, A. E. Cardenas, and R. D. Coalson, J. Chem. Phys. **115**, 7772 (2001).
- [135] J. Herbst, K. Heyne, and R. Diller, Science **297**, 822 (2002).
- [136] E. Samoylova *et al.*, J. Am. Chem. Soc. **127**, 1782 (2005).
- [137] R. Olender and R. Elber, J. Chem. Phys. **105**, 9299 (1996).
- [138] L. Onsager and S. Machlup, Phys. Rev. **91**, 1505 (1953).
- [139] M. Dykman and M. Krivoglaz, Sov. Phys. JETP **50**, 30 (1979).
- [140] A. J. Bray and A. J. McKane, Phys. Rev. Lett. **62**, 493 (1989).
- [141] M. I. Dykman, Phys. Rev. A **42**, 2020 (1990).
- [142] A. J. McKane, H. C. Luckock, and A. J. Bray, Phys. Rev. A **41**, 644 (1990).
- [143] A. J. Bray, A. J. McKane, and T. J. Newman, Phys. Rev. A **41**, 657 (1990).
- [144] H. C. Luckock and A. J. McKane, Phys. Rev. A **42**, 1982 (1990).
- [145] A. J. Mckane, J. Phys. A **26**, 5629 (1993).
- [146] R. Olender and R. Elber, J. Mol. Struct.: THEOCHEM **398-399**, 63 (1997).
- [147] M. Bier, I. Derényi, M. Kostur, and R. D. Astumian, Phys. Rev. E **59**, 6422 (1999).
- [148] R. Elber and D. Shalloway, J. Chem. Phys. **112**, 5539 (2000).
- [149] M. I. Dykman, P. V. E. McClintock, V. N. Smelyanski, N. D. Stein, and N. G. Stocks, Phys. Rev. Lett. **68**, 2718 (1992).
- [150] M. I. Dykman, D. G. Luchinsky, P. V. E. McClintock, and V. N. Smelyanskiy, Phys. Rev. Lett. **77**, 5229 (1996).
- [151] M. I. Dykman and V. N. Smelyanskiy, Superlattices Microst. **23**, 495 (1998).
- [152] G. Hummer, J. Chem. Phys. **120**, 516 (2004).
- [153] D. Bai and R. Elber, J. Chem. Theory Comput. **2**, 484 (2006).

- [154] S. Redner, *A guide to first-passage processes*, 1st ed. (Cambridge University Press, 2001).
- [155] E. W. Weisstein, *Poisson Sum Formula* (MathWorld—A Wolfram Web Resource, <http://mathworld.wolfram.com/PoissonSumFormula.html>).
- [156] E. W. Weisstein, *Error Function* (MathWorld—A Wolfram Web Resource, <http://mathworld.wolfram.com/Erf.html>).
- [157] G. B. Arfken and H. J. Weber, *Mathematical methods for physicists*, 5th ed. (Harcourt/Academic Press, 2001).
- [158] L. R. Mead and N. Papanicolaou, *J. Math. Phys.* **25**, 2404 (1984).
- [159] A. Tagliani, *J. Math. Phys.* **34**, 326 (1993).
- [160] D. Poland, *J. Chem. Phys.* **102**, 2604 (1995).
- [161] M. S. Jhon and J. S. Dahler, *J. Chem. Phys.* **68**, 812 (1978).
- [162] A. Macchi, A. A. Maradudin, and V. Tognetti, *Phys. Rev. B* **53**, 5363 (1996).
- [163] G. Talenti, *Inverse Probl.* **3**, 501 (1987).
- [164] Y. C. Hon and T. Wei, *Eng. Anal. Bound. Elem.* **26**, 855 (2002).
- [165] R. B. Best, Y.-G. Chen, and G. Hummer, *Structure* **13**, 1755 (2005).
- [166] K.-i. Okazaki, N. Koga, S. Takada, J. N. Onuchic, and P. G. Wolynes, *Proc. Natl. Acad. Sci. USA* **103**, 11844 (2006).
- [167] P. C. Whitford, O. Miyashita, Y. Levy, and J. N. Onuchic, *J. Mol. Biol.* **366**, 1661 (2007).
- [168] V. N. Maiorov and G. M. Crippen, *J. Mol. Biol.* **235**, 625 (1994).
- [169] N. Barton, C. Verma, and L. Caves, *J. Phys. Chem. B* **106**, 11036 (2002).
- [170] J. Shimada, E. L. Kussell, and E. I. Shakhnovich, *J. Mol. Biol.* **308**, 79 (2001).
- [171] J. Shimada and E. I. Shakhnovich, *Proc. Natl. Acad. Sci. USA* **99**, 11175 (2002).
- [172] H. Flyvbjerg and H. G. Petersen, *J. Chem. Phys.* **91**, 461 (1989).
- [173] L. Y. Chen, P. L. Nash, and N. J. M. Horing, *J. Chem. Phys.* **123**, 094104 (2005).
- [174] D. J. Tobias and C. L. Brooks, *J. Phys. Chem.* **96**, 3864 (1992).
- [175] C. Branden and J. Tooze, *Introduction to Protein Structure*, 1st ed. (Garland Pub., 1991).

- [176] D. M. Philipp and R. A. Friesner, *J. Comput. Chem.* **20**, 1468 (1999).
- [177] J. Apostolakis, P. Ferrara, and A. Caffisch, *J. Chem. Phys.* **110**, 2099 (1999).
- [178] T. Marrone, M. Gilson, and J. McCammon, *J. Phys. Chem.* **100**, 1439 (1996).
- [179] A. Drozdov, A. Grossfield, and R. Pappu, *J. Am. Chem. Soc.* **126**, 2574 (2004).
- [180] P. E. Smith, B. M. Pettitt, and M. Karplus, *J. Phys. Chem.* **97**, 6907 (1993).
- [181] P. E. Smith, *J. Chem. Phys.* **111**, 5568 (1999).
- [182] R. Vargas, J. Garza, B. Hay, and D. Dixon, *J. Phys. Chem. A* **106**, 3213 (2002).
- [183] D. Branduardi, F. L. Gervasio, and M. Parrinello, *J. Chem. Phys.* **126**, 054103 (2007).
- [184] M. Schaefer and M. Karplus, *J. Phys. Chem.* **100**, 1578 (1996).
- [185] N. W. Ashcroft and N. D. Mermin, *Solid State Physics*, 1st ed. (Brooks Cole, 1976).
- [186] P. Atkins and J. de Paula, *Physical Chemistry*, 7th ed. (W. H. Freeman, 2001).
- [187] R. Zwanzig, *J. Phys. Chem.* **96**, 3926 (1992).